Phase transitions and interfaces in temperature-sensitive colloidal systems

Nguyễn, V.Đ.

Publication date
2012
Document Version
Final published version

PHASE TRANSITIONS AND INTERFACES IN TEMPERATURE-SENSITVE COLLOIDAL SYSTEMS

NGUYỄN VĂN ĐỨC

PHASE TRANSITIONS AND INTERFACES IN

TEMPERATURE-SENSITVE COLLOIDAL SYSTEMS

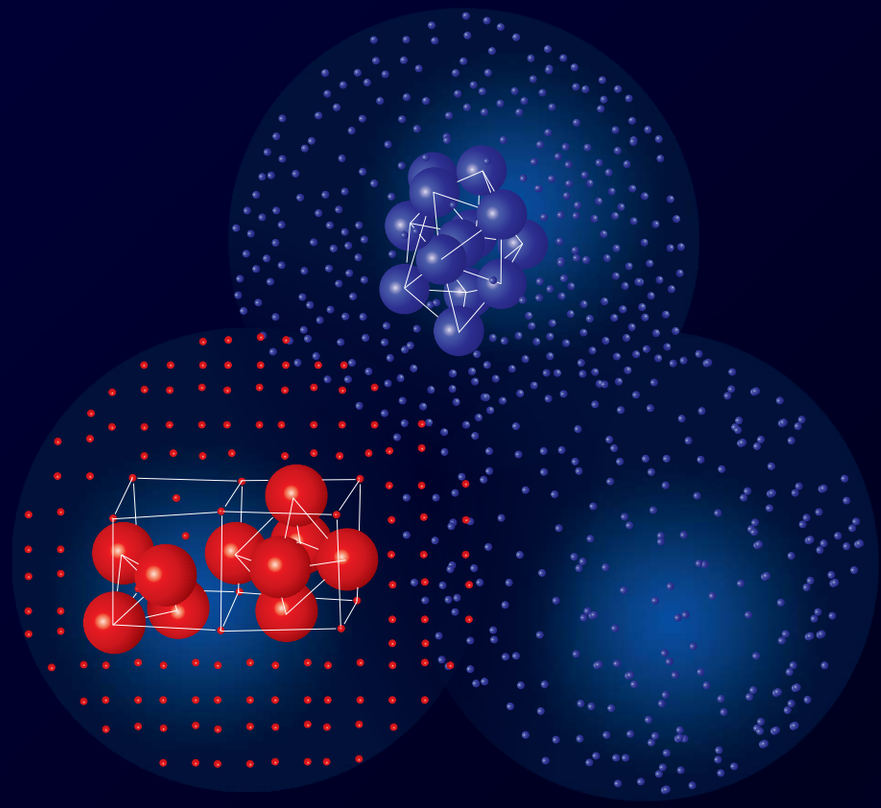

Nguyễn Văn Đức

Phase transitions and interfaces in temperature-sensitive colloidal systems

ACADEMISCH PROEFSCHRIFT

Ter verkrijging van de graad van doctor
Aan de Universiteit van Amsterdam
op gezag van de Rector Magnificus
Prof. dr. DC. Van den Boom
ten overstaan van een door het college voor promoties
ingestelde commissie, in het openbaar te verdedigen
in de Agnietenkapel op donderdag 20 december 2012, te 10.00 uur

door

Nguyen Van Duc

Geboren te Quang Ninh, Viet Nam

Promotiecommissie

Promotor:	Prof. dr. D. Bonn
Co-Promotor:	Dr. P. Schall
Overige leden:	*Prof. G. H. Wegdam*
	Prof. P. G. Bolhuis
	Prof. T. Gregorkiewicz
	Prof. M. Dijkstra
	Prof. D. Dean

Faculteit der Natuurwetenschappen, Wiskunde en Informatica

ISBN: 978-90-6464-610-2
Printed in the Netherlands

The author can be reached at : **vdnguyen77@gmail.com**

The work described in this thesis was carried out at the Institute of Physics, University of Amsterdam. The work was financially supported by the Innovational Research Incentives Scheme (VIDI grant) of the Nederlandse Organisatie voor Wetenschappelijk Onderzoek (NWO).

Tặng em Cẩm Thanh, con gái Cẩm Hà, con trai Đức Việt.

Amsterdam 2012

Contents

Chapter 1

Introduction

1.1 Colloids

Colloids are widely used because of their exceptional properties. Beside their importance for wide range applications in foods, petrol, cosmetics and drug industries, photonic crystal, optical filters and chemical sensor, they are also known as powerful model systems to study molecular phase behavior [1]. Particles are regarded as colloids when their diameter a is in the range of nanometer to micrometer, although any such definition is inevitably imprecise. The lower limit comes from the requirement that the particles be significantly larger than the molecules of the suspension medium. The upper limit ensures that the particles exhibit significant Brownian motion leading to equilibrium phase transitions and particle self-assembly, and that their motion is not dominated by extraneous effects such as gravitational and convection. Typically, the diameter of a colloidal particle is 10^3 -10^5 times larger than that of an atom. This disparity of size has several important consequences. Firstly, since the surface tension is proportional to a typical energy / a^2, interfacial tensions of colloidal phases are roughly 10^6 – 10^{10} times smaller than that of the atomic counterparts (Fig.1.1). The weakness of the colloidal surface tension means that the interface of the colloidal system can be easily deformed and

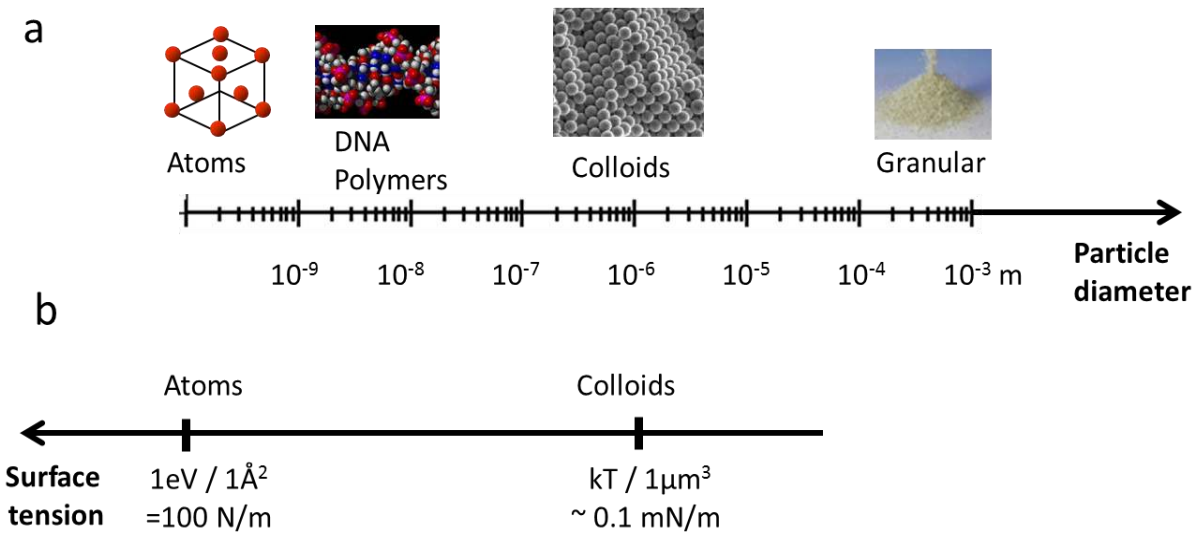

Figure 1.1: Schematic of the particle domain.

(a) The typical particle size scale. (b) The corresponding surface tension scale.

thermally induced fluctuations become large and directly observable. Secondly, because the time the particle needs to diffuse by its own radius is of the order of a fraction of a second, processes can be followed with great time resolution. The large diffusion time means that once disrupted or melted a colloidal system will take a macroscopic time (seconds, minutes or even hours) to rearrange. This brings a big convenience to investigate the evolution of the thermodynamic process in the system. Another important difference between atoms and colloids concerns the particle size distribution. The atoms (of one isotope) of a particular element are identical. However, with the possible exception of some biological materials, colloidal particles inevitably have some distribution of size or 'polydispersity' this size distribution can be tailored to study glass formation and particle assembly.

1.2 Colloidal phase behavior

Over the last few decades, the phase transitions in soft matter have been extensively studied. The most outstanding examples are colloidal systems in which the sizes, polydispersity and interactions of colloidal particles can be precisely set. For example, a rich colloidal phase behavior results from different type of repulsive and attractive

interactions (see Fig. 1.2) [2]. The simplest model system to mimic the phase behavior of simple atomic liquids and solids is the colloidal hard sphere system. Hard spheres are defined as impenetrable spheres that cannot overlap in space and they are non-interacting as long as they do not touch. A schematic of the hard sphere phase diagram is shown in Fig. 1.2a. The particle volume fraction ϕ is the only parameter to control the phase behavior. The system behaves like a fluid as ϕ is lower than 0.494. At $0.494 < \phi < 0.545$, fluid and crystalline phases coexist in the system. Above ϕ ~0.545, the crystal phase becomes thermodynamically stable. The addition of long-range attractions result in three-phase equilibria, with a triple point and phase line between liquid and gas ending in a critical point, Fig.1.2b. This is the phase diagram we know from atomic and molecular systems. For short-range attractions, equilibrium between gas and crystal is found, but the gas-liquid equilibrium becomes metastable, Fig.1.2c. In spite of the various forms of these phase behaviors, many of their properties have common origins, such as a large number of internal degrees of freedom, weak interactions between structural elements, and a delicate balance between entropic and enthalpic contributions to the free energy. These properties lead to large thermal fluctuations, sensitivity of equilibrium structures to external conditions, macroscopic softness, and metastable states.

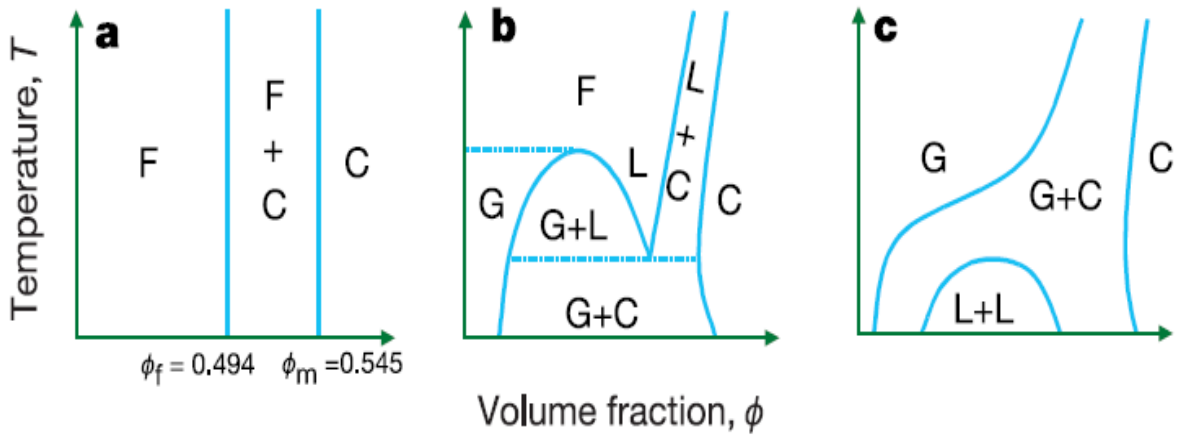

Figure 1.2: Colloidal phase diagram.

(a) Purely hard-sphere system, (b) long-range attraction system, and (c) short-range attraction system.

1.3 Interactions in soft matter

1.3.1 Screened Coulomb and van der Waals forces

Well-know Derjaguin-Landau-Verwey-Overbeek (DLVO) theory considers the total interaction between stabilized colloids as a sum of attraction and repulsion. The attractive Van der Waals interactions, also called London- dispersion forces, arise from the interactive forces between instantaneous multi-poles in molecules without permanent multi-pole moments. The total potential energy of two spheres of radius R at a center-to-center distance of r is given by [3];

$$U_{vdW} = -\frac{1}{6}A\left[\frac{2R^2}{r^2-4R^2} + \frac{2R^2}{r^2} - ln\left(1-\frac{4R^2}{r^2}\right)\right] \qquad (1.1)$$

where A is the Hamaker constant which depends on the polarisablilites of both the particles and the solvent. In practice, an estimate of the Hamaker constant is given by [4]:

$$A = \frac{3hv(n_1+n_2)^2(n_1-n_2)^2}{16\sqrt{2}(n_1^2+n_2^2)^{3/2}} \qquad (1.2)$$

where h is Planck's constant, v is the characteristic frequency and n_1 and n_2 are the refractive indices of the colloids and the solvent, respectively. When the refractive index of the colloidal particle is closely matched with that of solvent, the Hamaker constant is infinitely small and the van der Waals attraction is reduced. However, complete elimination of van der Waals forces is impossible, since the simultaneous refractive index matching at all wavelengths is impossible. Usually, the matching of refractive indices occurs at visible wavelengths

The van der Waals attraction diverges as the gap between the surfaces tend to zero [4]

$$\lim_{r\to 2R} U_{vdW}(r) = -\frac{A}{12}\frac{R}{r-2R} \qquad (1.3)$$

This negative potential has near contact a finite value, but becomes much larger than the thermal energy k_BT, leading in general to an irreversible aggregation of the colloidal particles. The effect of the van der Waals forces is to create a primary minimum in the potential near r=2R. Thus one needs to introduce some mechanism providing a large positive potential barrier in order to prevent the particles from being trapped in the primary minimum.

Colloids are mostly charge stabilized leading to repulsive Coulomb interaction between them. These repulsive forces act against dispersion forces thus avoiding the irreversible aggregation of colloids. In reality, the strong electric potential resulting from the charge of the particles attracts free counterions, a fraction of which get absorbed onto the surface forming a layer of condensed

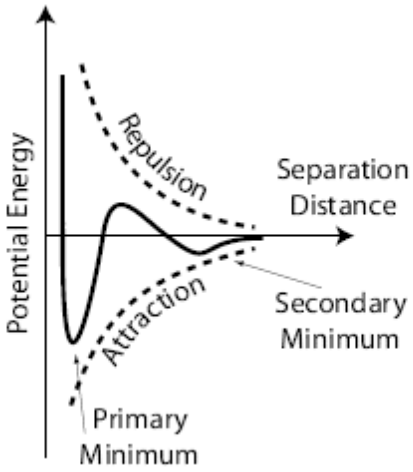

Figure 1.3: The schematic description of the DLVO interaction potential. The two dashed lines indicate the separate contributions of van der Waals attraction and double-layer repulsion. The solid line represents the total potential energy.

counterions [5]. The remaining free counterions form the so-called electrical double layer that screens the bare Coulomb repulsion between the charged colloidal particles and reduces its range. This leads to an interaction potential that does not scale as $1/r$, as for two charges in vacuum, but rather exhibits an exponential decay, the Yukawa-type form [6]

$$U_c(r) = \frac{(Ze)^2 exp(-kr)}{4\pi\epsilon\epsilon_{0r}}, \qquad (1.4)$$

where ϵ_0 is the permittivity of vacuum, ϵ is the dielectric constant of the medium and $\underline{Z}$ is a charge incorporating the effect of the finite size of the colloidal particle:

$$Z = Z^* \frac{exp(kR)}{1+kR}, \qquad (1.5)$$

where R is the radius of the particle. The inverse Debye screening length κ is given by [4]:

$$k = \sqrt{\frac{\rho_c (qe)^2}{\epsilon\epsilon_0 k_B T}}, \qquad (1.6)$$

where ρ_c is the density of the free counterions and q their valence. Thus, the screened Coulomb potential decays exponentially with the characteristic Debye length λ_D. The Debye length can be considered as the range of repulsive potential and corresponds approximately to the thickness of the diffuse electrical double layer. For the charged colloidal system, the total energy between charged colloids is the sum of the hard repulsion for $r < 2R$, the van der Waals attraction and the electrostatic repulsion (Fig. 1.3). The Derjaguin-Landau-Verwey-Overbeek (DLVO) theory is a well-known model for describing the interactions in a colloidal system [7].

1.3.2 Polymer mediated depletion attraction

Depletion interaction between colloids is induced by adding polymer to a colloidal system. When partial or complete depletion of macromolecules occurs between colloids and surfaces, the osmotic pressure difference between the bulk and gap regions produces an effective attractive potential between the colloids (Fig. 1.4) [8]. The attractive nature of this potential can be understood either from a force balance as particles and surfaces being pushed / pulled together from the integrated pressure or from an energetic perspective as the free energy associated with negative adsorption being minimized by closing the gap between particles and surfaces. The range and the strength of the attraction are controlled by the size and the concentration of the polymer, respectively. The above-mentioned phase behavior of attraction particles (Fig. 2b and c) has been experimentally explored using depletion interaction.

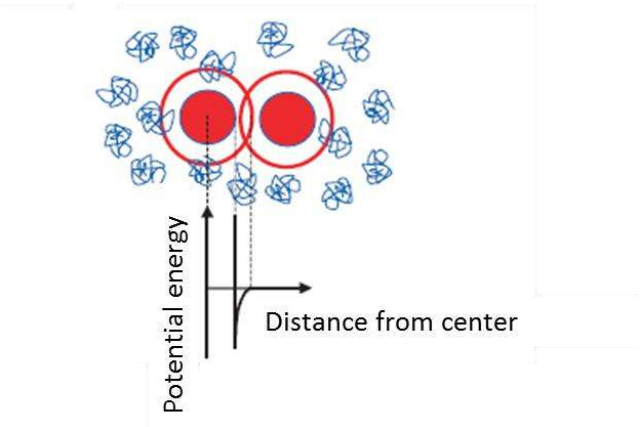

Figure 1.4: A schematic illustration of the origin of the polymer-induced depletion attraction between hard spheres (spheres). A volume (circles) exists around each sphere into which the center of the polymer coil (sketch) cannot penetrate.

1.3.3 DNA-mediated attraction

DNA-functionalized colloidal systems have been recently introduced in soft matter; Due to the specificity of the DNA interaction these systems are expected to be a powerful tool for guiding the self-assembly of nanometer-and micrometer-sized particles. The interactions originate from binding of complementary single-stranded DNA "sticky ends" which are coated on the surfaces of the colloids. These "sticky ends" on two different colloids either bind directly to each other via complementary sequences or via a ssDNA linker sequence introduced in solution. The strength of binding depends on the temperature, pH and ionic strength of the solution [9, 10].

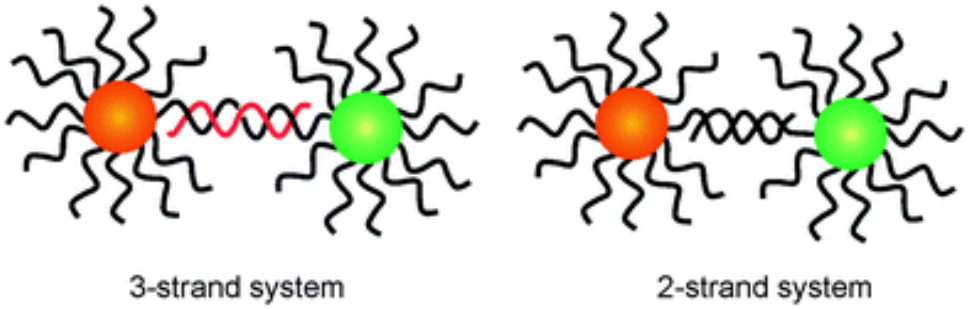

Figure 1.5: DNA- driven assembly can either be initiated by the addition of a linker DNA (3-strand system) or colloids can be coated with fully or partially complementary ssDNA directly (2-strand system).

1.3.4 Solvent mediated attraction or the critical Casimir forces

When fluctuating fields are confined between two walls, long-range forces arise. A well-known example is the quantum mechanical Casimir effect, where vacuum fluctuations of the electromagnetic field confined between two conducting plates cause attraction between these plates (Fig. 1.6a) [11]. It was predicted by Casimir in 1948 [12], but experiment could only confirm in 1980s and 1990s when atomic force microscopy had enough sensitivity [13]. A thermodynamic analogue is the critical Casimir force being realized in 1978 by Fisher and de Gennes [14]. This force arises due to the confinement of concentration fluctuations of a solvent close to its critical point (Fig. 1.6b). This force is attractive if the boundary conditions are symmetric and repulsive if the boundary conditions are asymmetric. The strength and range of this force depend sensitively on the solvent correlation length set by the temperature, as recently demonstrated by Bechinger *et al* with direct measurements of the critical Casmir force [15]. The authors used total internal reflection microscopy to measure directly the critical Casimir force between a

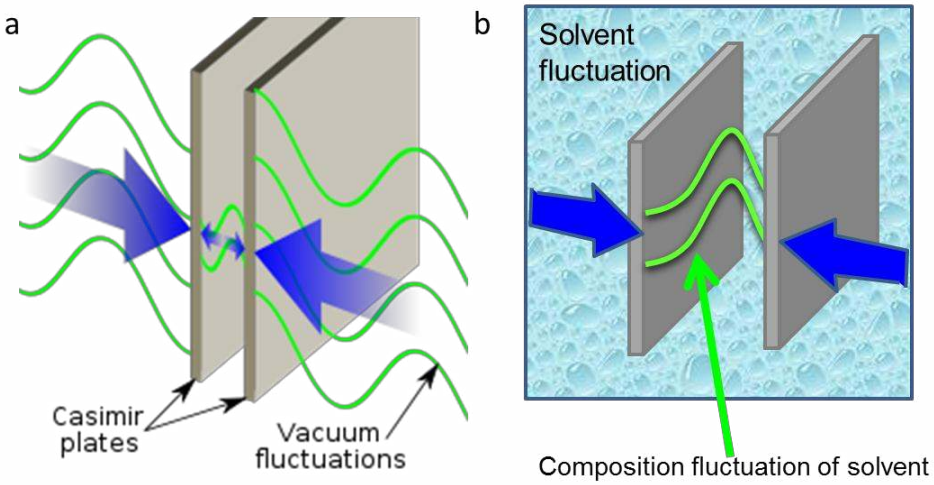

Figure 1.6: (a) Confinement of vacuum fluctuations leads to Casimir forces. (b) Confinement of composition fluctuations close its critical point leads to critical Casimir forces.

single colloidal sphere and a flat silica surface immersed in a mixture of water and 2,6 lutidine near its critical point.

In this thesis, we use attractive critical Casimir forces between colloids to induce colloidal phase transitions, and assemble the particle with temperature as a control parameter. We determine the particle pair potential directly and study gas-liquid transition quantitatively by tuning the strength and range of the critical Casimir interaction with temperature.

1.4 Solvent phase diagram

A binary mixture of water (D_2O/H_2O) and 3- methylpyridine (3-mp) exhibits concentration fluctuations when the temperature approaches the critical point of the mixtures. A schematic illustration of the solvent phase diagram is shown in Fig. 1.7. Outside the loop, water and 3-mp are well mixed and form a homogenous solvent, while within the loop, they are separated into water rich phase and 3-mp rich phases. The two-phase region ends at the critical point with 3mp concentration C_c. For the mixture used in this thesis $C_c = 0.31$. However, the shape and the width of the loop depend on the ratio of D_2O/H_2O in the mixture. The two phase region is maximal when the mixture has no D_2O and it shrinks with increasing fraction of heavy water concentration [16].

By approaching the critical point line from below, the correlation length increases. The resulting long-range fluctuations give rise to critical Casimir forces between the particles that are suspended in the solvent. These forces cause the particles to aggregate. Aggregation appears at the right hand side of the critical point C_c if colloids prefer water and at the left hand side when colloids prefer 3mp. In this thesis, we use particles that prefer 3-mp and therefore aggregation occurs on the left hand side of the critical point.

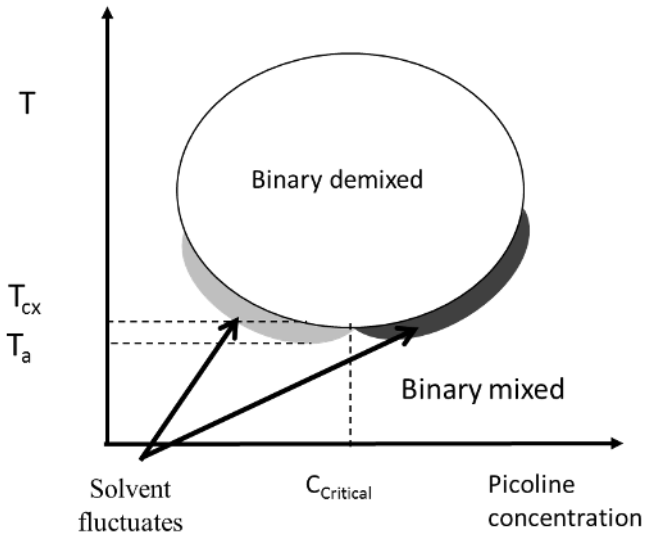

Figure 1.7: Schematic illustration of the solvent phase diagram. The solid line is the coexistence curve for the solvent mixture T_{cx}. The gray regions are the colloidal aggregate regions, corresponding to aggregate temperature T_a. $C_{critical}$ is critical composition of 3mp. When the particle preferred the water-rich phase aggregation occurs on the right side of the critical composition (dark gray), and when the particle preferred the 3mp-rich phase aggregation occurs on the left side of the critical composition (light gray).

1.5 Scope of this thesis

In this thesis we investigate two major subjects; in the first part, we investigate the crystal-fluid transition and free energy at colloidal crystal-fluid interface. In the second part, we study colloidal phase transitions induced by critical Casimir forces.

Chapter 2: We describe and discuss the experimental techniques used in this thesis. The main techniques are confocal microscopy, dynamic light scattering, temperature gradient and particle tracking. The standard sample preparation and particle size behavior are also presented.

Chapter 3: We present a new temperature-gradient method to grow colloidal crystals using thermosensitive particles, and provide a direct microscopic observation of colloidal crystal growth. We tune the volume fraction of the colloidal suspension by temperature, and then use the temperature gradient to grow colloidal crystal from a colloidal fluid. We use confocal microscopy to follow directly the heterogeneous crystal nucleation and the advancing interface. We measure the growth velocity of the crystal, diffusion coefficient of fluid particles and use them to determine the chemical potential difference between crystal and fluid phases. We investigate the effect of impurities on the advancing interface and determine the critical force needed to overcome impurity particles from the local interface curvature.

Chapter 4: In this chapter we focus on the equilibrium crystal-fluid interface. We visualize the structural transition from the long range order crystal to short range order fluid by measuring the possible packing configurations of particles in different phases. We establish a direct link between structure and interfacial energy by measuring the free energy change across the interface from the 3D particle configurations. The free energy is determined directly from the particle configurations. Moreover, we measure the anisotropy of the crystal-fluid interfacial tension directly from the thermally excited fluctuations of the interface.

Chapter 5: We perform experimental and simulation studies of colloidal phase transition induced by critical Casimir forces. We use confocal microcopy to observe these phase transitions directly. We show that by approaching the solvent phase separation temperature, colloidal gas condenses into a liquid and a crystal phase. The particle pair distribution function and, therefore, the particle pair potential are measured directly from the confocal images. The temperature-dependent range and amplitude of critical Casimir attractive force are determined. We use the particle pair potential and van der Waals model to examine the gas-liquid transition and compare it with the direct observation. We also use the measured particle pair potential as input for Monte Carlo simulation to fully study colloidal phase behavior. We find a good agreement between the simulation and the experimental results.

Chapter 6: In this chapter we mainly focus on visualization of colloidal liquid nucleation and growth induced by critical Casimir forces. First, liquid nucleation and growth are investigated by dynamic light scattering. We find three distinctive regimes: initial

nucleation, surface limited growth and diffusion limited growth. We then use confocal microscopy to follow directly the nucleation and growth process. We measure the density profile of liquid clusters and define the critical size of nuclei. The distribution of the cluster size is used to determine the cluster free energy barrier, and compare with classical nucleation theory predictions. We measure the interfacial tension and the chemical potential difference between gas and liquid particles and we find that these quantities are directly related to the degree of supersaturation.

Chapter 7: In the last chapter we study the morphology of fractal structures by combining experimental control of critical Casimir forces and Monte Carlo simulations of diffusion-limited aggregation. Experimentally, using temperature-quench we assemble particles into aggregates with well-defined morphology. We elucidate the relation between their fractal dimension and the depth of temperature quench directly by imaging the resulting structures at the particle scale. In the simulation, we use Monte Carlo simulations of diffusion-limited aggregation with finite particle dissociation probability to model the aggregation process, and relate the resulting structures directly to the attractive potential strength.

Bibliography

[1] P. Pusey, Colloidal suspensions, UK.

[2] V. J. Anderson and H. N. W. Lekkerkerker, "Insights into phase transition kinetics from colloid science," *Nature,* vol. 416, p. 811, 2002.

[3] W. R. Schowalter, colloidal dispersions, Cambridge: Cambridge university press, 1989.

[4] J. Israelachili, Intermolecular and surface forces, London: Academic press, 1992.

[5] D. H. Eerett, Basic principles of colloid science, London: Royal society of chemistry, 1988.

[6] L. D. Landau, and B. V. Derjaguin, "Theory of the stability of strongly charged lyophobic sols and of the adhesion of strongly charged particles in solution of electrolytes," *Acta Physicochim USSR,* vol. 14, p. 633, 1941.

[7] E. J. W. Verwey, and J. T. Overbeek, Theory of the stability of lyophobic colloids, Amsteram: Elsevier, 1948.

[8] S. Asakura, and F. Oosawa, "On interaction between two bodies immersed in a solution of macro-molecules," *J. Chem. Phys.,* vol. 22, p. 1255, 1954.

[9] A. Paul Alivisatos, et al, "Organization of "Nanocrystal molecules" using DNA," *Nature,* vol. 382, p. 15, 1996.

[10] M. E. Leunissen et al, "Switchable seft-protected attractions in DNA-functionalized colloids," *Nature,* vol. 8, p. 590, 2009.

[11] K. A. Milton, The Casimir effect, Singapore: World scientific, 2001.

[12] H. B. G. Casimir, *Proc. K. Ned. Akad. Wet.,* vol. 51, p. 739, 1948.

[13] U. Mohideen and A. Roy, "Precision Measurement of the Casimir Force from 0.1 to 0.9μm," *Phys. Rev. Lett.,* vol. 81, p. 4549, 1998.

[14] Gennes, M. E. Fisher and P.-G. de, "Physique des Colloides," *C. R. Acad. Sci. Ser. B,* vol. 287, p. 207, 1978.

[15] C. Hertlein, L. Helden, A. Gambassi, S. Dietrich, C. Bechinger, "Direct measurement of critical Casimir forces," *Nature,* vol. 451, p. 172, 2008.

[16] Z. P. Visak, L. P. N. Rebelo and J. Szydlowski, " The hidden phase diagram of water+ 3-Methylpyridine at large absolute negative pressures," *J. Phys. Chem. B,* vol. 107, p. 9837, 2003.

Chapter 2

Experimental Techniques

In this thesis, we investigate colloidal phase behavior and the interfaces at the particle level in both real space and reciprocal space. The particle sizes are in the range of several hundred nm to μm, therefore, the standard experimental methods used in this thesis are light scattering and confocal microscopy. Below we describe in detail the basic principle of each techniques and the information obtained by them. We also show the standard methods of sample preparation, particle size measurement and temperature control techniques.

2.1 Dynamic light scattering

When colloidal particles are suspended in a solvent, the particles exhibit a random motion called Brownian motion. Each particle exhibits a zigzag motion, and its motion is uncorrelated with the other particles in very dilute suspensions. As light scatters from the moving particles, this motion imparts a randomness to the phase of the scattered light, such that when the scattered light from two or more particles is added together, there will be a changing destructive or constructive interference. This gives rise to time-dependent

fluctuations in the intensity of the scattered light, known as "speckle patterns". The fluctuations are quantified by the intensity autocorrelation function [1, 2]

$$\langle I(q,t)I(q,0)\rangle = \lim_{T\to\infty}\frac{1}{T}\int_0^T I(q,\tau)I(q,\tau+t)d\tau \qquad (2.1)$$

where q is the scattering wave-vector, $I(q,0)$ and $I(q,t)$ are the scattered intensity at time 0 and time t, respectively. The brackets denote an ensemble average. The scattering wave-vector is directly related to the laser wave length λ and scattering angle θ as

$$q = (4\pi/\lambda)\sin(\theta/2) \qquad (2.2)$$

A sketch of the light scattering setup is shown in Fig. 2.1.

In Dynamic Light Scattering (DLS) measurements, the time fluctuations of the scattered intensity are sent into a correlator that calculates the normalized intensity correlation function in real time as

$$g^1(q,t) = \frac{\langle I(q,0)I(q,t)\rangle}{\langle I(q)\rangle^2} \qquad (2.3)$$

where $\langle I(q)\rangle$ is the ensemble averaged scattered intensity. For simple diffusion of the particles, this correlation function decays exponentially with time as

$$g^1(q,t) = \exp\left(-2Dq^2t\right) \qquad (2.4)$$

where D is the diffusion coefficient. The hydrodynamic radius R of the particles is determined directly from the diffusion coefficient using the Einstein-Stokes relation:

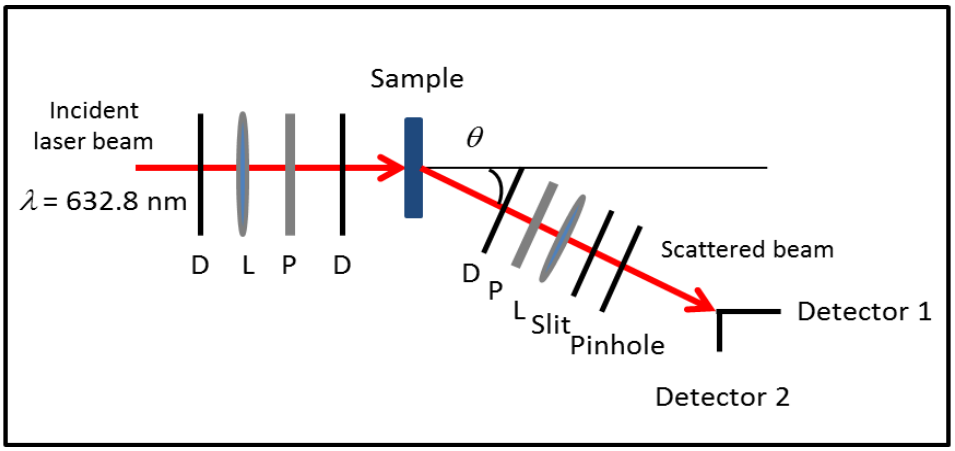

Figure 2.1 : Schematic configuration of the light scattering setup.

$$R = \frac{k_B T}{6\pi\eta D} \qquad (2.5)$$

where η is the viscosity of the solvent, k_B is Boltzman's constant, and T is temperature of the solvent.

2.2 Confocal microscopy

2.2.1 Confocal microscopy setup

The Laser Scanning Confocal Microscope (LSCM) was invented in 1957 by Marvin Minsky [3]. The confocal microscope uses point illumination and a pinhole in an optically conjugate plane in front of the detector to eliminate out-of-focus light. Only the light within the focal plane is detected, so the LSCM provides 2D sections though a 3D specimen. As only one point is illuminated at a time in LSCM, 2D or 3D imaging requires scanning over a regular raster (i.e. a rectangular pattern of parallel scanning lines) in the specimen. The thickness of the focal plane is defined mostly by the point spread function due to the diffraction through the circular aperture (pinhole).

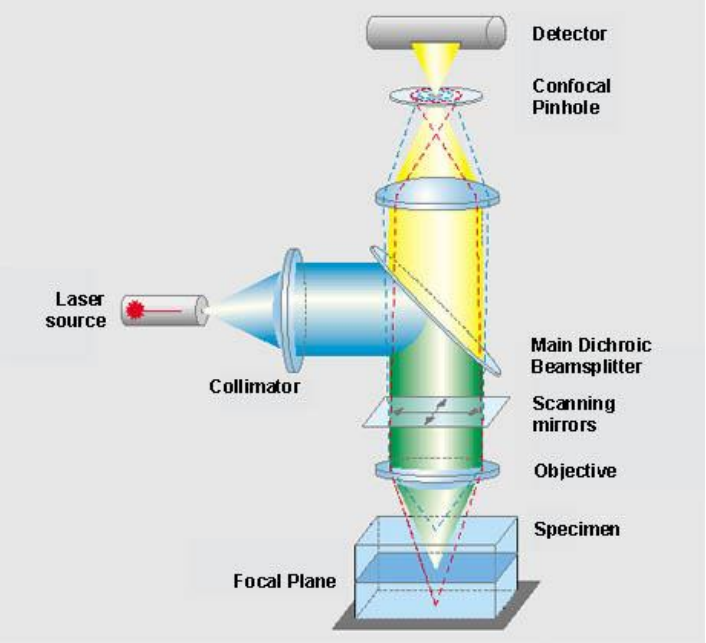

Figure 2.2 : Schematic configuration of the confocal microscope setup.

A LSCM shows much better contrast than a conventional microscope because the detector pinhole blocks most scattered and out of focus light. Also, scattered light is reduced because only a small part of the sample is illuminated. Fluorescent samples give good contrast because a filter can block out everything except the fluorescent wavelengths. With a dichroic mirror, a single objective can be used so that the laser and the fluorescent light go through the same objective (Fig. 2.2). A conventional LSCM can take an image in about one second. Here, we use a recent fast Zeiss LSM 5 Live confocal microscope that can acquire up to 120 frames per second at a resolution of 512 by 512 pixels.

2.2.2 Data acquisition

The most widely used particle tracking algorithm was introduced by Crocker and Grier in 1995 [4]. By assuming the particles appear as spherical bright spots on a dark background, the software defines local brightness maxima within an image as candidate particle locations. Then the tracking algorithms remove the undesired noise and long wavelength contrast gradients using a spatial band pass filter. A centroid algorithm finds the center of particles by locating the brightness weighted center of mass of the bright spots. With this refinement procedure the coordinates of the particle centers can be obtained with sub-pixel resolution down to less than 1 / 10 of the pixel size. We show an example of the different stages of the particle tracking procedure in Fig. 2.3; the confocal image (a), the image after using the spatial band pass filters (b), and the determined particle centers, shown as the black dots within the white spots (c).

Figure 2.3 : Particle tracking procedure:

(a) A confocal image. (b) The image after using spatial band pass filter. (c) The particle centers are shown as the black dots within the white spots.

One of the most advanced features of the software is linking particle locations into trajectories. The program matches up locations in each image with corresponding locations in later images to produce particle trajectories. This requires determining which particle in a given image most likely corresponds to one in the preceding image. Linking particle positions into trajectories is only feasible if the typical single particle displacement between subsequent images is sufficiently smaller than the typical inter-particle spacing, a. Otherwise, particle positions will become inextricably confused between snapshots. The optimal cutoff parameter falls in the range of $\delta \leq a/2$. Any particle with no match in the successive frames is considered to be lost. Such particles are generally detected at the boundaries of the images where the particles move in and out of the field of view.

2.3 Sample and sample cell preparations

Below we describe in detail the preparation method to obtain the monodisperse colloidal samples used in this thesis. We used colloidal poly-N- isopropylacrylamdie (pNipam) particles that are cross-linked microgel spheres. The spheres swell in water at room temperature, but shrink and undergo a reversible volume transition above the critical solution temperature [5-8]. In the swollen state, the density and refractive index match closely that of the solvent, preventing settling of the particles for several weeks and allowing to image particles deep inside the bulk of a dense suspension. The particles are labeled with a fluorescent dye that allows us to image them with LSCM.

2.3.1 Samples for crystal growth

For the colloidal crystal growth described in chapter 3, it is important to use a monodisperse suspension. In the following we describe the cleaning and preparation steps applied to obtain the final sample. The fluorescent Poly-N-isopropylacrylamdie microgel suspensions were obtained from Zhibing Hu, University of North Texas. To screen the particle charge, LiCl 0.005 M was added to the suspension. The sample contained a small amount of larger particles (impurities) which were removed by centrifuging. To do this, the stock suspension was diluted five times with water, and was subsequently concentrated by centrifugation at a speed of 7500 rpm for 30 minutes. Because of the larger size, the impurities settled faster than the rest of particles. By taking out the upper half of the

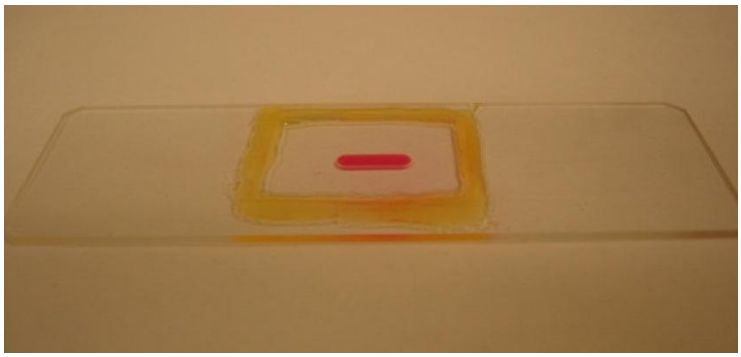

Figure 2.4: An image of glass sample cell used for crystal growth. pNipam suspension (pink) is filled in the middle of the cell, covered by a microscope slide and glued by Bevat 2- hydroxyethylmethacrylaat (yellow).

suspension, we achieved a uniform pNipam colloidal suspension. In order to not waste the sample, the bottom half of the suspension was diluted and concentrated subsequently five times. To obtain the final sample, the monodisperse suspension was then centrifuged with a higher speed for a longer time (9000 rpm, 100minutes) and subsequently water was removed with a pipette. The concentrated suspension was then diluted to an effective volume fraction of 55 %.

We prepared a sample cell by making a hole of 10 x 2 x 1 mm in the middle of a 75 x 25 x 1 mm glass slide. To avoid contamination, the glass slide was soaked in chromic acid for one day, rinsed several times with Millipore water, and then dried in a vacuum oven. One side of the glass slide was closed by a microscope cover glass with dimensions 15 x 32 x 0.19 mm, glued by a dilute Bevat 2- hydroxyethylmethacrylaat solution. After curing by UV light for one day the cell was ready for use. We filled the suspension in the blank cell, which we covered by a microscope slide, sealed with 2-epoxy components glue. The final sample cell is shown in Fig. 2.4.

2.3.2 Samples for critical Casimir effect

The second part of the thesis (chapter 5-7) deals with the aggregation and phase transitions by critical Casimir forces. The samples for these studies were prepared by suspending the pNipam particles in a mixture of 3-Methyl Pyridine (3MP), water and heavy water. The range and amplitude of the force depends not only on the temperature, but also on the concentration of liquid components [9-11]. In this thesis, we investigate the temperature

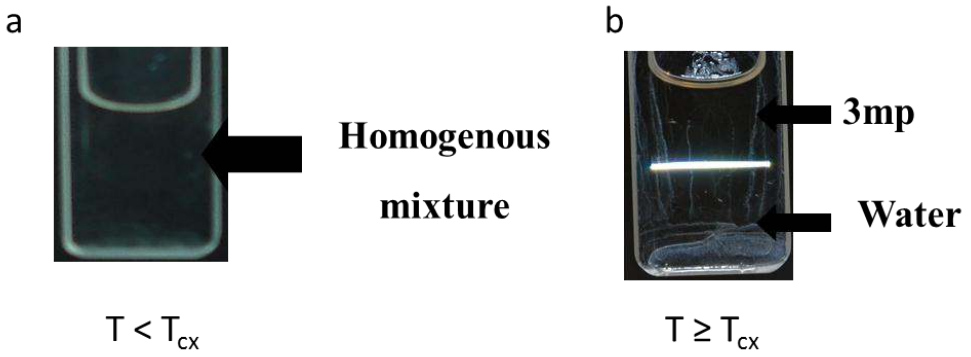

Figure 2.5: Images of binary mixture in glass sample cells.

(a) Below the solvent separated temperature, a homogenous mixture is observed, (b) Above the solvent separated temperature, the mixture separates into 3mp-rich phase (above) and water-rich phase (below).

dependence of the critical Casimir forces using two types of quasi two-component solvent. The first quasi two-component solvent consists of 3MP and water (H_2O and D_2O) with mass fractions of 0.25 and 0.75, respectively, and on the left side of the critical concentration C_c = 0.31. This solvent mixture separates into 3MP-rich and water-rich components upon heating to $T_{c\,x} = 52.2$ °C (see Fig.2. 5) and will be used to investigate the colloidal gas-liquid transition in chapter 5. The other mixture has 3mp mass fraction of 0.28, and is closer to the critical point. This solvent mixture separates into 3MP-rich and water-rich components upon heating to $T_{c\,x} = 39.5$ °C. It will be used to investigate liquid nucleation and morphology of cluster aggregate in chapter 6 and 7. The change of solvent composition allows us to investigate the influence of the solvent composition on the particle pair potential (see chapter 5). pNipam particles with a weight fraction of ~0.3% are suspended in the binary solvent. The advantage of these particles is that their refractive index and density match closely that of the binary solvent, making the suspension transparent, and preventing particle sedimentation. We find that these particles are stable in the 3mp-water mixture over at least several months. The suspension is filled in a 0.2 x 4.0 mm clean glass capillary and the capillary flame sealed to avoid solvent evaporation.

2.4 Measurement of particle size

Particle volume fraction is the unique parameter controlling the crystal-fluid transition in hard sphere system. In our system, we tune the particle volume fraction by controlling the

pNipam colloid size using temperature. In order to know precisely how the particle size changes with the temperature, we investigate the temperature dependence of the particle radius using dynamic light scattering techniques.

2.4.1 Sample preparation for dynamic light scattering

We diluted the monodisperse suspension to particle volume fraction of 0.5% by adding water. The suspension was then filled into a quartz curvet and the curvet was thoroughly closed by a cap and well winded by parafilm to avoid solvent evaporation. We embedded the curvet in the scattering chamber, which was connected to a thermostat to control its temperature. We fixed the scattering wavelength q=0.37 μm^{-1} by fixing the scattering angle at $\theta = 90^{o}$. The incident laser beam has a scattering wavelength at λ = 632 nm. We measured the scattered intensity $I(t)$ and the reduced correlation function $g^{1}(q,t)$ as a function of time to determine the particle size.

2.4.2 Experimental results and discussion

We show the reduced correlation function at T = 20 ^{o}C in Fig.2.6a. The best exponential fit to the data gives the diffusion coefficient D = 0.308 $\mu m^2/s$. Using the viscosity of water at 20 ^{o}C, η = 1.002 Pas, and the Stokes – Einstein relation, we obtain the hydrodynamic radius of the pNipam particles R_h = 694 nm. We gradually increased the temperature from 20 ^{o}C to 40 ^{o}C in steps of 1 ^{o}C, and equilibrated the system for 30 minutes at each step before making a new measurement.

The resulting correlation functions of the pNipam suspension at different temperatures are shown in Fig. 2.6b. Single exponential functions are observed at all investigated temperatures. With increasing temperature, the correlation functions are shifted to the left indicating an increase in the diffusion coefficient, which reveals a decrease of the particle size with increasing temperature. The curves are clearly divided into two groups, indicating that the diffusion coefficient changes rapidly when the temperature increases from 32 to 33 ^{o}C. The resultant average hydrodynamic radius of the particles as a function of temperature is shown in Fig. 2.7 (solid triangle). The radius of the particle decreases from 694 nm at 20 ^{o}C to 345 nm at 38 ^{o}C, a decrease by a factor of 2. In detail, when the

temperature increases from 20 to 32 ^{o}C, the particle radius decreases slightly from 694 to 639 nm and it decreases rapidly when the temperature is in the range of 32-36 ^{o}C. However, the particle radius is almost constant when the temperature is above 38 ^{o}C. This is in good agreement with earlier observations [5- 8].

We examine the reversibility of the particle size change by measuring the particle radius with decreasing temperature. The values are shown as open squares in Fig. 2.7. In general, both data sets are consistent. However, at 32, 34, and 36 ^{o}C the values show larger

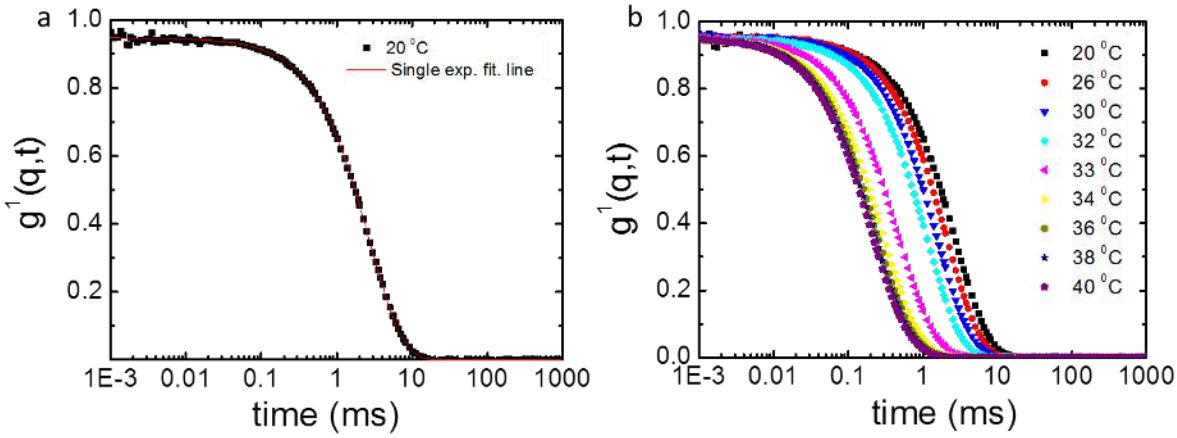

Figure 2.6: Reduced correlation function, measured by means of dynamic light scattering, of pNipam suspension at $\phi = 0.005$. (a) At $T = 20\ ^{0}$C, experimental measurements (squares), and best single exponential (solid line). (b) At different temperatures, single exponential functions are observed at all investigated temperatures.

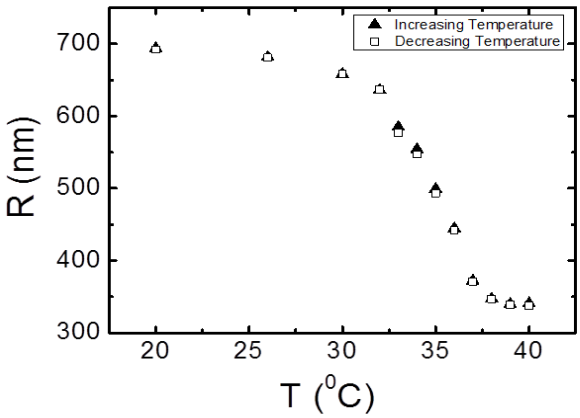

Figure 2.7: Hydrodynamic radius of pNipam particle as a function temperature; solid triangle-measured with increasing of temperature, open square-measured with decreasing of temperature.

deviations. We associate these deviations with the rapid change of particle size at these temperatures. Here, a longer waiting time is needed for the system to reach the final thermal equilibrium.

2.5 Temperature-control setup

In this thesis, temperature is the key parameter controlling the colloidal phases. On the one hand, we use the temperature to tune the particle size to control the growth of large crystals, while on the other hand we use temperature to control the amplitude and range of the critical Casimir forces via fluctuations of binary solvents. The detail of the temperature-control setup is described below.

A photo and a schematic of the temperature setup are shown in Fig.2.8. A temperature stage is directly connected to a thermostat by a water loop. The thermostat controls the average temperature of the sample and the microscope objective with a stability of 0.02 ^{o}C. For the critical Casimir experiments (chapter 5, 6 and 7), the sample cell is mounted directly on the surface of the stage using thermal paste.

To guide the crystallization from its melt (chapter 3 and 4), we introduce a temperature gradient using peltiers. These peltiers are mounted on opposite sides of the temperature stage and they are placed upside down with respect to each other. A voltage is applied to both elements, the upper plate of one peltier warms up with respect to the water bath while the upper plate of the other peltier cools down. This results a temperature gradient from

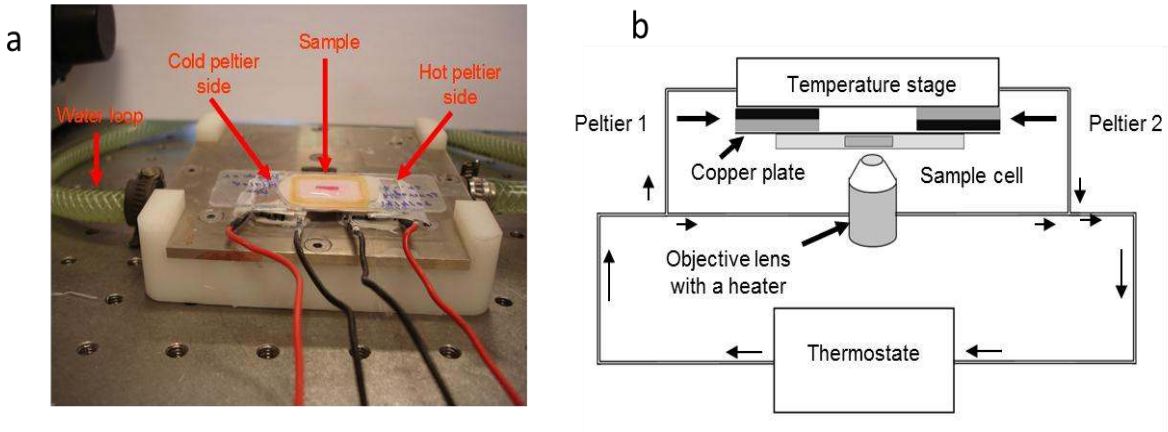

Figure 2.8: (a) An image of the temperature gradient setup and (b) its schematic configuration used for the crystal growth experiment.

left to right. A thin copper plate, 0.5 mm thick, is placed on top of the two peltiers in order to have a linear temperature profile. Finally, a sample cell is mounted on top of the thin cooper plate using thermal paste.

We use an infrared camera to check the temperature profile of our sample cell. An infrared image of the pNipam sample cell at an applied electric current of I = 0.7 A, and a voltage of U = 3 V is shown in Fig. 2.9a. Different colors in the image correspond to different temperatures (see the color scale on the right). This way, we measured the temperature across the sample cell as function of applied electric current. The resulting temperature profiles, for different electric currents at U = 3 V, are shown in Fig. 2.9b. The data confirms that, to good approximation, the temperature is a linear function of the distance.

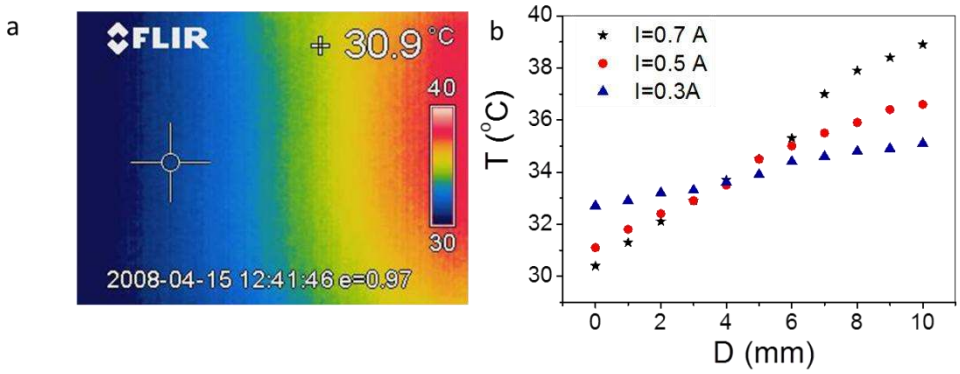

Figure 2.9: Temperature gradient of sample cell: (a) an infrared-camera picture of the sample cell at U = 3 V and I = 0.7 A. (b) Temperature as a function of distance across the cell, measured with an infrared camera at U = 3 V and different applied electric currents to the peltiers.

Bibliography

[1] S. C. Johnson and D. A. Gabriel, Laser Light Scattering, Ontario: CRC press, Inc, 1981.

[2] W. Brown, Dynamic Light Scattering, Oxford: Clarendon press, 1993.

[3] M. Minsky, "Memoir on inventing the confocal scanning microscope," *Scanning,* vol. 10, p. 128, 1988.

[4] J. Croker and D. Grier, "Method of digital video microscopy for colloidal studies," *J. of Colloid Interface Sci.,* vol. 179, p. 298, 1996.

[5] J. Gao and Z. Hu, "Optical properties of N-Isopropylacrylamide microgel spheres in water," *Langmuir,* vol. 18, p. 1360, 2002.

[6] R. H. Pelton, "Temperature-sensitive aqueous microgels," *Adv. Colloid Interface Sci.,* vol. 85, p. 1, 2000.

[7] R. H. Pelton, P. Chibante, "Preparation of aqueous latices with N-isopropylacrylamide," *Colloids Surf.,* vol. 20, p. 247, 1986.

[8] M.J. Snowden and B. Vincent, "The temperature-controlled flocculation of crosslinked lates particles," *J. Chem. Soc. Commun.,* p. 1103, 1992.

[9] D. Beysens and T. Narayanan, " Wetting-induced aggregation of colloids," *J. Stat. Phys,* vol. 95, p. 997, 1999.

[10] T. Narayanan, A. Kumar and E.S.R. Gopal, "A new description regarding the approach to double criticality in quasi-binary liquid mixtures," *Phys. Let. A,* vol. 155, p. 276, 1991.

[11] C. Hertlein, L. Helden, A. Gambassi, S. Dietrich, C. Bechinger, "Direct measurement of critical Casimir forces," *Nature,* vol. 451, p. 172, 2008.

Chapter 3

Microscopic observation of colloidal crystal growth

3.1 Introduction

Three-dimensional ordered colloidal systems whose lattice constants are comparable to the wavelength of visible light have important applications in photonic crystals [1], optical filters and switches [2], and chemical sensors [3]. Recently, colloidal crystallization has been actively studied [4-8], leading to the development of several methods to control the self-assembly of the colloidal particles; for example colloidal epitaxy [9] and space-based reduced gravity techniques [10].

In this chapter, we show that by using new temperature-sensitive colloidal particles and a temperature gradient, we can grow large, equilibrated colloidal crystals. The temperature changes the size of the particles, thereby allowing precise control over the crystal growth process. We apply a temperature gradient to guide the nucleation of a few crystals, and use slow cooling to direct the growth of these crystals. We use confocal microscopy to image the entire crystal growth process: heterogeneous crystal nucleation, the advancing crystal-fluid interface, and the stationary equilibrium crystal-fluid interface at the particle level. We determine the diffusion coefficient of particles in the liquid from their mean-square

displacement. The amount of supersaturation that drives the growth of the crystals is then determined directly from the measured crystal growth velocity and the diffusion coefficient. We find that crystals grow perfectly at moderate supersaturations with a chemical potential difference $\Delta\mu \sim 0.4 k_B T$ between the crystal and fluid. Finally, we investigate the stability of growth by adding impurity particles. This allows us to directly observe the role of surface tension to surmount the impurities during growth and keep the interface stable and straight.

3.2 Crystal growth procedure

We have shown in the preceding chapter that the size of the colloidal pNipam particles depends strongly on temperature. The particle diameter changes reversibly from d~1.4 µm at room temperature to d~0.7µm at 36.0 °C with a polydispersity of less than 3%. We use these properties to control the particle volume fraction in order to drive the crystal growth with a temperature gradient. The used temperature protocol is shown in Fig.3.1a. We start with a suspension that is fully crystallized at room temperature, and then increase the average temperature to 36.0 °C, at which the crystals melted entirely. We waited for one hour to obtain a homogeneous colloidal melt. A linear temperature gradient of 2 °C/cm was applied across the cell, and we lowered the average temperature of the sample slowly at a rate of 0.5 °C/h with a temperature stability of 0.02 °C to direct nucleation and the

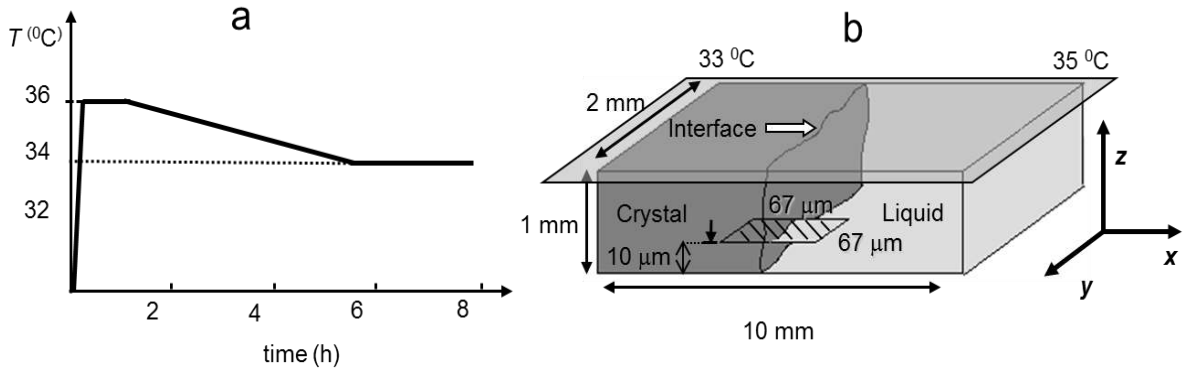

Figure 3.1: (a) Schematic of the temperature protocol used for the crystal growth. (b) Schematic showing the imaged 67 x 68 mm section (dashed) with respect to the sample cell. The dark gray color represents the crystals, while the light gray color represents the fluid. The *x* axis aligns with the temperature gradient direction.

growth of macroscopic crystals. We used confocal microscopy to image individual particles in horizontal slices of 67 μm by 67 μm at the interface (see Fig. 3.1b); these slices contain roughly 12,000 particles. The *x*-axis aligns with the temperature-gradient direction. To avoid boundary effects, we focus on sections roughly 10 μm above the cover slip.

3.3 Observation of crystal nucleation and growth

After two hours of cooling, we observed that particles order in a few corners of the sample. Fig. 3.2a shows that within the area indicated by the dotted line, the particles crystallize, while they are still disordered outside. We interpret these areas as heterogeneous crystal nuclei forming at the corners of the sample cell. Such heterogeneous nucleation reduces the interfacial area between the crystal and its melt, and is therefore energetically preferred over homogeneous nucleation in the bulk. We followed the development of these nuclei, and saw that they grew to large crystals when we lowered the temperature. Close inspection reveals that these crystals exhibit a random hexagonal close packed (rhcp) structure. They consist of a random stacking of hexagonal close packed (hcp) planes, similar to crystals formed in hard-sphere colloidal systems. The hcp planes align with the cover slip; their lateral orientation is random.

We focus on the early stage of crystal growth, and image the interface after t_1 = 2.5 hrs when the crystals have grown to 180 μm in length. Selected snapshots of the crystal-fluid interface during growth are shown in Fig. 3.2b-d. The interface advances in the positive *x*-direction, while at the same time significant fluctuations of the interface occur. We determine the growth velocity by following the mean interface position as a function of time in Fig. 3.3. The data indicates linear growth with a constant velocity of $v = 0.1$ μm/s.

We follow the motion of the individual particles in the fluid and crystal to determine their mean square displacement. 200 images are acquired at a frame rate of 30 images/s and the positions of the individual particles in the horizontal sections are tracked with an accuracy of 0.03 μm [11]. Particle trajectories are plotted in Fig. 3.4a. While for particles in the fluid, these trajectories indicate diffusive motion, for particles in the crystal, they indicate confinement of the particles to their crystal lattice positions. For more clarity, we plot enlarged trajectories of a single particle in the crystal and fluid phase in the left- and right

hand inset of Fig. 3.4a. We determine the mean square displacement $\langle r^2 \rangle$ separately for particles in the crystal and fluid, and plot $\langle r^2 \rangle$ as a function of time in Fig. 3.4b. For crystal particles, the mean square displacement saturates at $\langle r^2 \rangle_\infty = 0.0086\ \mu m^2$ due to confinement by their neighbors, while for fluid particles $\langle r^2 \rangle$ increases linearly with time confirming that the particles exhibit diffusive motion. For the crystals, the asymptotic value of the crystal mean square displacement corresponds to twice the variance of the particle displacement from their equilibrium position. Assuming that particle fluctuations are isotropic, we used this value to determine the three-dimensional Lindemann parameter of melting using [12]

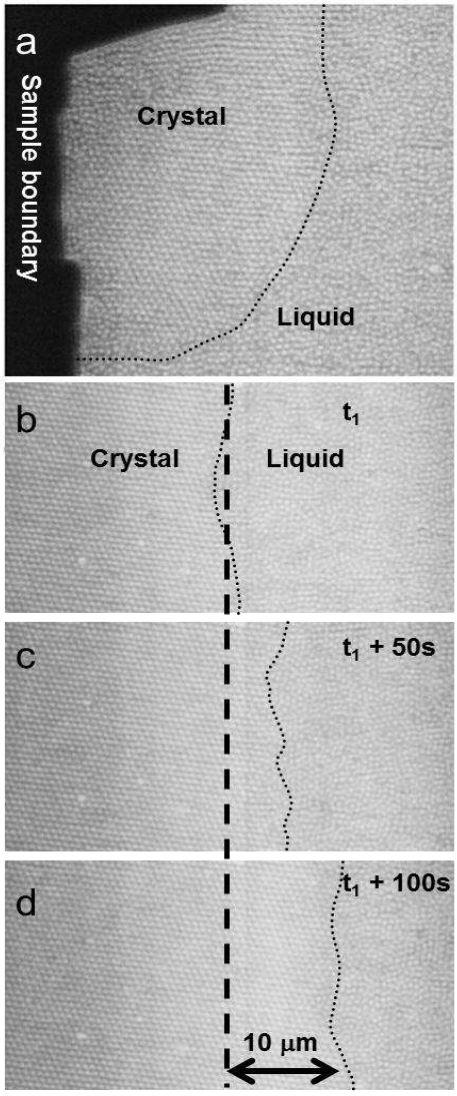

Figure 3.2: Observation of crystal nucleation and growth. (a) Confocal microscope image of a crystal nucleus forming at the sample boundary. (b)–(d) Sequence of confocal microscope images taken during the early stage of crystal growth, starting after t_1 = 2.5 h of cooling. Dotted lines indicate the advancing interface, and the dashed line indicates the initial position of the interface at time t_1.

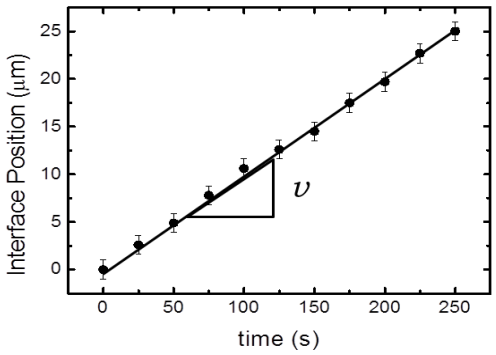

Figure 3.3: Mean interface position as a function of time, experimental measurements (dots) and best linear fit (solid line)

$$L = \frac{1}{r_{nn}} \sqrt{\frac{3}{4} \left\langle r^2 \right\rangle_\infty} \,. \qquad (3.1)$$

Here the crystal nearest neighbor distance $r_{nn} = 0.75\mu m$. We find $L \sim 0.115$, in good agreement with values for close packed crystals close to melting [13-16]. We also determined the diffusion coefficient D_{lq} of fluid particles from their mean square displacement using

$$\langle r^2 \rangle \sim 4 D_{lq} t \qquad (3.2)$$

A value of $D_{lq} = 0.052\ \mu m^2/s$ is obtained from the best linear fit (Fig.3.4b). The velocity of diffusion-limited growth can be estimated according to [17]

$$v_{dl} = 4 D_{lq} / d. \qquad (4.3)$$

Using the measured diffusion coefficient, we obtain $v_{dl} = 0.3\ \mu m/s$. This value is a factor of 3 larger than the observed growth velocity $v = 0.1\ \mu m/s$ indicating that the growth is not limited by diffusion, but rather by the rate of attachment of particles at the crystal surface. The difference between both values allows estimation of the amount of supersaturation of the crystallizing suspension. Assuming Wilson-Frenkel growth, we determine the chemical potential difference $\Delta\mu$ between fluid and crystal according to [17-19]

$$\Delta\mu = -\ln\left(\frac{v_{dl} - v}{v_{dl}}\right) k_B T \qquad (3.4)$$

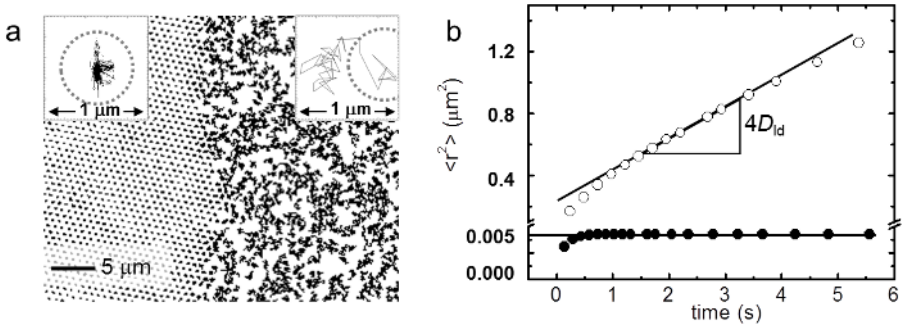

Figure 3.4: Particle trajectories and mean square displacement.

(a) Trajectories of particles in the crystal (left) and fluid (right). Inset: enlargement of a single particle trajectory for a particle in the crystal (top left) and fluid (top right). (b) Mean square displacement as function of time for particles in the crystal (filled dots) and fluid (open dots). The mean square displacement of crystal particles saturates at a value of 0.0086 μm^2 (solid line, bottom), while that of fluid particles increases linearly with time (solid line, center) indicating diffusion. The slope equals four times the diffusion coefficient.

Using the experimentally measured values for v_{dl} and v, we find $\Delta\mu = 0.41\ k_B T$, a small amount of supersaturation that indicates that the growth occurs close to the equilibrium freezing transition [17, 20, 21]. This value is in good agreement with simulation values between 0.2 and 0.5 $k_B T$ for crystallizing soft spheres [22], and is of the same magnitude as hard-sphere simulation values predicted for ϕ~0.52 [23], well in the crystal-fluid coexistence regime.

3.4 Crystal growth stability

The stability of crystal growth is important because it defines the quality and the morphology of the final crystal. Here, we investigate the role of the interfacial free energy in stabilizing the crystal growth. This is done by adding "impurity particles" that act as obstacles and pin the advancing interface. We add impurity particles of two different sizes, with radii $R_1 \sim 2d$ and $R_2 \sim 3d$, and follow the interface with time starting from the moment where the interface reaches the edge of the impurities. Reconstructed images of the advancing interface are shown in Fig.3.5. Gray dots indicate particles in the crystal while open circles indicate particles in the fluid. The black line indicates the advancing fluid-

crystal interface, and the two large gray dots show the impurity particles. We observe that both impurities pin the interface; however, while the small impurity is easily overcome by the interface, the larger impurity holds the advancing interface back and causes it to bow strongly (Fig. 3.5b and c), before finally impurity is overcome and the interface retracts.

The interface curvature leads to a local force that drives the interface across the obstacle. This force is

$$F = PA_{\text{eff}} . \qquad (3.5)$$

Here A_{eff} is the effective contact area between the interface and the obstacle, and P can be estimated from the Laplace pressure

$$P_{\text{LP}} = 2\gamma / R_C \qquad (3.6)$$

with γ is the interfacial free energy, and R_{C} is the radius of curvature of the pinned interface. The interface overcomes the impurity when the driving force F becomes larger than F_{obst}, the critical force required to surmount the obstacle. This critical force is

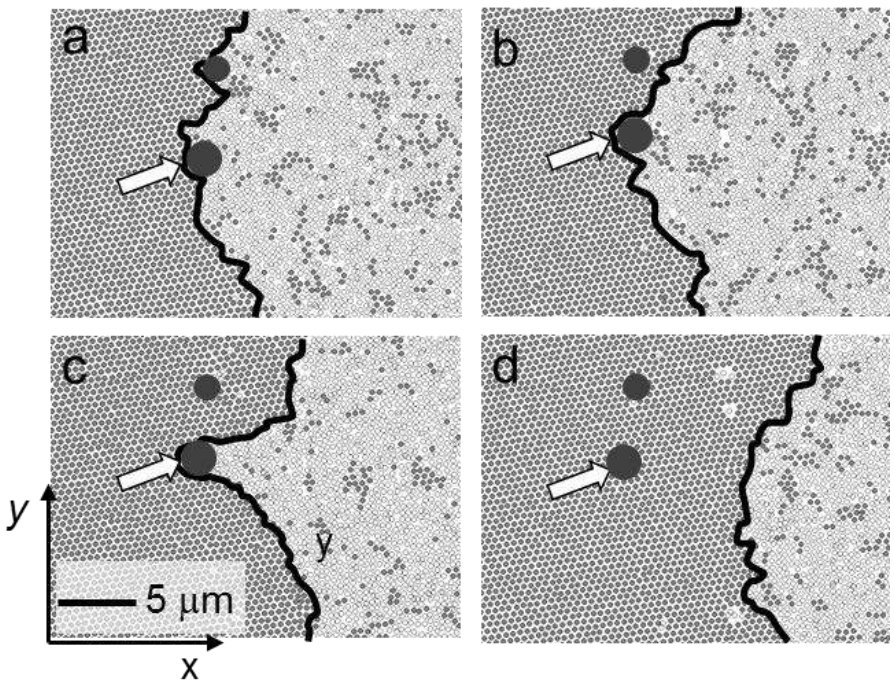

Figure 3.5: Crystal growth across impurities.

(a)–(d) Sequence of reconstructed images showing the advancing solid-fluid interface surmounting impurity particles (dark gray spots): Interface touching the impurities (a), surmounting the small impurity (b), pinned by the large impurity (c), and final straightening of the interface after successful transgression (d).

$$F_{obst} \sim 2\gamma A_{eff} / R_c \qquad (3.7)$$

where we take $R_c \sim R_2$ and the contact area

$$A_{eff} = (4\pi R_2)^2 / 2 \qquad (3.8)$$

By using a typical value of the interfacial free energy of these colloidal crystals, $\gamma = 0.71 k_B T / d^2$ (see chapter 4), we obtain $F_{obst} = 1.6 \cdot 10^{-13}$ N. Interestingly, this force is of the same order as that measured for dislocation motion through a dense colloidal crystal [24]. When $F > F_{obst}$, the interface overcomes the impurity, and it quickly retracts and flattens, thereby minimizing its energy cost (Fig. 3.5d).

3.5 Conclusions

The temperature sensitivity of pNipam hydrogel particles allows excellent control to guide macroscopic crystal growth. We have shown that in analogy to atomic crystal growth, large macroscopic pNipam colloidal crystals grow in a temperature gradient when the suspension is cooled slowly so that only a few crystal nuclei form initially. We followed the growth directly and determined a chemical potential difference of $\Delta\mu = 0.41\ k_B T$ between crystal and fluid phases indicating that the growth occurred close to equilibrium with only moderate undercooling.

By adding impurities with different sizes to the advancing interface we examined the role of the interfacial tension to stabilize of the crystal growth. We also estimate the Laplace pressure and the critical driving force required to surmount the obstacle. The magnitude of this force is 160 fN, which is the same order as the force measured for dislocation motion through a dense colloidal crystal.

Bibliography

[1] J. D. Joannopoulos, P. R. Villeneuve and S. Fan, " Photonic crystals: putting a new twist on light," *Nature ,* vol. 386, p. 143, 1997.

[2] G. Pan, R. Kesavamoorthy, and S. A. Asher, "Optically nonlinear Bragg diffracting nanosecond optical switches,," *Phys. Rev. Lett.,* vol. 78, p. 3860, 1997.

[3] J. H. Holtz, and S. A. Asher, "Polymerized colloidal crystal hydrogel films as intelligent chemical sensing materials," *Nature,* vol. 389, p. 829, 1997.

[4] P. Pusey and W. van Megen, "Phase behavior of concentrated suspensions of nearly hard colloidal spheres," *Nature,* vol. 320, p. 340, 1986.

[5] P. Pusey, in Liquids, Freezing and the Glass Transition, Amsterdam: Elsevier, 1991.

[6] W. C. K. Poon, and P. N. Pusey, in Observation, Prediction and Simulation of Phase Transitions in Complex Fluids, Boston: Kluwer Academic, 1995.

[7] A. D. Dinsmore, J. C. Crocker, and A. G. Yodh, "Self-assembly of colloidal crystals," *Curr. Opin. Colloid Interface Sci.,* vol. 3, p. 5, 1998.

[8] D. G. Grier, "From dynamics to device: directed self-assembly of colloidal materials," *MRS Bull,* vol. 23, p. 21, 1998.

[9] A. van Blaaderen, R. Ruel, and P. Wiltzius, "Template-directed colloidal crystallization," *Nature,* vol. 385, p. 321, 1997.

[10] J. Zhu, M. Li, R. Rogers, W. Meyer, R. H. Otteewill, W. B. Russel, and P. M. Chaikin, "Crystallization of hard-sphere colloids in microgravity," *Nature,* vol. 387, p. 883, 1997.

[11] E. R Weeks , J. C. Crocker, A. C. Levitt, A. B. Schofield, and D. A. Weitz, "Three-dimensional direct imaging of structural relaxation near the colloidal glass transition," *Science,* vol. 287, p. 627, 2000.

[12] A. M. Alsayed, M. F. Islam, J. Zhang, P. J. Collings, A. G. Yodh, "Premelting at defects within bulk colloidal crystal," *Science,* vol. 309, p. 1207, 2005.

[13] F. A. Lindemann, *Z. Physik,* vol. 11, p. 609, 1910.

[14] R. Cahn, "Melting from within," *Nature,* vol. 413, p. 582, 2001.

[15] D.A. Young and B.J. Alder, "Studies in molecular dynamics. XIII. Singlet and pair distribution functions for harddisk and hardsphere solids," *J. Chem. Phys.,* vol. 60, p. 1254, 1974.

[16] R. Ohnesorge, H. Löwen and Wagner, "Density distribution in a hard-sphere crystal," *Europhys. Lett.,* vol. 22, p. 245, 1993.

[17] D. J. W. Aastuen, N. A. Clark, L. K. Cotter, and B. J. Ackerson, "Nucleation and growth of colloidal crystals," *Phys. Rev. Lett.,* vol. 57, p. 1733, 1986.

[18] H. Wilson, *Philos. Mag.,* vol. 50, p. 238, 1900.

[19] J. Frenkel, *Phys. Z. Sowjetunion,* vol. 1, p. 498, 1932.

[20] M. Würth, J. Schwarz, F. Culis, P. Leiderer, and T. Palberg, "Growth kinetics of body centered cubic colloidal crystals," *Phys. Rev. E,* vol. 52, p. 6415, 1995.

[21] T. Palberg, "Crystallization kinetics of repulsive colloidal spheres," *J. Phys., Condens. Matter,* vol. 11, p. R323, 1999.

[22] S. Auer, W. C. K. Poon, and D. Frenkel, "Phase behavior and crystallization kinetics of poly-12-hydroxystearic-coated polymethylmethacrylate colloids," *Phys. Rev. E,* vol. 67, p. 020401, 2003.

[23] S. Auer, and D. Frenkel, "Numerical prediction of absolute crystallization rates in hard-sphere colloids," *J. Chem. Phys.,* vol. 120, p. 3015, 2004.

[24] P. Schall, I. Cohen, D. A. Weitz, F. Spaepen, "Visualization of dislocation dynamics in colloidal crystals," *Science,* vol. 305, p. 1944, 2004.

Chapter 4

Visualizing the structural solid-fluid transition and free energy at colloidal crystal-fluid interfaces

The interfacial free energy between a crystal and its melt is an important parameter that determines crystal nucleation and growth. The origin of this interfacial free energy is mostly entropic, and results from the change of order from the long-range order of the crystal to the short-range order of the liquid. In this chapter, we report the direct measurement of the interfacial free energy and its small anisotropy from thermally equilibrated crystal-fluid interfaces using pNipam microgels as a model system [1-5]. We use three-dimensional imaging of the equilibrium crystal-fluid interface to obtain insight into the structural transition from the liquid to the crystal. We measured the corresponding interfacial free energy barrier directly by implementing a new method to relate structure and free energy. Finally, we resolve the small anisotropy of the interfacial free energy by directly following thermally induced interface fluctuations of crystal fluid interfaces in different orientations.

4.1 Introduction

The hallmark of the crystal is its maximal global density, which results from a periodic filling of space. In contrast, the liquid maximizes its short-range density by forming local close packed configurations [6, 7]. It has been argued that for simple monatomic liquids, maximum short-range density is achieved with icosahedral configurations [6]. These icosahedral units exhibit five-fold rotational symmetry that is incompatible with a periodic filling of space [8]. This incompatibility leads to the first-order transition that separates solid and liquid phases [9]. At the interface to the solid, the number of possible packing configurations of the liquid is reduced with respect to the bulk liquid, resulting in a loss of configurational entropy; this loss of configurational entropy provides the dominant contribution to the interfacial energy [10]. The structural transition is therefore central to our understanding of the interfacial energy. In atomic liquids, sophisticated scattering and electron microscopy [11-13] measurements have been used to elucidate it; however, the change of liquid configurations at the interface to the solid is extremely difficult to image in atomic system, and the direct measurement of the structure-dependent free energy barrier remained elusive.

We used colloidal poly-N-isopropylacrylamide (PNIPAM) particles to obtain direct images of the short-range order of the liquid at the interface to the solid. The PNIPAM and its derivative particles have the advantage that their size is directly controlled with temperature, allowing direct control over crystal growth and melting [14] and glass-formation [15]. These particles enabled us to achieve large, equilibrated crystal-fluid interfaces that are well suited to elucidate the structural crystal-fluid transition. The crystal growth was studied in the last chapter. Here, we focus on the stationary interface after the crystal has been fully grown. We switched off the temperature gradient, and use confocal microscopy to image the equilibrium crystal-fluid interface on the particle scale. We show that the predominant building blocks of the liquid are large fragments of icosahedra that are broken and reformed by thermal fluctuations, and we elucidate changes of the short-range order as we approach the crystal. We establish a direct link between the structure and the free energy to measure the free energy change across the interface directly from the three-dimensional particle configurations [16]. The resulting interfacial energy is $\gamma \sim 0.65 k_B T$ per particle, in very good agreement with simulation results of slightly soft spheres. We then use thermal fluctuations of the interfaces to resolve even the small

anisotropy of the interfacial tension. We obtain an anisotropy of ~2%, surprisingly larger than values obtained in simulations.

4.2 Free energy measurement of hard sphere configurations.

The free energy of hard-sphere systems is directly related to the geometry of the packing, and can be determined conveniently from the positions of the particles [16]. The free energy measurement is based on the insertion of an additional particle into the given particle packing. To find the free regions available for the insertion of an additional particle, exclusion spheres are created around the particles; these exclusion spheres have a radius of one particle diameter and demarcate the region from which the center of the additional particles is excluded. The volume unoccupied by the excluded spheres is defined as available volume V_0 to insert the additional sphere into the system without disturbing its neighbors. The surface area of this volume is defined as available surface area A_0, (see Fig.4.1).

In thermal equilibrium, the reversible work per unit volume needed to squeeze an extra particle into a volume V_0 is related to the pressure p and it is expressed in terms of A_0 and V_0 as

$$p = \rho k_B T [1 + (rA_0/3V_0)] \qquad (4.1)$$

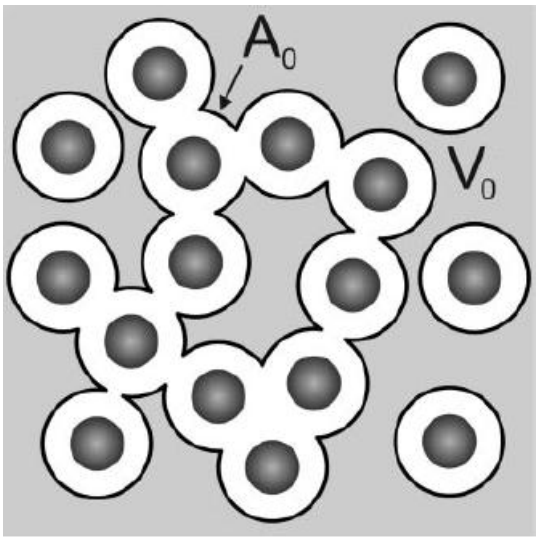

Figure 4.1: A 2D illustration of V_0 (gray area) and A_0 (black lines). The dark and white circles, respectively, represent the hard spheres and the corresponding excluded volume spheres [16].

where ρ is the particle number density and r is the particle radius. On the other hand, the energy required for adding an extra particle into the system is the chemical potential μ and it is determined as

$$\mu = \mu_0 - k_B T \ln(V_0/V) \qquad (4.2)$$

where μ_0 is ideal gas chemical potential and V is the total volume of the system. The free energy per unit volume is directly determined from the pressure and the chemical potential as

$$f = -p + \mu\rho \qquad (4.3)$$

In principle, using this method, all thermodynamic quantities are determined just using particle geometry in real space. This has been exploited in recent confocal microscopy measurements by Dullens *et al* [16]. They used confocal microscopy to obtain three-dimensional snapshots of a colloidal hard-sphere suspension. From the experimental snapshots, particle positions are located using a particle tracking software and the excluded spheres are defined and mapped onto a fine lattice. Three types of lattice sites (pixels) are distinguished from which V_0 and A_0 are directly determined: A_0 equals the number of lattice sites at the edges of the excluded volume spheres, and V_0 equals the remaining lattice sites outside the excluded volume spheres. The resulting values of free energy determined with equations (4.1) to (4.3) is in good agreement with the results of Monte Carlo simulation and the free energy obtained from integration of the Carnahan-Starling equation of state.

We use this method to measure the free energy change across crystal fluid interfaces directly from the structure; this free energy change can then directly be related to the interfacial free energy using Gibb's argument of the dividing surface between two thermodynamic phases.

4.3 Measurement of anisotropy of the crystal-fluid interfacial tension.

The anisotropy of the interfacial free energy of crystal-fluid interfaces is a crucial parameter that determines the morphology of the growing crystal and the morphological stability of the growth. However, the anisotropy is difficult to measure since it is small, typically of the order of a few percent of the interfacial free energy. Therefore, direct

measurements of the free energy such as the one discussed in the last section, cannot resolve this small anisotropy. Recently, Hoyt *et al.* presented a method to compute accurately the crystal-fluid interfacial tension γ and its weak anisotropy from the orientation-dependent fluctuations of the interfaces [17]. The method is based on monitoring interfacial fluctuations to extract the interfacial stiffness which is typically an order of magnitude more anisotropic than the interfacial tension itself.

In thermal equilibrium, interface fluctuations are described by interface waves along the y-direction as

$$x = A_q \exp(iqy), \tag{4.4}$$

were A_q is the Fourier amplitude of the interface height fluctuation with wave vector q. These fluctuations increase the interfacial free energy by

$$\Delta F = \frac{1}{2} A_q \left(\gamma + \gamma^{"}\right) bl \tag{4.5}$$

Here it is assumed that the thickness of the interface b is much smaller than the width l of the imaged section [2,17]. The term $\gamma + \gamma^{"}$ corresponds to the interfacial stiffness, where $\gamma^{"}$ is the second derivative of γ as a function of the angle α of the local interface normal relative to its average orientation. Note that $\gamma^{"}$ originates from the energy cost of bending locally the interface away from its macroscopic orientation. That is the reason why the fluctuation spectrum measures directly the stiffness. Because of the equipartition, in thermal equilibrium energy mode is excited with thermal energy, k_BT. Therfore, the interfacial stiffness is related to the mean square of the Fourier amplitude as

$$\langle |A_q|^2 \rangle = \frac{k_B T}{bl(\gamma+\gamma^{"})q^2} \tag{4.6}$$

By measuring the spectrum of interfacial fluctuations, we can directly measure the interfacial stiffness $(\gamma + \gamma^{"})$. The crystals made up of colloidal pNipam particles consist of a random stacking of hexagonal close-packed layers (see chapter 3). Such random hexagonal close-packed (rhcp) crystals exhibit sixfold symmetry around the axis perpendicular to the hcp planes. The interfacial tension thus depends on the angle α between a crystal lattice direction and the normal to the interface within the hcp plane as

$$\gamma(\alpha) = \gamma_0(1 + \epsilon \cos 6\alpha). \tag{4.7}$$

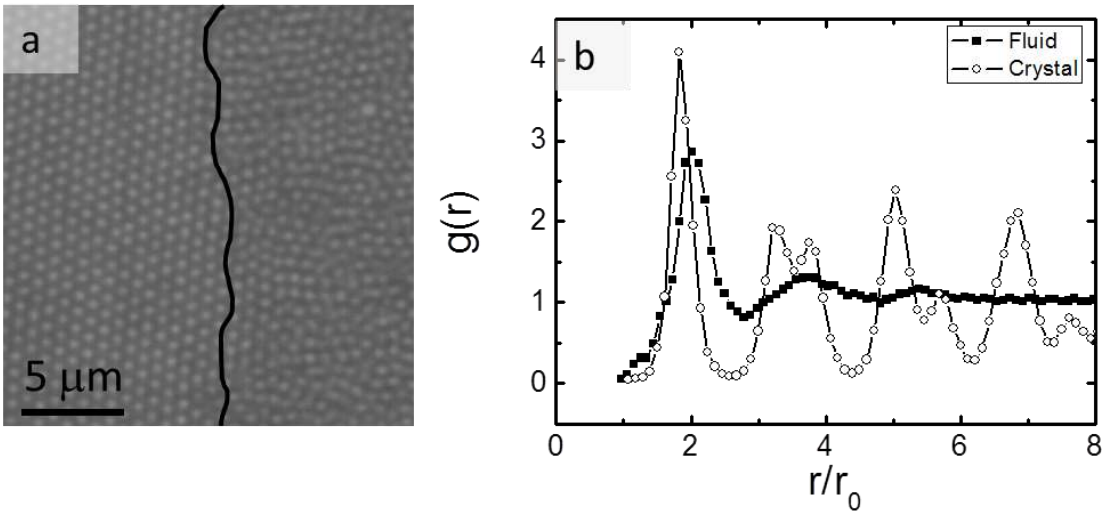

Figure 4.2: Crystal and fluid. (a) Confocal microscope image of crystal (left) and fluid (right) focussed at the interface (solid line). (b) Pair correlation function of a colloidal crystal (open circles) and a colloidal fluid (solid squares).

Here γ_0 and ε are the average interfacial tension and its anisotropy, respectively. The orientation-dependent interfacial stiffness follows as

$$\gamma + \gamma'' = \gamma_0(1 - 35\epsilon \cos 6\alpha) \qquad (4.8)$$

The last equation indicates that the anisotropy of the interfacial *stiffness* is 35 times larger than the anisotropy of interfacial *tension* itself. Therefore, measuring the anisotropy of interfacial stiffness can be measured with high accuracy.

4.4 Colloidal crystal-fluid equilibrium and particle configurations

In the following, we describe our direct observations of the equilibrium crystal-fluid interface. We use the crystals growth procedure outlined in the previous chapter to nucleate and grow crystal following a fixed temperature protocol (see Fig. 3.1a). After a few hours, a few crystals have grown to centimeter lengths. By holding the sample at $T = 34°C$ and switching off the temperature gradient, we achieve equilibrium of macroscopic crystal and liquid phases separated by a stationary interface. We use confocal microscopy to image individual particles in a 65 μm by 65μm by 20 μm volume at the interface, and determined their positions with an accuracy of ~0.02 μm in the horizontal and ~0.03 μm in the vertical direction. To obtain this high accuracy, we used full 1024 by

1024 pixel images with a pixel density of 250 μm^{-2}, a factor of 4 higher than usually achieved. A small section of a confocal image is shown in Fig.4.2a. A clear distinction between crystal (left) and fluid (right) is observed. We measure the pair correlation functions *g(r)* of particles on the left and on the right side of the image separately and show the results in Fig. 4.2b. Open circle symbols, corresponding to *g(r)* of particles on the left, show characteristic peaks of the hcp crystal plane while solid square symbols, corresponding to *g(r)* of particles on the right, show the characteristic short range-order of the fluid.

To pinpoint the interface, we distinguish crystal and fluid particles from their nearest-neighbor environment. For each particle, we find the nearest neighbors as those separated by less than the first minimum of the crystal pair correlation function. The nearest neighbor vectors, $\boldsymbol{d_i}$, are then compared with those of the reference crystal lattice, $\boldsymbol{D_i}$. Deviations from the reference positions are determined using the order parameter

$$\delta^2 = \frac{1}{12}\sum_i |d_i - D_i|^2 \ , \qquad (4.9)$$

the mean square difference between the actual and the average crystal nearest neighbor vectors [17] (see Fig.4.3a). We plot the average order parameter as a function of *x* in Fig. 4.3b. In the crystal, the normalized order parameter $(\delta_{cryst}/d)^2 \sim 0.02$, reflecting the small lattice distortions due to thermal fluctuations, while in the fluid, $(\delta_{fl}/d)^2 \sim 0.12$, demonstrating the loss of crystalline order. The order parameter appears constant on both

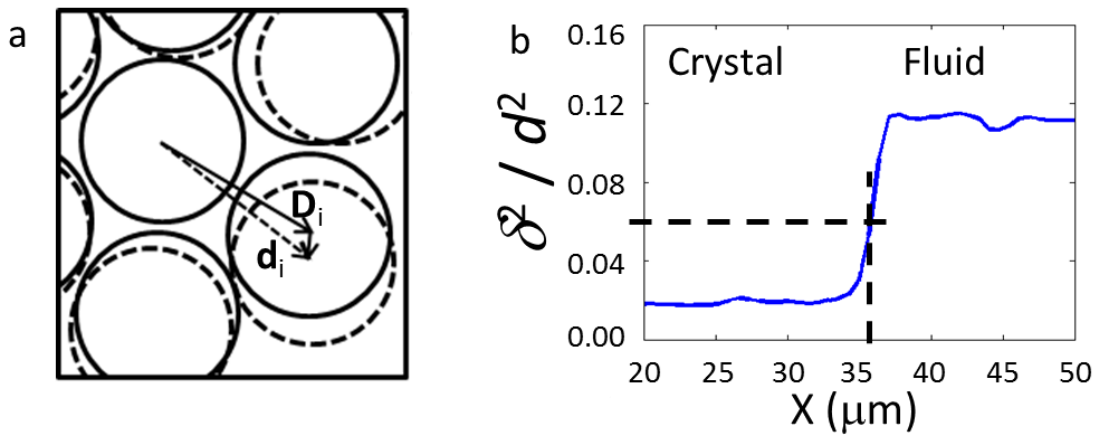

Figure 4.3: Order parameter. (a) Illustration of the determination of the order parameter from the nearest-neighbor vectors $\boldsymbol{d}_i$, and the reference vectors $\boldsymbol{D}_i$. (b) Order parameter as a function of *x* across the interface. The dashed lines indicate the interface position.

crystal and fluid sides and shows a sharp rise at $x \sim 35.5\,\mu m$, indicating the crystal-fluid interface. We use this rise of δ^2 to define the interface position and distinguish crystal and fluid particles (see dashed lines in Fig. 4.3b).

We plot a 40 µm by 35 µm by 15 µm reconstruction of the crystal-melt equilibrium in Fig. 4.4a. Large red spheres indicate particles with $(\delta/d)^2 < 0.07$, while small blue spheres indicate particles with $(\delta/d)^2 > 0.07$. Red spheres demarcate the regular crystal lattice for $x < 33\,\mu m$, while blue spheres reveal the disordered structure of the liquid for $x > 38\,\mu m$. We observe that, even on the fluid side, small patches of red particles appear indicating spontaneously ordered particle configurations that are not stable and disappear. Fig.4.4a shows the coexisting bulk crystal and fluid phases, and their interface. To show the interface more clearly, we reconstructed the two-dimensional interfacial surface as the

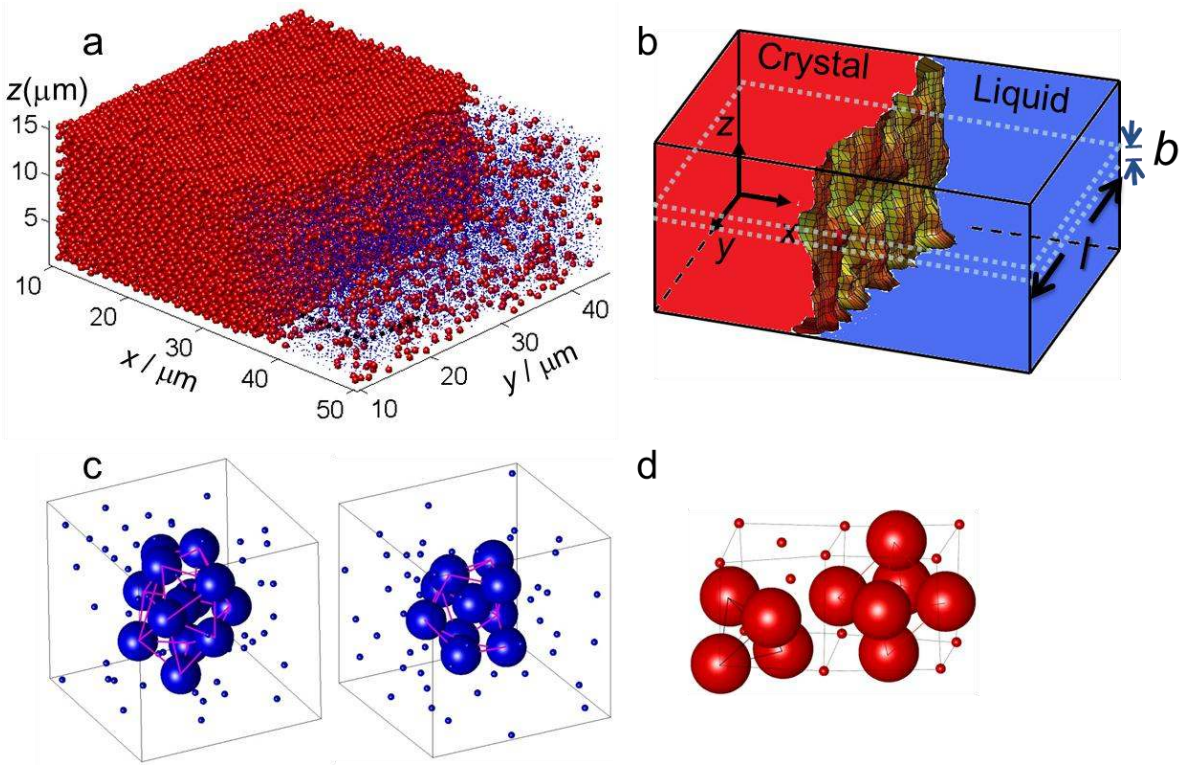

Figure 4.4: Reconstruction of crystal and fluid and their interface. (a) 40 µm × 35 µm × 15 µm reconstruction of the crystal–fluid equilibrium. Large red spheres show particles with a crystalline environment and small blue spheres show particles with a fluid environment. Fluid particles are depicted with small spheres for clarity. (b) Reconstructed solid/fluid interfacial plane. The interface roughness is roughly five particle diameters. (c,d) Particle configurations in the colloidal fluid and crystal. (c) Icosahedrally coordinated particles (large spheres, left) and fragment of an icosahedron consisting of 10 particles (large spheres, right) embedded in the colloidal fluid. (d) Tetraherdral (left) and octahedral configurations (right) in two unit cells of the face-centered cubic lattice.

surface along which $(\delta/d)^2 \sim 0.07$. In more detail, we divided the image volume into cubes of size $a = 0.5d$, and calculate the average order parameter for each cube from the order parameter values of all particles with centers within $2d$ of the center of the cube. We then connect the centers of all cubes with order parameter values $\delta^2 \sim 0.07d^2$. A reconstruction of the interface is shown in figure 4.4b. The interface is rough, due to thermally excited interface fluctuations. Its width is about five particle diameters.

The direct three-dimensional imaging of the interface provides a unique opportunity to investigate how the long-range order of the crystal goes over into the short-range order of the fluid. To elucidate the structural solid-fluid transition, we investigated local packing configurations at the interface. We connected the centers of nearest neighbor particles into polyhedra, and identified tetrahedral and octahedral particle configurations, which have been suggested to be local building blocks of liquid and crystal [7]. Reconstructions of local configurations in the fluid and crystal are shown in Fig. 4.4c and Fig.4.4d, respectively. The figures show particles with tetrahedral coordination in the fluid (large blue spheres in Fig. 4.4c) and with tetrahedral and octahedral coordination in the crystal (large red spheres on the left and right of Fig.4.4d, respectively). In the fluid, tetrahedral configurations join into units of 13 particles (Fig. 4.4c, left) or less (Fig. 4.4c, right). We

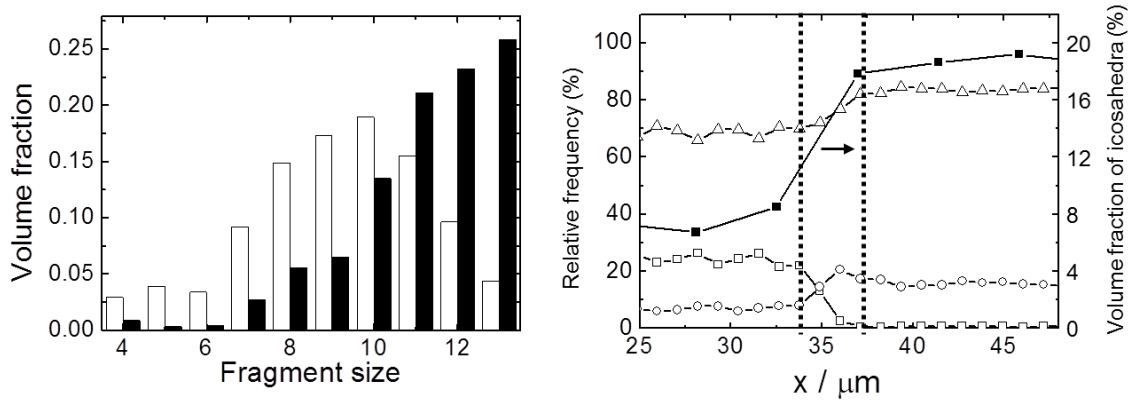

Figure 4.5: Relative frequency of particle configurations: icosahedral fragments, octahedra, and tetrahedra. (a) Relative volume occupied by icosahedral fragments as function of fragment size in the colloidal fluid (open bars) and in a close-packed suspension of millimeter-sized particles (solid bars). (b) Relative frequency of particle configurations as a function of x across the interface: tetrahedral configurations (triangles), octahedral configurations (squares), and other polyhedral configurations (pentagons). Also shown is the volume fraction of icosahedral fragments with size larger than 10 particles (solid squares and scale on the right).

identified these units as complete and fragmented icosahedra, respectively. Because of particle diffusion, however, the neighborhood of a particle changes rapidly giving rise to a relative change of the fragment size in the colloidal fluid. We focused on a single three-dimensional image stack to determine the relative volume occupied by icosahedral fragments of a particular size. We plot the volume fraction as a function of fragment size in Fig. 4.5a (open bars). Remarkably, full icosahedra occur only rarely, and icosahedral fragments containing ~10 particles are most frequent. We also investigated a random close packed suspension of millimeter-size, athermal particles of similar polydispersity [18], and find that in this athermal suspension, complete icosahedra occur most often, in contrast to the colloidal fluid (Fig. 4.5a solid bars). This difference suggests that in the colloidal fluid, icosahedral configurations are constantly broken by thermal fluctuations. Moreover, in contrast to the crystal, no single octahedral configuration is observed in the fluid indicating the strong preference of the fluid for maximum short-range density.

To elucidate the structural transition from solid to liquid, we determine the number of tetrahedral, octahedral, and icosahedral configurations as a function of x. We pinpoint the center of mass of each polyhedron, bin the centers of all polyhedra in 2 μm intervals along the x-direction, and determine the relative number of polyhedra for each interval. Their relative frequency as a function of x is shown in Fig. 4.5b. A sharp rise in the number of tetrahedra and icosahedra demarcates the transition from the solid to the fluid at $x \approx 35.5\mu m$, in good agreement with the interface position determined from the order parameter. Towards the crystal, the relative frequency of tetrahedra and octahedra approaches that of ~70% and 30%, in good agreement with the relative frequency of 2/3 and 1/3, expected for face-centered cubic crystals [10]. The change from the characteristic packing of the liquid to that of the crystal occurs within ~3.5 μm corresponding to ~5 particle diameters, in good agreement with estimates from particle density profiles [19].

4.5 Measurement of free energy at colloidal crystal-fluid interfaces

The three-dimensional imaging of liquid configurations allows us to directly measure the free energy change at the interface. To achieve this, we measure the free volume V_0 and the free surface area A_0 available for insertion of additional particles (chapter 4.2). We

determine the effective radius of the particles from their average nearest neighbor distance d_{nn} in the crystal using

$$r_{\mathrm{eff}} = (d_{nn}/2)\,(\phi_{\mathrm{m}}/\phi_{\mathrm{cp}})^{1/3} \qquad (4.10)$$

where we used ϕ_m=0.54 and ϕ_{cp}=0.74, the volume fractions of hard-sphere crystals at melting and close packing, respectively. The resulting value $r_{\mathrm{eff}} = 0.35$ μm agrees well with static light scattering measurements in dilute suspensions, and is roughly 30% smaller than the hydrodynamic radius $r \sim 0.5$ μm determined with dynamic light scattering, indicating that these particles are still slightly compliant [20, 21] . We show the resulting particle volume fraction, ϕ as a function of x, determined from particle counting in Fig. 4.7a. Within an interfacial region of width ~5 d, the volume fraction changes between the values $\phi_{\mathrm{m}} \sim 0.54$ and $\phi_{\mathrm{f}} \sim 0.49$, the melting and freezing volume fractions of hard spheres [22].

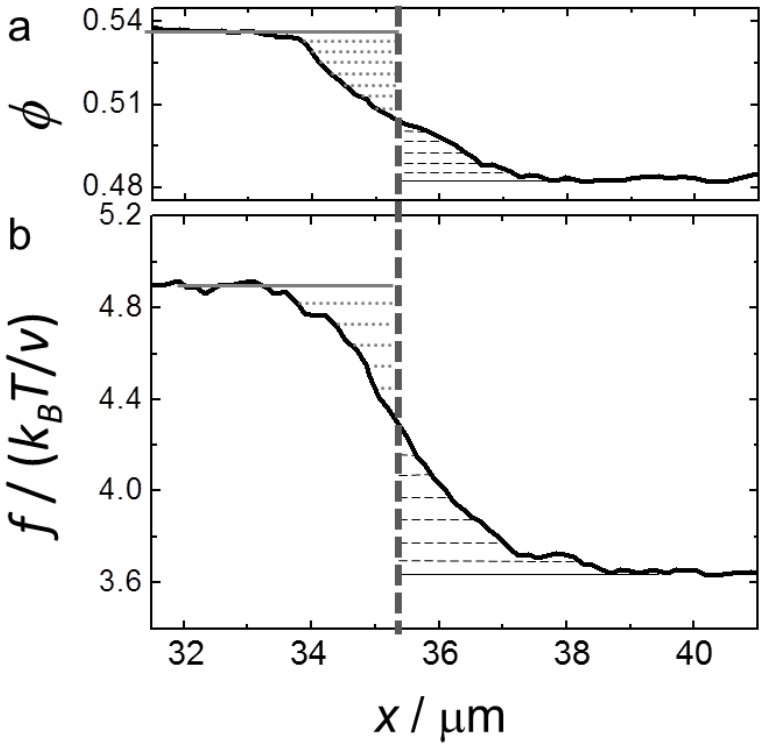

Figure 4.6: Free energy change at the interface. (a) Particle volume fraction as a function of x. The interface (vertical dashed line) is determined by balancing the number of excess and deficit particles in the liquid and solid, respectively (dot and dash shaded areas in a). (b) Free energy density as a function of x. The black solid curve shows the measured free energy, and the solid lines show the hypothetical values in Gibbs' model.

To determine the free energy as a function of distance to the interface, we focus on thin sections parallel to the interface and measure the total V_0 and A_0 in these sections. We then use equations (4.1) – (4.3) to determine the free energy for each section. The resulting free energy density, f, as a function of x is shown in Fig. 4.6b. The free energy density drops from $4.9\,(k_BT/v)$ to $3.6\,(k_BT/v)$, in agreement with the expected free energy density difference $\Delta f \approx 1.5\,(k_BT/v)$ of hard-sphere crystal-fluid equilibrium [23]. Here, $v = \pi d^3/6$ is the particle volume. This decrease of the free energy density reflects the increasing entropy associated with the increasing number of packing configurations towards the liquid. We can now determine the interfacial free energy: It is defined as the difference in free energy between the system containing the interface, and a hypothetical reference system, in which the bulk free energy of crystal and liquid are extended up to the dividing surface [24] (dot and dash lines in Fig. 4.6b). We pinpoint the position of this hypothetical surface by balancing the number of excess particles in the fluid (dot shaded area in Fig.4.6a) with the number of deficit particles in the crystal (dash shaded area). We obtain the interface position $x_I = 35.4\,\mu m$ (dash vertical line in Fig. 4.6), in very good agreement with the position determined from the order parameter. Unlike the number of particles, the excess and deficit free energies in fluid and crystal (dash and dot shaded areas in Fig. 4.6b) do not balance, and exhibit a net excess on the fluid side. This excess free energy per unit area is the interface tension, γ. We obtain a value of $\gamma = 0.65\,k_BT/d^2$ by numerical integration, in good agreement with values found in simulations of hard and slightly soft-spheres [25], which are between 0.50 and $0.8 k_BT/d^2$.

4.6 Direct measurement of the anisotropy of the crystal-fluid interfacial free energy

Because of its structural origin, the interface tension depends on the direction of the interfacial plane with respect to the crystal lattice, and is anisotropic. This anisotropy plays an important role in crystal nucleation and the morphological stability of crystal growth; however, its direct experimental measurement is prohibitively difficult, and this anisotropy has mostly been inferred from macroscopic measurements [26]. We used thermally excited interface fluctuations to measure the small anisotropy of the interface tension directly [17, 27]. We acquired 200 images, and followed the fluctuations of the one-

dimensional trace of the interface. A reconstructed image focusing on the interface is shown in Fig. 4.7a. Gray dots show particles with order parameter values $\delta^2<0.07d^2$, while open circles indicate particles with $\delta^2>0.07d^2$. The black line is obtained by connecting all points with order parameter $\delta^2 \sim 0.07d^2$, and indicates the trace of the crystal-fluid interface in the plotted section. A few traces of reconstructed interfaces are shown in fig. 4.7b. The solid black line indicates the time-averaged interface while the gray lines indicate instantaneous interface profiles. These results show that the interface strongly fluctuates around its average position. We determine the average spectrum A_q of interfacial fluctuations by Fourier transformation of the individual interface profiles. This analysis is then repeated for several different interface orientations to determine the orientation-dependent interface stiffness. Average interface spectra $\langle|A_q|^2\rangle$ as a function of q^2 for

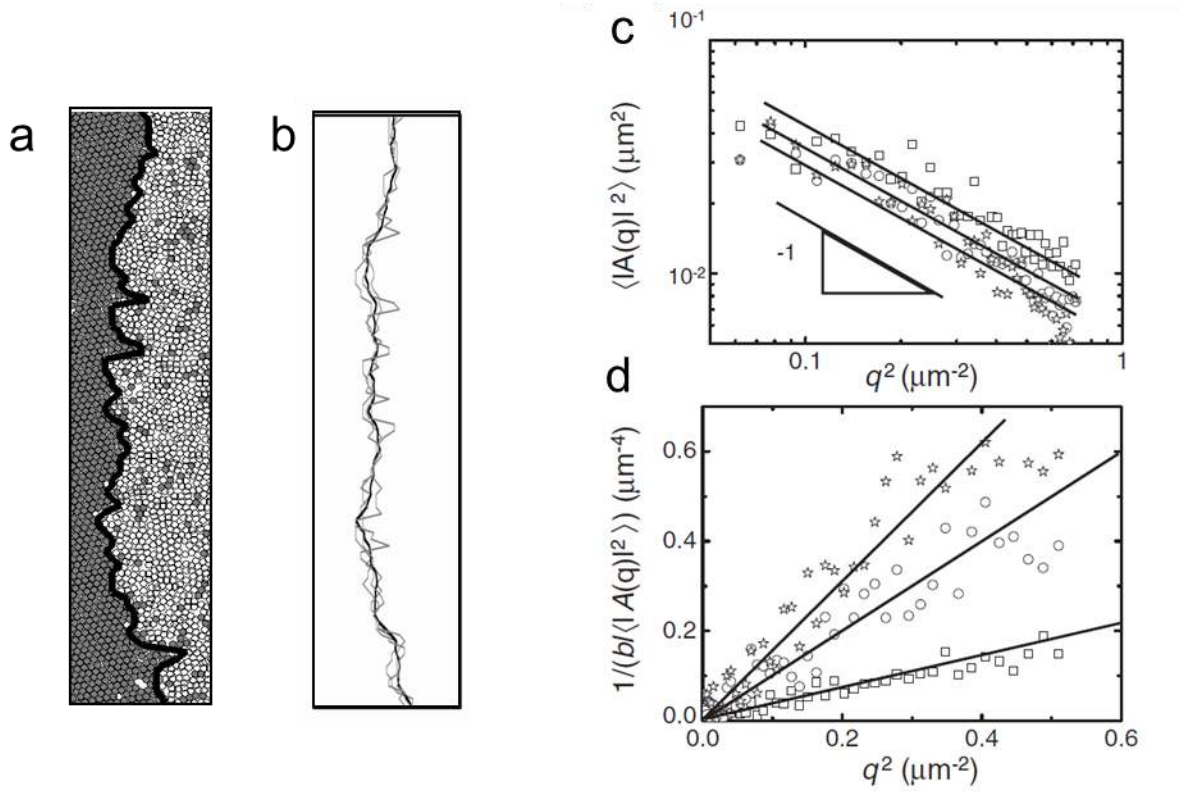

Figure 4.7: Equilibrium interface and interface fluctuations. (a) Reconstruction of the crystal-fluid equilibrium and interface. Gray dots represent particles with a crystalline environment, while circles represent particles with a fluid-like environment. The black solid line indicates the interface. (b) Snapshots of the interface (gray) demonstrating fluctuations around the average position (black). (c) Log-log plot of the fluctuation spectra for the crystal orientations α = 2◦ (squares), 10.5◦ (circles), and 14.9◦ (stars). The solid lines indicate a slope of –1. (d) $1/bl\langle|A(q)|2\rangle$ vs q^2 for the three crystal orientations. The solid lines indicate best linear fits to the data.

three selected interface orientations are shown in Fig. 4.7c. The data confirms the decay $A_q^2 \propto q^{-2}$ for all orientations. We notice a systematic shift of the data in the double-logarithmic representation; this shift indicates the change of the interface stiffness with orientation. To determine the corresponding stiffness values, we plot $(<|A_q|^2> lb)^{-1}$ as a function of q^2 in a linear representation in Fig. 4.7d. A clear distinction of three slopes indicates the clear difference of interfacial stiffness for the three orientations. Values of the interface stiffness are obtained from the best linear fit to the data (solid lines in Fig. 4.7d). We analyzed interfacial spectra of many more interface orientations and show the corresponding stiffness values and error margins, obtained from a linear regression analysis of the data in table 1. These values vary systematically with crystal orientation. Our measured values are in excellent agreement the expected dependence (4.7) and (4.8) of the hexagonal symmetry as shown by plotting the interface stiffness as a function of α in Fig. 4.8a.

From the best fit with Eq.4.8 (solid line), we obtain values of $\gamma_0 = (0.70 \pm 0.05)\, k_B T / d^2$ and $\varepsilon = (0.016 \pm 0.004)$. The value of γ_0 is in good agreement with the value obtained from the direct free energy measurement and with values determined in simulations of soft sphere colloidal crystal-fluid interfaces, which are between 0.55 and 0.8 $k_B T/d^2$ depending on the particle softness [28]. The magnitude of the anisotropy, however, is much larger than simulation values of anisotropies within the hexagonal close-packed plane. By using the directions $[\bar{1}10]$ and $[\bar{2}11]$ for the face centered cubic (fcc) lattice, we determine that

Angle α (Degree)	$(\gamma + \gamma'')(k_B T/d^2)$
2.0	0.19 ± 0.02
10.5	0.49 ± 0.05
14.3	0.74 ± 0.08
14.9	0.73± 0.08
24.0	1.13 ± 0.12
34.2	1.02 ± 0.11
42.4	0.81 ± 0.09
48.7	0.47 ± 0.05

Table 1: Orientation-dependent interface stiffness. Measured interface stiffness ($\gamma+\gamma q''$) for several crystal orientations α. α enotes the angle between the normal of the crystal-fluid interface, and a nearest-neighbor vector in the hcp plane.

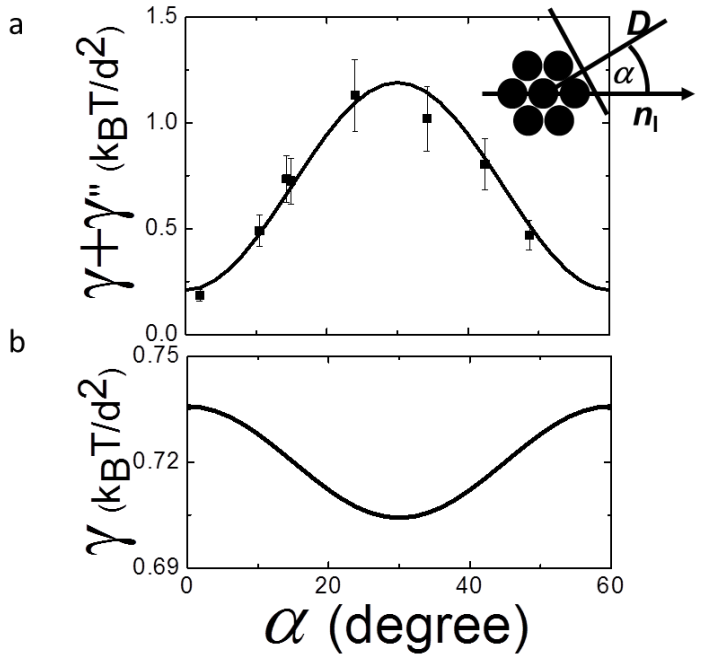

Figure 4.8: Anisotropy of interfacial stiffness and interfacial tension. Interfacial stiffness (a) and interface tension (b) as a function of crystal orientation. Inset: Schematic illustrating the angle α between the interface normal, n_l , and a crystal lattice direction, D.

simulations predict an anisotropy of ~0.4% within the hcp plane for hard sphere fcc crystals [29] and by using the planes (1120) and (1010) of the hexagonal lattice, we determine that simulations predict an anisotropy of ~0.2% for the hexagonal metal magnesium [30]. Our measured value is significantly larger than these predictions. Finally, we plot the resulting interfacial free energy according to equation (4.7) in Fig. 4.8b.

4.7 Discussion

It has been discussed that at high volume fraction, the method of particle insertion faces limitations because the available volume for insertion of a particle becomes very small [16, 31]. Other methods based on the free volume between particles (rather than the available volume) might then be better suited at such high density. For the crystal-fluid interface investigated here, however, we find that the method of particle insertion still provides a good approach to determine the free energy: the free energy density difference between crystal and fluid $\Delta f = 1.3\ k_B T$ is only about 13 % smaller than the expected value

for hard-sphere crystal-liquid equilibrium. Moreover, the surface tension $\gamma = 0.65\ k_B T / d^2$ is in good agreement with the value $\gamma = 0.70\ k_B T / d^2$ found using interface fluctuation method and with values found in simulations of hard- and slightly soft-spheres, which were between 0.50 and 0.8 $k_B T / d^2$. Further confirmation of the reliability of the free energy measurement can be obtained by comparing with the free volume methods suggested in the literature. These methods have been recently successfully applied to glasses at high density [32], being able to reproduce the correct equation of state, thereby lending credence to the method. A comparison of the different methods will be the subject of further investigation.

4.8 Conclusions

Our results establish a direct connection between the liquid short-range order and the interfacial free energy of crystal-liquid interfaces. Direct real-space imaging of particle configurations at the interface enabled us to follow changes in the short range order, and measure the corresponding interfacial free energy barrier directly. The measured interface tension agrees well with simulation values of hard and slightly soft spheres, while the anisotropy is surprisingly larger than that found in simulations. We consider this difference significant since it greatly exceeds the error margin of our measurements. Finally, while our measurements provide an immediate link between structure and free energy for the solid-liquid transition, similar relations applied to supercooled liquids and glasses should provide the important missing link between structure, free energy landscape, and structural relaxation of glasses.

Bibliography

[1] H. Senff, W. Richtering, "Temperature sensitive microgel suspensions: Colloidal phase behavior and rheology of soft spheres," *J. Chem. Phys. ,* vol. 111, p. 1705, 1999.

[2] J. D. Debord, S. Eustis, S. B. Debord, M.T. Lofye, L. A. Lyon, "Color-tunable colloidal crystal from soft hydrogel nanoparticles," *Adv. Mater.,* vol. 14, p. 658, 2002.

[3] J. Gao and Z. Hu, "Optical properties of N-Isopropylacrylamide microgel spheres in water," *Langmuir,* vol. 18, p. 1360, 2002.

[4] G. Romeo, A.Fernandez-Nieves, H. M. Wyss, D. Acierno, and D. A. Weitz, "Temperature-Controlled Transitions Between Glass, Liquid, and Gel States in Dense p-NIPA Suspensions," *Adv. Mater.,* vol. 22, p. 3441, 2010.

[5] R. H. Pelton, "Temperature-sensitive aqueous microgels," *Adv. Colloid Interface Sci.,* vol. 85, p. 1, 2000.

[6] F. Frank, "Supercooling of Liquids," *Proc. R. Soc. Lond. A,* vol. 215, p. 43, 1952.

[7] J. D. Bernal, "Geometry of the Structure of Monatomic Liquids," *Nature,* vol. 185, p. 68, 1960.

[8] J. Kepler, Joannes Plancus, Lincii Austria: Harmonices Mundi, Libri quinque, 1619.

[9] G. Tarjus, S. A. Kivelson, Z. Nussinov, and P. Viot, "The frustration-based approach of supercooled liquids and the glass transition: a review and critical assessment," *J. Phys.: Condens. Matter,* vol. 23, p. R1143, 2005.

[10] F. Spaepen, "A structural model for the solid-liquid interface in monatomic systems," *Acta Met.,* vol. 23, p. 729, 1975.

[11] H. Reichert, O. Klein, H. Dosch, M. Denk, V. Honkimäki, T. Lippmann, and G. Reiter, "Observation of five-fold local symmetry in liquid lead," *Nature,* vol. 408, p. 839, 2000.

[12] T. Schenk, D. Holland-Moritz, V. Simonet, R. Bellissent, and D. M. Herlach, "Icosahedral Short-Range Order in Deeply Undercooled Metallic Melts," *Phys. Rev. Lett.,* vol. 89, p. 075507, 2002.

[13] Y. K. C. S. W. D. K. a. M. R. S. H. Oh, "Ordered Liquid Aluminum at the Interface with Sapphire," *Science,* vol. 310, p. 661, 2005.

[14] A. M. Alsayed, M. F. Islam, J. Zhang, P. J. Collings, "Premelting at Defects Within Bulk Colloidal Crystals," *Science,* vol. 309, p. 1207, 2005.

[15] J. Mattsson, H. M. Wyss, A. Fernandez-Nieves, K. Miyazaki, Z. B. Hu, D. R. Reichman, D. A. Weitz, "Soft colloids make strong glasses," *Nature,* vol. 462, p. 83, 2009.

[16] R. P. A. Dullens, D. G. A. L. Aarts and W. K. Kegel, "Direct measurement of the free energy by optical microscopy," *Proc. Nat. Acad. Sci.,* vol. 103, p. 529, 2006.

[17] J. J. Hoyt, M. Asta and A. Karma, "Method for Computing the Anisotropy of the Solid-Liquid Interfacial Free Energy," *Phys. Rev. Lett.,* vol. 86, p. 5530, 2001.

[18] K. Lorincz and P. Schall, "Visualization of displacement fields in a sheared granular system," *Soft Matter,* vol. 6, p. 3044, 2010.

[19] J. Hernandez-Guzman and E. Weeks, "The equilibrium intrinsic crystal–liquid interface of colloids," *Proc. Nat. Acad. Sci.,* vol. 106, p. 15198, 2009.

[20] David A. Sessoms, I. Bischofberger, L. Cipelletti and V. Trappe, "Multiple dynamic regimes in concentrated microgel systems," *Phil. Trans. R. Soc. A,* vol. 367, p. 5013, 2009.

[21] S. M. Hashmi and E. R. Dufresne, "Mechanical properties of individual microgel particles through the deswelling transition," *Soft Matter,* vol. 5, p. 3682, 2009.

[22] P. N. Pusey and W. van Megen, "Phase behaviour of concentrated suspensions of nearly hard colloidal spheres," *Nature,* vol. 320, p. 340, 1986.

[23] M. Dijkstra, R. van Roij, and R. Evans, "Multiple dynamic regimes in concentrated microgel systems," *Phys. Rev. E,* vol. 59, p. 5744, 1999.

[24] J. Gibbs, The Scientific Papers of J. Willard Gibbs, New York: Dover, 1961.

[25] R. L. Davidchack, "Crystal Structure and Interaction Dependence of the Crystal-Melt Interfacial Free Energy," *Phys. Rev. Lett.,* vol. 94, p. 086102, 2005.

[26] S. L. a. R. T. R.E. Napolitano, "Experimental Measurement of Anisotropy in Crystal-Melt Interfacial Energy," *Interface Science,* vol. 10, p. 217, 2002.

[27] M. P. A. Fisher, D. S. Fisher, and J. D. Weeks, "Agreement of Capillary-Wave Theory with Exact Results for the Interface Profile of the Two-Dimensional Ising Model," *Phys. Rev. Lett.,* vol. 48, p. 368, 1982.

[28] R. L. Davidchack and B. B. Laird , "Direct Calculation of the Hard-Sphere Crystal /Melt Interfacial Free Energy," *Phys. Rev. Lett.,* vol. 85, p. 4751, 2000.

[29] R. L. Davidchack, J. R. Morris, and . B. Laird, "The anisotropic hard-sphere crystal-melt interfacial free energy from fluctuations," *J. Chem. Phys.,* vol. 125, p. 094710, 2006.

[30] D. Y. Sun, M. I. Mendelev, C. A. Becker, K. Kudin, T. Haxhimali, M. Asta, J. J. Hoyt, A. Karma, and D. J. Srolovitz, "Crystal-melt interfacial free energies in hcp metals: A molecular dynamics study of Mg," *Phys. Rev. B,* vol. 73, p. 024116, 2006.

[31] T. Aste, and A. Coniglio, "Cell theory for liquid solids and glasses: From local packing configurations to global complex behaviors," *Europhysics letters,* vol. 67, p. 165, 2004.

[32] R. Zargar,B. Nienhuis, P. Schall, and D. Bonn, "Direct measurement of the free energy of aging hard-sphere colloidal glasses," *Nature,* p. Submitted, 2012.

Chapter 5

Colloidal phase transitions induced by critical Casimir forces

The critical Casimir effect is a thermodynamic analogue of the well-known quantum mechanical Casimir effect. It acts between two surfaces immersed in a critical binary liquid mixture, and results from the confinement of concentration fluctuations of the liquid. Unlike the quantum mechanical effect, the magnitude and range of this attraction can be adjusted with temperature via the solvent correlation length, thus offering new opportunities for the assembly of nano and micron-scale structures. In this chapter, we demonstrate the active assembly control of equilibrium phases using critical Casimir forces. We guide colloidal particles into analogues of molecular liquid and solid phases via exquisite control over the particle interactions. We measure the critical Casimir pair potential of the particles directly by following density fluctuations in the colloidal gas. This allows us to elucidate the applicability of continuum models to the colloidal assembly process. We apply the Van der Waals model of molecular liquefaction to show that the colloidal gas-liquid condensation is accurately described by the Van der Waals theory, even on the scale of a few particles. We then use the experimentally measured particle pair potentials as input to Monte Carlo simulations to map out the entire phase diagram of

colloids interacting via critical Casimir forces. The calculated phase diagram agrees well with measurements of the experimental system, indicating that many body effects are limited. This phase diagram is qualitatively similar to those of molecular system. These results open up new possibilities in the active assembly of micro and nanostructures.

5.1 Introduction

The critical Casimir effect provides an interesting analogue of the quantum mechanical Casimir effect [1-4]. Close to the critical point of a binary liquid, concentration fluctuations become long-range, and the confinement of these long-range fluctuations between two surfaces gives rise to critical Casimir interactions. This offers new opportunities to achieve active control over the assembly of colloidal particles [5-8]. At close distance, solvent fluctuations confined between the particle surfaces lead to an effective attraction that adjusts with temperature on a molecular time scale. Because the correlation length depends on temperature, temperature provides a unique control parameter to control the range and strength of this interaction [1]. The advantage of this effect is its universality: as other critical phenomena, the scaling functions depend only on the symmetries of the system and are independent of material properties, allowing similar interaction control for a wide range of colloidal particles [9]. Such assembly control would have important applications for the design of structures at the micrometer and nanometer scale. In principle, by tuning critical Casimir interactions with temperature, analogues of molecular liquid and solid phases should be directly observable, and such direct control would offer new opportunities to actively guide the assembly of particles into nanostructures.

In this chapter, we demonstrate the direct control of equilibrium phase transitions with critical Casimir forces. Through exquisite control of the particle pair potential with temperature, we assemble colloidal particles into phases that are analogues of molecular liquid and solid phases, and we visualize these phases in three dimensions and on the single particle level. The direct imaging allows for direct measurement of the critical Casimir pair potential, and we elucidate the relation between critical Casimir attraction and gas-liquid condensation, a crucial step in the equilibrium assembly process. Gas-liquid condensation reflects the competition between the energy cost for compression of the particles against their entropic pressure, and the energy gain from the condensation of the

attractive particles. At some critical attraction, the energy released by condensation exceeds the energy needed for compression, and the system can lower its free energy by condensation into the liquid phase, thereby reducing the pressure of the remaining gas. As the attraction increases, an increasing portion of the gas condenses.

We measure important parameters of the condensation process: equilibrium densities of liquid and gas phases, and relative amount of gas and liquid. These microscopic observations provide a unique opportunity to test the applicability of mean field models of liquefaction. We find that the widely used Van der Waals model of molecular liquefaction also describes the particle condensation in our colloidal system remarkably well, even on the scale of a few particles, indicating that this mean-field model applies also to describe the condensation of nanoparticles in the formation of nanostructures.

We also combine the experimentally measured potential and Monte Carlo simulation to investigate phase equilibria due to critical Casimir forces. We locate colloidal gas, liquid and solid phases as a function of temperature and colloidal volume fraction. The resulting colloidal phase diagram agrees well with experiment, indicating that many body interactions play a secondary role and that pair potentials describe the experimental system well. The phase diagram has the characteristic topology of the molecular systems similar to that obtained with the Lennard-Jones potential, but occurs over a very narrow temperature range due to the strong temperature-dependence of the critical Casimir interactions.

5.2 Gas-liquid transition in the van der Waals model

In 1873, to describe attractive molecules of finite size, Johannes Diderik van der Waals modified the ideal gas equation of state $pV=Nk_BT$ that relates the pressure p, volume V and temperature T to [10, 11, 12]

$$\left(V - Nb\right)\left(P + \frac{N^2 a}{V^2}\right) = Nk_B T \qquad (5.1)$$

The attraction between molecules reduces the pressure by N^2a/V^2, where a accounts for the attractive potential of a particle due to all other particles. The finite molecule size reduces the volume accessible to the molecules by Nb, where b indicates the volume around a

particle which is inaccessible all other particles. If the number of molecules is fixed, molecular gases are condensed to liquid either by compression or by lowering the temperature, and by measuring P, V and T, the parameters a and b can be determined. An example of van der Waals isotherms is sketched in Fig. 5.1a. At high temperature, the isotherms show a pure gas phase. While at low temperature, the double-loop of the isotherms indicates the characteristic gas – liquid coexistence: at equal pressure, a low density phase and high density phase coexist. By rewriting Eq. 5.1 to

$$PV^3 - (bP + RT)V^2 + aV - ba = 0, \qquad (5.2)$$

we see that the pressure is a cubic polynomial in V: There is a region in which the polynomial has three real roots. As we increase T these roots move closer together, and merge at the critical point (point C in Fig.5.1a) when $T = T_c$, the critical temperature. At the critical point the gas and the liquid have equal density and specific entropy and the equation of state must be of the form

$$(V - V_c)^3 = 0 \qquad (5.3)$$

where V_c is the critical volume. Combining Eq. 5.2 and Eq. 5.3 we obtain the critical pressure P_c, the critical volume V_c and the critical temperature T_c as

$$RT_c = \frac{8a}{27b} \qquad (5.4)$$

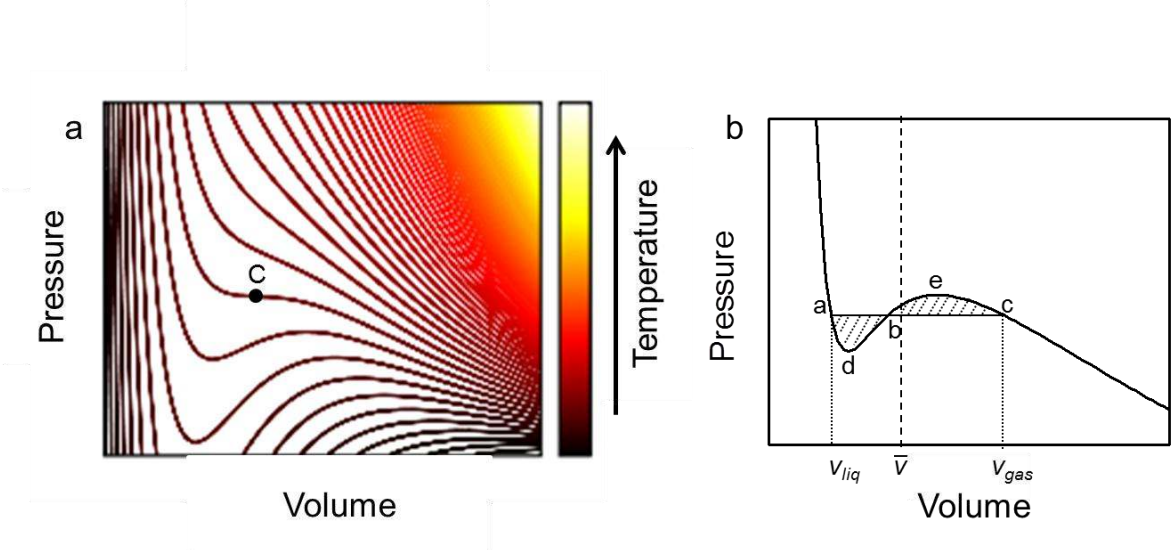

Figure 5.1: (a) van der Waals isotherms; at high temperature, the isotherms show a pure gas phase. At low temperature, the double-loop of the isotherms indicates the characteristic gas – liquid coexistence. The critical point is at C. (b) Maxwell equal area rule; two hatched regions are equal. Gas and liquid coexist at specific volumes v_{gas} and v_{liq}, respectively. $\bar{v}$ is an average specific volume of the system.

$$P_c = \frac{a}{27b^2} \tag{5.5}$$

$$V_c = 3b \tag{5.6}$$

To understand the gas-liquid condensation in more detail, let us consider a single isotherm containing a double-loop, as shown in Fig 5.1b. Along the isotherm, there is a portion (from *e* to *d*) where a compression gives rise to decreasing pressure, which indicates a physically unstable situation. The van der Waals equation fails to describe real substance in this region because the equation always assumes the fluid to be uniform, while between *a* and *c* on the isotherm, the stable state of the system is a coexistence of low density gas and a denser liquid phase. Thus, in 1875 James Clerk Maxwell replaced the isotherm between *a* and *c* by a horizontal tie line positioned so that the areas of the two hatched regions are equal. He argued that the work done on the system in going from *c* to *b* should equal work released on going from *a* to *b*. The flat line portion of the isotherm now corresponds to gas-liquid equilibrium [11, 13]. This tie line intersects the isotherm at v_{liq} and v_{gas}, the specific volumes of coexisting liquid and gas phases, which bound the gas-liquid coexistence regime.

The model predicts that a system with an average specific volume $\bar{v}$ inside the coexistence regime will separate into phases with specific volumes v_{liq} and v_{gas}, and with relative fraction

$$f_{liq} = \frac{v_{gas} - \bar{v}}{v_{gas} - v_{liq}} \tag{5.7}$$

$$f_{gas} = \frac{\bar{v} - v_{liq}}{v_{gas} - v_{liq}} \tag{5.8}$$

The Van der Waals equation provides a universal model for molecular gas-liquid condensation. However, most experimental confirmation comes from macroscopic measurement of pressure and volume; the parameters *a* and *b* are then fit parameters to the measured isotherms. The direct observation of colloidal gas-liquid transition presented in this chapter allows us to determine values of *a* and *b* from microscopic measurement. The parameters *a* and *b* are directly related to the attraction and microscopic volume of the particles as [10]

$$a = -2\pi \int_{r_1}^{\infty} U(r) r^2 dr \tag{5.9}$$

$$b = \frac{1}{2}V_{excl} = \frac{4}{6}\pi(2r_0)^3 \qquad (5.10)$$

where r_0 is particle radius, $U(r)$ is the particle pair potential and the lower limit of the integration r_1 is defined as the position where potential becomes negative.

5.3 Observation of colloidal phase transitions induced by critical Casimir forces.

We use colloidal pNipam particles suspended in the binary mixture of 3-mp and water (chapter 2.3). Sufficiently far below T_{cx} = 52.2 °C, the phase separation temperature of the binary solvent, the particles are uniformly suspended and form a dilute gas phase (Fig. 5.2a). At ΔT = 0.3°C below T_{cx}, the particles condense and form spherical aggregates that

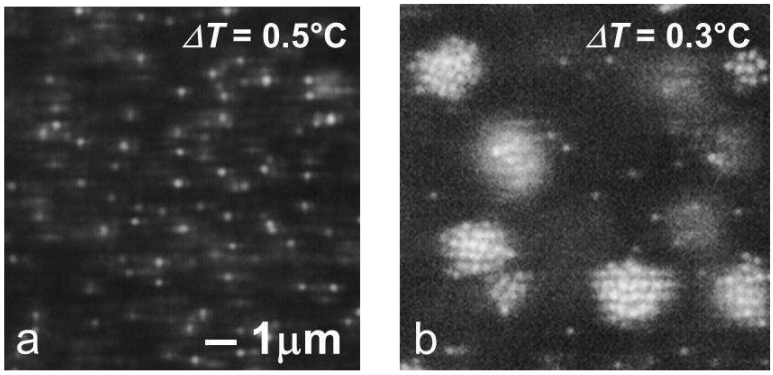

Figure 5.2: Confocal microscope images of colloidal gas-liquid transitions induced by critical Casimir forces: colloidal gas (a), and gas - liquid coexistence (b).

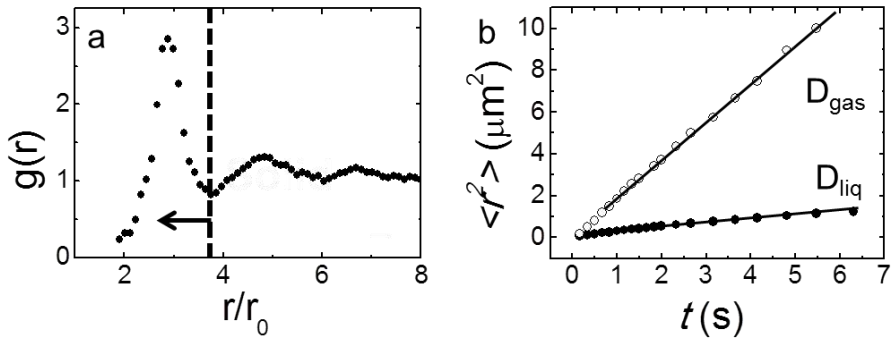

Figure 5.3: (a) Pair correlation function of colloidal particles in aggregates, the dashed line indicates the nearest-neighbor separation. (b) Mean-square displacement of particles in the dilute phase (circles) and in the aggregates (dots). The linear fits to the data yields diffusion coefficients, D_{gas} and D_{lid} that differs by a factor of 10.

coexist with a low-density colloidal gas (Fig. 5.2b). Within the aggregates, particles show the characteristic short-range order of a liquid as shown by the pair correlation function in Fig. 5.3a. We further confirm the liquid nature of the aggregates by tracking the motion of the particles, and comparing their mean-square displacement with that of the particles in the dilute gas in Fig. 5.3b. The mean square displacement grows linearly with time, similar to that of the motion of molecules in liquids. Moreover, it is factor of 10 slower than that of the gas particles, indicating the confinement of the particles in the dense liquid environment. When we raise the temperature further to $\Delta T = 0.2\,°\mathrm{C}$, the particles inside the aggregates form an ordered face-centered cubic lattice (Fig. 5.4): the colloidal liquid has frozen into a crystal. These observations appear as analogues of gas-liquid and liquid-solid transitions, driven by critical Casimir interactions. Because of the exquisite temperature dependence of critical Casimir interactions, these phase transitions occur with only small changes in temperature, and they are reversible: the crystals melt, and the liquid drops evaporate when the temperature is lowered below the characteristic thresholds. Such reversible control offers new opportunities for guiding the growth of perfect structures from colloidal building blocks [14]. The exquisite temperature dependence and reversibility allows precise control over the growth and annealing of perfect equilibrium structures, in analogy to the growth of atomic materials.

To elucidate the gas-liquid phase coexistence, we show three-dimensional reconstructions in Fig. 5.5. These reconstructions correspond to the confocal microscope images in Fig. 5.2. Red spheres indicate particles with more than 4 neighbors and small blue spheres

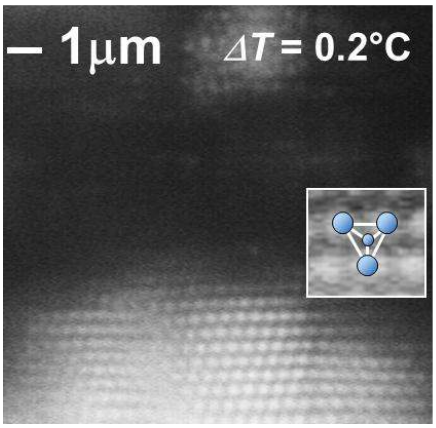

Figure 5.4: Confocal microscope image of colloidal crystal. Inset illustrates the relation between the imaged particle configuration and the structural motif of the face-centered cubic lattice.

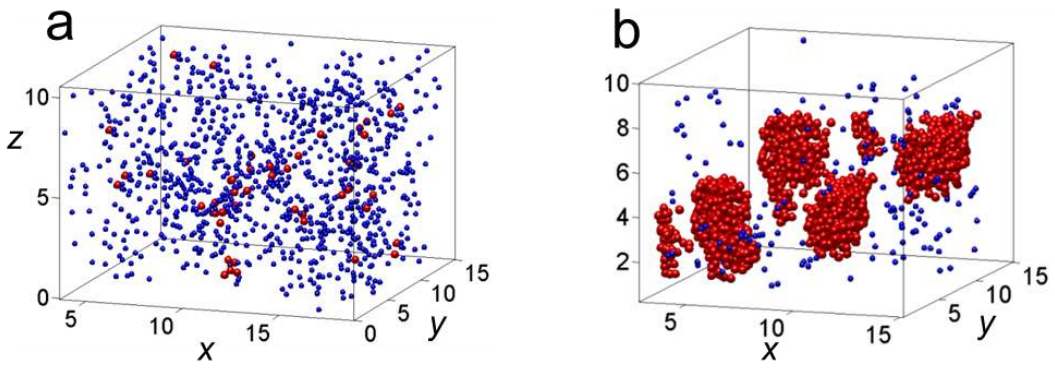

Figure 5.5: Three-dimensional reconstructions of gas and liquid correspond to the confocal images (Fig. 5.2). Red and blue spheres indicate particles with a large and small number of nearest neighbors, respectively. Red particles demarcate density fluctuations in the colloidal gas (a) and colloidal liquid aggregates coexisting with the colloidal gas (b).

indicate particles with 4 or less neighbors. Interestingly, at ΔT=0.5°C, small clusters of red particles appear and disappear, indicating spontaneous fluctuations in the density of the colloidal gas (Fig.5.5a). These density fluctuations become more pronounced as the temperature approaches T_{cx}. Then, at ΔT=0.3°C, after 10 min, red spheres form stable connected clusters (Fig. 5.5b), indicating stable liquid nuclei that grow to become large drops. To determine gas and liquid equilibrium densities, after 30 min, we measure the density of particles in the liquid and gas phases from the number of red and blue particles per volume, and obtain ρ_{liq}=3.0μm^{-3} and ρ_{gas}=0.1μm^{-3}, respectively.

5.4 Direct measurement of particle pair potential

We elucidate the mechanism that drives the condensation of particles by measuring the particle pair potential directly from the density fluctuations in the gas. The potential of mean force, U_{mf}, is related to the pair correlation function $g(r)$ which indicates the probability of finding two particles separated by r as [15]

$$g(r) \sim exp[-U_{mf}(r) / k_B T] \qquad (5.11)$$

We acquire 3000 images of particle configurations of the colloidal gas to determine the average pair correlation function at different temperatures, which we show in Fig. 5.6a. An

increasing peak arises at $r \sim 2.7 r_0$, indicating increasing particle attraction as the temperature approaches T_c. For dilute suspensions, $U_{mf} \approx U$, and the pair potential is obtained directly from the measurement of $g(r)$ as

$$U(r) / k_B T = -\ln g(r) \qquad (5.12)$$

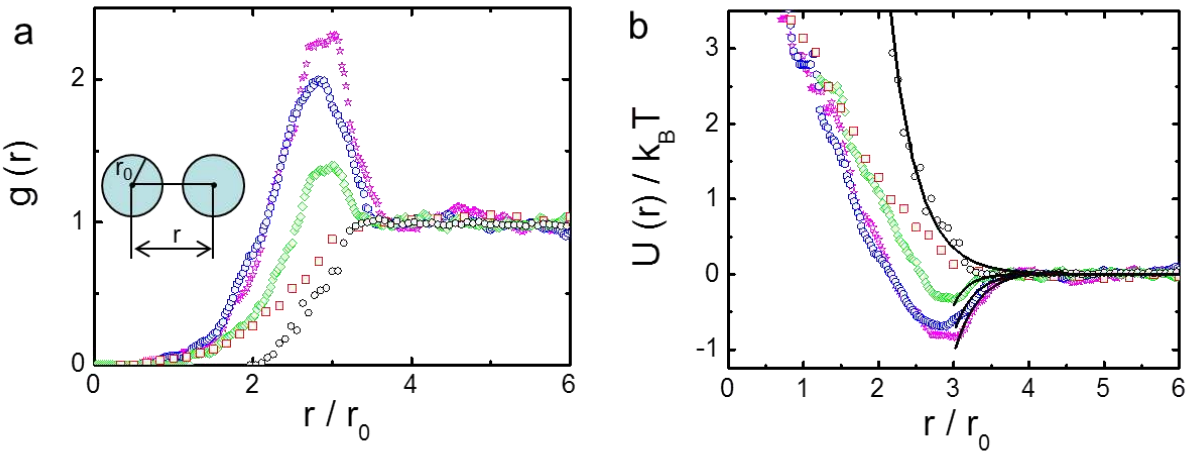

Figure 5.6: Particle pair correlation function (a) and corresponding particle pair potential (b) measured at different temperatures. The symbols indicate room temperature (black circles), ΔT=0.5 °C (red squares), 0.4 °C (green rhombi), 0.35 °C (blue hexagons) and 0.30 °C (magenta stars). The solid black line in (b) indicates the best fit with a screened electrostatic potential.

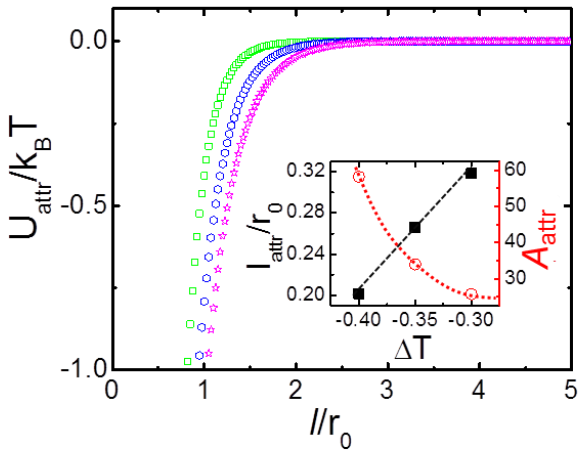

Figure 5.7: Attractive critical Casimir potentials extracted from the potential curves in (Fig. 5.6). Inset: range l_{attr} (black filled square) and amplitude A_{attr} (red open circle) of the critical Casimir potential as a function of ΔT. Dashed lines are guides to the eye.

The resulting pair potentials at different temperatures are shown in Fig. 5.6b. An attractive minimum emerges as the temperature approaches T_{cx}. This minimum reflects the competition between the critical Casimir attraction U_{attr}, and the screened electrostatic repulsion U_{rep} of the charged particles. We consider the total pair potential as [7]

$$U = U_{rep} + U_{attr} \tag{5.13}$$

where the screened electrostatic potential associated with the charged particles is described by [10]

$$U_{rep}(l) \approx A_{rep} \exp(-l / l_{rep}) \tag{5.14}$$

where $A_{rep} \sim 2\pi r_0 k_B T / l_{rep}$ is the amplitude, l_{rep} is the Debye screening length and $l = r - 2r_0$ is the distance between particle surfaces. The attractive critical Casimir potential can be approximated by [7]

$$U_{attr}(l) \approx -A_{attr} \exp(-l / l_{attr}). \tag{5.15}$$

Here $A_{attr} \sim 2\pi r_0 k_B T / l_{attr}$ and l_{attr} are the amplitude and the range of the critical Casimir attraction, respectively. We determine A_{rep} and l_{rep} from the potential at room temperature, where critical Casimir interactions are negligible. Excellent agreement with the data is obtained for $A_{rep} = 4.3\, k_B T$ and $l_{rep} = 0.36\, r_0$ (black circles and solid line in Fig. 5.6a). The values of A_{attr} and l_{attr} are then determined from the best fit of U to the measured potentials; these parameters are shown as a function of temperature in Fig. 5.7, inset. The data indicates that l_{attr} grows linearly with temperature, while the amplitude $A_{attr} \sim 1/l_{attr}$, as expected for the critical Casimir force between two spheres [7]. We use these parameters to determine the critical Casimir component, U_{attr}, of the pair potential, which we plot in Fig. 5.7, main panel.

5. 5 Experimental study of gas-liquid coexistence using the van der Waals model

The precision of these pair potential measurements allows us to make direct comparison with continuum models. We do this by applying the van der Waals equation of state to our attractive colloidal system. In contrast to molecular gases where values of a and b can only be inferred from macroscopic measurements, for our colloidal system, we can

determine the parameters a and b directly from the measured particle pair potential and particle size. Furthermore, while for molecular gases, the value of a is temperature-independent, and the only change with temperature occurs in the thermal energy, k_BT, for our colloidal system, temperature changes directly the value of a via the critical Casimir interactions. We determine values of a by numerical integration of the measured pair potentials using Eq. 5.9 and b from the measured particle radius using Eq. 5.10. The results are listed in table 1.We plot the resultant P as a function of V/Nb in Fig. 5.8. The values of a result in four isotherms; red and green curves show isotherms characteristic of a gas, while blue and pink curves show the double-loop characteristic of gas-liquid coexistence.

To test the van der Waals model, we determine the average volume per particle from the volume fraction using $\bar{v} = b/4\phi$, and indicate the resulting value $\bar{v} = 12.5b$ with a vertical dashed line. This line falls within the coexistence regime of only the pink isotherm, indicating that gas-liquid coexistence should occur only for $\Delta T = 0.30^{o}$C, in agreement with our direct observation (Fig. 5.2). Further confirmation of the model comes from comparison of the measured and predicted values of v_{liq} and v_{gas}. We determine the specific volumes of gas and liquid particles from the measured volume fractions ϕ_{liq}=0.25 and ϕ_{gas}=0.005 and obtain v_{liq}/b=1 and v_{gas}/b=50, in good agreement with the predicted values v_{liq}/b=1.25 and v_{gas}/b=43 determined from Fig. 5.8.

Furthermore, the relative amount of liquid and gas is f_{liq}=0.69 and f_{gas}=0.31, again in very good agreement with the values f_{liq}=0.72 and f_{gas}=0.28 obtained using Eq. 5.7 and Eq. 5.8. These results indicate that the van der Waals model provides a quantitatively accurate description of the colloidal gas-liquid equilibrium.

T (^{0}C)	ΔT (°C)	a (bk_BT)
51.70	0.5	0
51.80	0.4	1.28
51.85	0.35	3.67
51.90	0.3	5.25

Table 1: Temperature-dependent Van der Waals coefficient

Values of the Van der Waals coefficient, a, determined for several temperatures by integration of the measured particle pair potential (see Fig. 5.8, inset).

Molecular gas-liquid condensation typically entails measurement of the equilibrium vapor pressure, P_{eq}(T). For our colloidal system, this pressure is small and difficult to measure. However, we can estimate P_{eq} from the intersection of the horizontal tie line with the *y*-axis. From Fig. 5.9, we find $P_{eq} = 0.025(k_B T/b)$ yielding an equilibrium vapor pressure of $2 \cdot 10^{-4}$ Pa, 10^9 times smaller than typical vapor pressures of molecular gases at room temperature, which are of the order of ~10^5 Pa, the atmospheric pressure. This difference reflects the 10^9 times lower colloidal particle density associated with the ~10^3 times larger colloidal particle diameter. Therefore, the gas-liquid transitions in the colloidal and molecular systems are comparable. Vertical dashed black line indicates the average volume per particle, $\bar{v}$. Inset: Enlarged section of the particle pair potential at ΔT=0.35 °C illustrates the determination of the Van der Waals parameter a by integration. The lower integration boundary, r_1, is indicated by a dotted line.

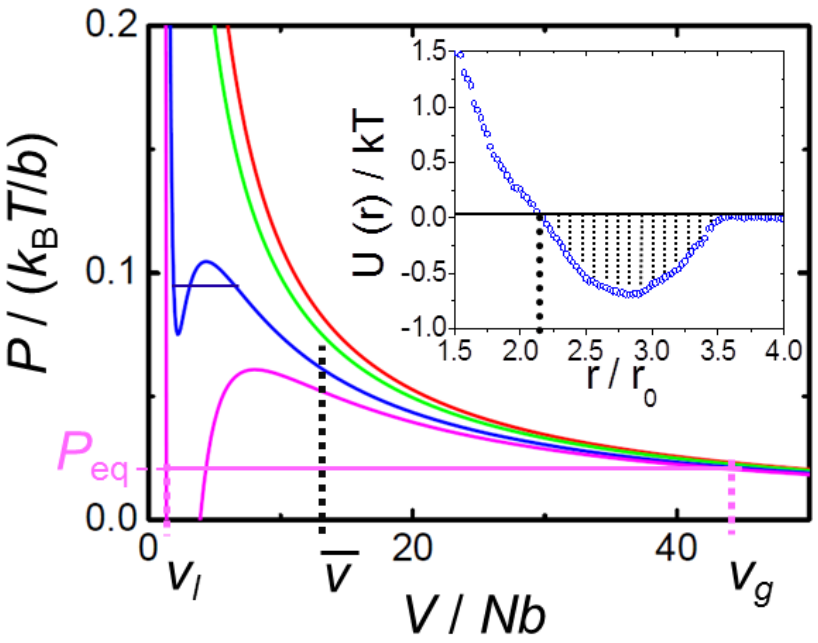

Figure 5.8: Van der Waals isotherms of the colloidal gas-liquid transition.

Van der Waals isotherms of the colloidal system for ΔT=0.5°C (red), 0.4°C (green), 0.35°C (blue), and 0.3°C (pink). A transition from a gas (green and red isotherms) to gas-liquid coexistence (blue and pink isotherms) is observed. Horizontal lines indicate tie lines, constructed following the Maxwell rule of equal chemical potential (equal areas included by the tie lines and isotherms). Intersections with the isotherms delineate the gas-liquid coexistence regimes.

5. 6 Monte Carlo simulation study of colloidal phase behavior induced by critical Casimir forces

In this section, we use the experimentally measured particle pair potentials and Monte Carlo (MC) simulations to fully examine the phase behavior of colloids in binary liquid solvents. This combination allows us to simulate phase equilibria due to critical Casimir forces. We locate colloidal gas, liquid and solid phases as a function of temperature and colloid volume fraction. In contrast to standard MC simulations where the temperature T only enters via the thermal energy, $\beta^{-1} = k_B T$, our simulations need to account explicitly for the temperature-dependent potential. The resulting colloidal phase diagram agrees well with experiment, indicating that many body interactions play a secondary role and that pair potentials describe the experimental system well. The phase diagram has the characteristic topology associated with molecular potentials like the Lennard-Jones potential, but occurs over a very narrow temperature range due to the strong temperature dependence of the critical Casimir interactions. These results highlight a novel way to control colloidal assembly by temperature-dependent critical Casimir interactions.

Simulating the phase behavior of the critical Casimir colloidal system requires a computationally efficient model. While in principle it is possible to compute the phase behavior from the ternary system of colloids in the liquid mixture, in practice this is prohibited by the large differences in length scales between the solvent molecules and the colloidal particles. We therefore model the colloidal system as particles interacting with effective potentials which implicitly account for solvent effects. We thereby assume that many-body effects are negligible and that interactions are well-described by pair potentials; this choice is validated by the close agreement between the simulated phase diagram and our experimental observations.

As discussed in section 5.4, we consider the measured potential to consist of a screened electrostatic repulsion $U_{\mathrm{rep}}(r)$ and a critical Casimir attraction $U_{\mathrm{attr}}(r;T)$. Assuming the critical Casimir attraction to be negligible at room temperature, and $Urep(r)$ to be independent of temperature allows us to determine A_{rep}, l_{rep}, A_{attr}, and l_{attr} directly from $U(r)$ according to equations (5.13)-(5.15). The results of those parameters were shown in Fig. 5.7, inset. Using those parameters we reproduce total pair potentials and overlay them onto the experimental data in Fig. 5.9. The observed difference between the reproduced and the measured potentials at short interparticle distances arises because the pNipam

particles are soft and thus easily compressed below their diameter at infinite dilution (note that the potentials shown in Fig.5.9 are still finite at r < 2r0), and the chosen potential form does not account for this effect. We show in the following that this apparent shortcoming of the chosen potential, however, introduces only a small error in the calculated phase diagram:

We confirm this by calculating the normalized second virial coefficients B_2 for both types of potentials. The second virial coefficient is a rough estimator of the phase behavior that should arise from a given potential [16]: a B_2 that is positive correlates with net repulsion between the particles, indicating that a phase transition should not occur; a strongly negative B_2 indicates the opposite. A B_2 that is close to zero indicates little net attraction or repulsion between the particles, so a phase transition is not expected. It follows that if the experimental and reproduced potentials at the same temperature lead to second virial coefficients of the same sign and comparable magnitude, the phase diagrams resulting from those potentials are expected to have the same topology and show only quantitative differences. We calculate B_2 according to [17]:

$$B_2 = -\frac{2\pi}{B_{2,HS}}\int_0^\infty r^2\left[\exp\left(-\beta U(r)\right)-1\right]dr \qquad (5.16)$$

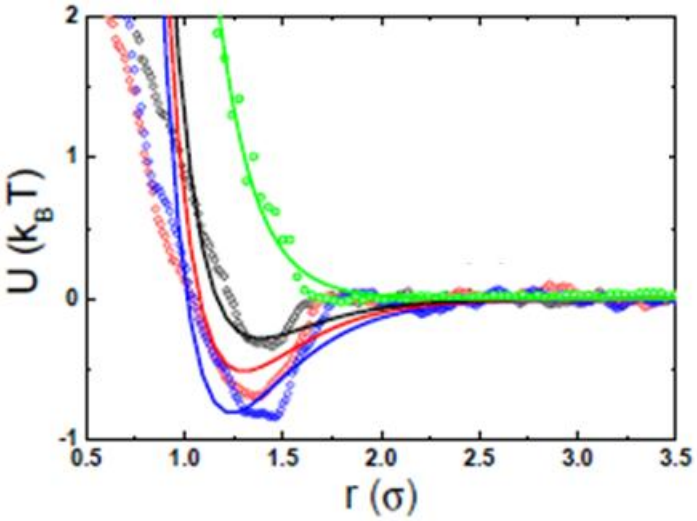

Figure 5.9: Experimental (circles) and fitted (lines) pair-potentials between colloids in a 3mp-water mixture at room temperature (green), ΔT = -0.4 °C (black), ΔT = -0.35 °C (red), and ΔT = -0.3 °C (blue). The green line effectively is the fitted electrostatic potential.

In this expression $B_{2,HS} = 2/3\sigma^3$ is the second virial coefficient for a system of hard spheres of diameter σ. For $0 < r \leq 1.5\ r_0$ the potential is too repulsive to be accurately measured in experiment. To integrate Eq.5.16 we thus used $U(r) = \infty$ for $0 < r \leq 1.5\ r_0$.

The upper integration boundary is set to $r = 7\ r_0$ because all potentials are approximately zero. The resulting normalized second virial coefficients are given in Table 2. At the lowest temperature $|\Delta T| = 0.4^oC$, for which potential was measured experimentally, the calculated B_2 coefficients for the fitted and experimental potentials are close to zero, indicating that phase transitions should not yet occur. This result is in line with our experimental observation: at this temperature, phase transitions do not occur yet. At the two highest temperatures for which the potentials were measured experimentally ($|\Delta T| = 0.35^oC$ and $|\Delta T| = 0.30^oC$), the B2 coefficients for both fitted and experimental potentials are negative, so we expect that the fitted potential will lead to the qualitatively correct phase behavior. Furthermore, at $|\Delta T| = 0.3^oC$, the B_2 corresponding to the experimental potential is almost identical to that for the fitted potential at $|\Delta T| = 0.35^oC$. These finding suggest that approximating the experimental potentials with the fitted ones will result in a calculated phase diagram with the correct topology, but shifted relative to the true one by no more than 0.05 ^oC.

Obtaining a complete phase diagram from simulations requires more closely-spaced potentials in a wider temperature range than is possible to measure experimentally. We therefore interpolate the critical Casimir potentials using a linear fit of the parameter lattr as a function of temperature and $A_{attr} \sim 1/l_{attr}$. Using this linear fit, we also extrapolate the critical Casimir potentials at lower and higher temperatures. We apply these potentials in Gibbs Ensemble MC simulations to investigate the gas-liquid transition of the colloidal system. For each temperature, we determine the associated pair potential $U(r;T)$ and compute the equilibrium gas and liquid volume fractions. The resulting gas and liquid volume fractions bounding the gas-liquid coexistence region are shown in Fig. 5.10. Close to T_{cx}, e.g. at $|\Delta T| = 0.3^oC$, the critical Casimir potential induces a separation into a dilute

	ΔT (°C)		
	0.4	0.35	0.30
Experimental	0.28	-1.0	-2.5
Fitted	-0.48	-2.4	-3.9

Table 2: B_2 coefficients for the experimental and fitted potentials at three different temperatures.

gas phase and a dense liquid phase with volume fraction around $\phi = 0.004$ and $\phi = 0.45$, respectively. As the temperature decreases, the critical Casimir potential becomes weaker, and the gas-liquid coexistence region shrinks, until near ΔT =0.336 oC, the binodal curve ends in a critical point (determined as described below) with a volume fraction $\phi = 0.136$. For temperatures $|\Delta T| \geq 0.3^{o}C$ the particles stay homogeneously suspended. Very similar behavior is observed in the experiments described in section 5.3. At $|\Delta T| = 0.35^{o}C$, the colloidal particles remain uniformly suspended, while at $|\Delta T| = 0.3^{o}C$ and $|\Delta T| = 0.25^{o}C$, phase separation into gas and liquid was observed. The volume fractions of gas and liquid measured by confocal microscopy are in reasonable agreement with the simulated phase diagram given the large uncertainty in the determination of ϕ and $|\Delta T|$ (see Fig. 5.10). Note that as our simulations are based on effective pair potentials from dilute solution, the observed agreement between experiment and simulation indicates that many body effects are limited, even at high colloid volume fractions.

We further investigated the occurrence of crystal-liquid equilibria. As the Gibbs ensemble is not easily applied to solid-liquid coexistence, we instead employ Kofke's Gibbs-Duhem integration technique [18]. Here the full coexistence curve is computed by numerically

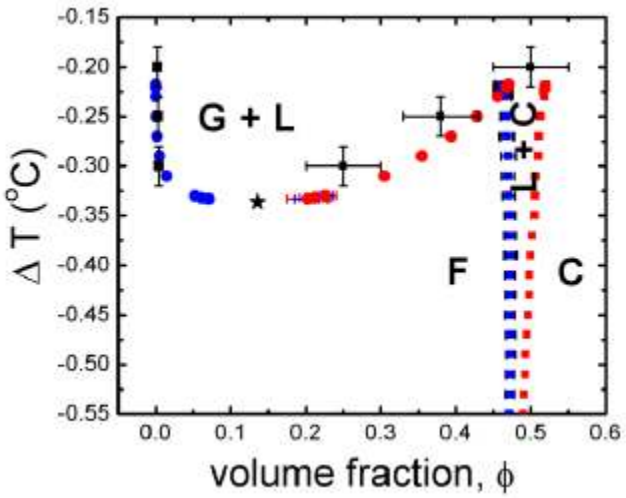

Figure 5.10: Colloidal phase diagram induced by the critical Casimir forces.

The circles denote the gas-liquid coexistence curve. Blue- and red circles represent the gas phase (G) and the liquid (L) phase, respectively. The black star indicates the gas-liquid critical point. The blue and red squares denote the fluid-crystal (F-C) coexistence curve. The black squares and error bars are experimental coexistence points of gas-liquid (ΔT = –0.3, –0.25 ^{o}C) and gas-crystal (ΔT = -0.20 ^{o}C).

integrating the Gibbs- Duhem equation (or equivalently, the Clausius-Clapeyron equation) starting from a known reference coexistence point. For our system, the relevant reference point is the hard sphere system coexistence at a pressure of $\beta P/\sigma^3 = 11.67$ [19] and volume fractions $\phi_l = 0.494$ and $\phi_s = 0.545$, for the liquid and the face-centered cubic (fcc) crystal phase, respectively. The resulting fluid-solid coexistence curve is shown in Fig. 5.10. This coexistence curve connects well with the gas-liquid phase boundary: the two curves intersect at the temperature $|\Delta T| = 0.22^oC$, the triple point, where the liquid-crystal coexistence pressure almost vanishes [20]. These observations are consistent with our experiments: at temperatures $|\Delta T|$ between 0.25 and 0.20 ^oC, face-centered cubic (fcc) crystals formed inside the liquid drops; at $|\Delta T| = 0.20^oC$, they consisted entirely of fcc crystals (see Fig. 5.4), exhibiting a volume fraction of ϕ ~ 0.5, in agreement with the simulations (see Fig. 5.10).

The phase diagram shown in Fig. 5.10 mirrors the well-known gas-liquid-solid phase diagram of Lennard-Jones systems [21, 22], lattice-based Ising models [23], and systems with square-well potentials [24, 25]. The diagram is inverted with respect to the known phase diagrams of Lennard-Jones systems, because βU becomes stronger as we approach the solvent phase separation from below, instead of βU becoming weaker with increasing temperature, as is the case in Lennard-Jones systems. Because for our system, the interparticle potential is explicitly strongly temperature dependent, the entire phase diagram extends only over a very small temperature range of ~ 0.3 ^oC.

5.7 Influence of the solvent composition

In this section, we investigate the influence of the solvent composition on the range and amplitude of particle pair potential. To do this, we increase the mass fraction of 3mp, in the water-3mp mixture, from 0.25 to 0.28 and use equal amount of H_2O and D_2O. The increase of 3mp lowers the solvent phase separation temperature to T_{cx}=39.5 °C. We measure the particle pair potential directly from the density fluctuations of the colloidal particles as described earlier. The resulting particle pair potential at different temperatures is shown in Fig. 5.11a. Similar to the system with 0.25 mass fraction of 3mp, the range and the amplitude of attraction increase when the temperature approaches the solvent phase separation temperature. We compare pair potentials of the two solvent

compositions, measured at the same ΔT. We see that the range of attraction increases as the 3mp fraction approaches the critical composition. These observations are in good agreement with earlier experimental results [1, 9]. We used this system to investigate colloidal phase behavior as before. We found that the system exhibits the gas-liquid coexistence at a larger temperature difference of ΔT = 0.40 ^{o}C to the critical temperature. These results suggest that as the range of attraction increases, the gas-liquid coexistence appears at lower attraction strength, as expected from the second virial coefficient. Therefore, solvent compositions closer to the critical point may be advantageous, since they allow investigation of colloidal phase behavior in a wider temperature-range.

Finally, we investigate the potential depth as a function of temperature by plotting potential depth as a function of ΔT in Fig. 5.11b. The results show that the potential depth increases strongly as the temperature approaches the solvent phase separation temperature. The data suggest an exponential relation between the potential depth and ΔT. This exponential dependence is in good agreement with results of Bechinger et al. for critical Casimir force between a single colloid and a planar surface [1, 9].

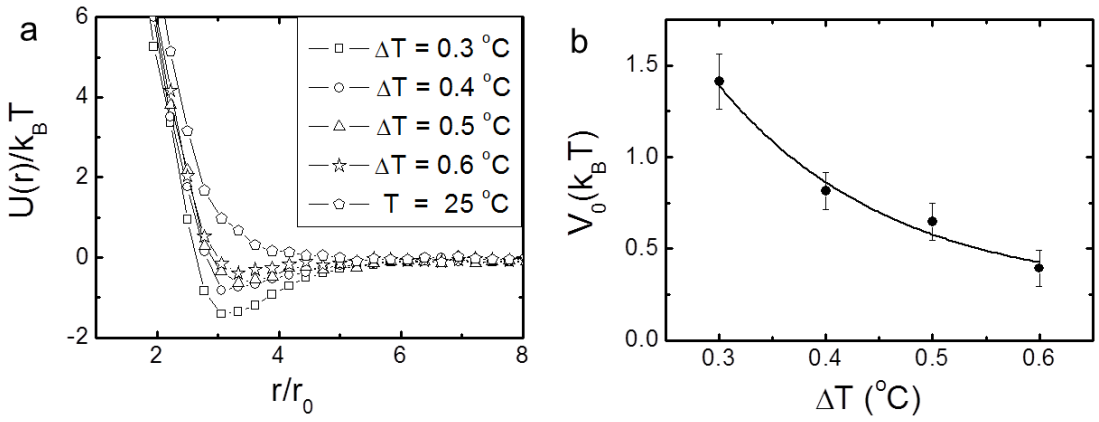

Figure 11: Critical Casimir attractions.

(a) Pair potentials at different temperatures of pNipam particles suspended in binary solvent consisting of 28 % 3mp. (b) Potential depth as a function of ΔT below the solvent separated temperature T_{cx}. The data points are the minima of the pair potentials in (a). Solid line indicates the best exponential fit to the data.

5.8 Conclusions

In this chapter, we have demonstrated the formation of equilibrium liquid and solid phases using critical Casimir forces. Using Monte Carlo simulations with experimentally determined pair particle potentials as input, we have completed the phase behavior numerically, and mapped out the corresponding phase diagram. This active and reversible control of colloidal gas-liquid and liquid-solid equilibria lays the groundwork for novel assembly techniques making use of critical Casimir forces by a unique procedure of precise temperature control. Because of the reversibility of the interactions, one can imagine using temperature gradient and zone melting techniques to grow perfect equilibrium structures, in analogy to atomic crystal growth. The presented close correspondence of the colloidal and the molecular gas-liquid transition suggests further studies of equilibrium and non-equilibrium phenomena using these colloidal systems as models with active potential control. The close agreement between the molecular Van der Waals theory and the colloidal phase separation that we observe on the scale of just a few particle diameters suggests that such mean field models may also be applied to describe the condensation of nano particles in the assembly of nanostructures. Moreover, the agreement between the simulation phase diagram and experimental data suggests that the critical Casimir interactions between colloids are sufficiently well described by two-body potentials. In contrast to other temperature-dependent colloid-colloid potentials, the critical Casimir effect allows temperature control of colloidal phases in a new, reversible and universal fashion. We foresee that more complex structures can be obtained by particle surface patterning to create anisotropic critical Casimir interactions. Together with the tunable solvent correlation length, such surface modification might allow mimicking “atomic orbitals” to assemble colloidal particles into structures similarly complex as those of molecules.

Bibliography

[1] C. Hertlein, L. Helden, A. Gambassi, S. Dietrich, C. Bechinger, "Direct measurement of critical Casimir forces," *Nature,* vol. 451, p. 172, 2008.

[2] Gennes, M. E. Fisher and P.-G. de, "Physique des Colloides," *C. R. Acad. Sci. Ser. B,* vol. 287, p. 207, 1978.

[3] M. Fukuto, Y.F. Yano, P. S. Pershan, "Critical Casimir Effect in Three-Dimensional Ising Systems: Measurements on Binary Wetting Films," *Phys. Rev. Let.,* vol. 94, p. 135702, 2005.

[4] S. Rafai, D. Bonn, J. Meunier, "Repulsive and attractive critical Casimir forces," *Physica A,* vol. 286, p. 31, 2007.

[5] D. Beysens and D. Esteve, "Adsorption Phenomena at the Surface of Silica Spheres in a Binary Liquid Mixture," *Phys. Rev. Let.,* vol. 54, p. 2123, 1985.

[6] D. Beysens and T. Narayanan, " Wetting-induced aggregation of colloids," *J. Stat. Phys,* vol. 95, p. 997, 1999.

[7] D. Bonn, J. Otwinowski, S. Sacanna, H. Guo, G. Wegdam and P. Schall, "Direct Observation of Colloidal Aggregation by Critical Casimir Forces," *Phys. Rev. Let.,* vol. 103, p. 156101, 2009.

[8] H. Guo, T. Narayanan, M. Sztuchi, P. Schall, and G. H. Wegdam,, "Reversible Phase Transition of Colloids in a Binary Liquid Solvent," *Phys. Rev. Let.,* vol. 100, p. 188303, 2008.

[9] A. Gambassi, A. Maciołek, C. Hertlein, U. Nellen, L. Helden, C. Bechinger, and S. Dietrich, "Critical Casimir effect in classical binary liquid mixtures," *Phys. Rev. E,* vol. 80, p. 061143, 2009.

[10] J. Israelachvili, Intermolecular & Surface Forces, San Diego: Academic Press, 1992.

[11] K. Huang, Introduction to statistical physics, Boca Raton: CRC press, 2010.

[12] J. V. d. Waals, Dissertation, University of Leiden , 1873.

[13] J. C. Maxwell, "The scientific papers of James Clerk Maxwell," *Dover,* vol. 424, p. 1965, 1890.

[14] Glotzer S.C. and Solomon M. J, "Anisotropy of building blocks and their assembly into complex structures," *Nature Materials,* vol. 6, p. 557, 2007.

[15] S. H. Behrens and D. G. Grier, "Pair interaction of charged colloidal spheres near a charged wall," *Phys. Rev. E,* vol. 64, p. 050401R, 2001.

[16] G. A. Vliegenthart and H. N. W. Lekkerkerker, "Predicting the gas–liquid critical point from the second virial coefficient," *J. Chem. Phys.,* vol. 112, p. 5364, 2000.

[17] M. E. Tuckerman, Statistical Mechanics: Theory and Molecular Simulation, Oxford University Press, 2011.

[18] D. A. Kofke, "Direct evaluation of phase coexistence by molecular simulation via integration along the saturation line," *J. Chem. Phys.,* vol. 61, p. 4149, 1993.

[19] U. Nellen, J. Dietrich. L. Helden, S. Chodankar, K. Nygard, J. Friso, C. Bechinger, "Salt-induced

changes of colloidal interactions in critical mixtures," *Soft matter,* vol. 7, p. 5360, 2011.

[20] J. Q. Broughton and X. P. Li, "Phase diagram of silicon by molecular dynamics," *Phys. Rev. B,,* vol. 35, p. 9120, 1987.

[21] B. Smit, P. Desmedt and D. Frenkel, "Computer simulations in the Gibbs ensemble," *Mol. Phys.,* vol. 68, p. 931, 1989.

[22] A. Z. Panagiotopoulos, "Molecular simulation of phase coexistence: Finite-size effects and determination of critical parameters for two- and three-dimensional Lennard-Jones fluids," *Int. J. Thermophys.,* vol. 15, p. 1057, 1994.

[23] K. K. Mon and K. Binder,, "Finite size effects for the simulation of phase coexistence in the Gibbs ensemble near the critical point," *J. Chem. Phys.,,* vol. 96, p. 6989, 1992.

[24] J. R. Recht and A. Z. Panagiotopoulos, "Finite-size effects and approach to criticality in Gibbs ensemble simulations," *Mol. Phys.,* vol. 80, p. 843, 1993.

[25] L. Vega, E. D. Miguel, L. F. Rull, G. Jackson, and I. A. McLure, "Phase equilibria and critical behavior of square-well fluids of variable width by Gibbs ensemble Monte Carlo simulation," *J. Chem. Phys.,* vol. 96, p. 2296, 1992.

Chapter 6

Visualizing colloidal liquid nucleation by critical Casimir forces

In the preceding chapter, we have investigated colloidal phase transitions induced by critical Casimir forces. We have shown that with precise temperature control of critical Casimir forces we achieved reversible control of colloidal gas-liquid and liquid-solid equilibria. In this chapter, we focus on the formation of the liquid phase and investigate liquid nucleation and growth with real and the reciprocal space techniques down to the single particle level. This allows us to obtain direct insight into the nucleation of liquids, which is difficult to study at the atomic scale. We directly visualize critical liquid nuclei and study their structure. We then measure the size-dependent surface tension and chemical potential directly from the distribution of droplet sizes. Using classical nucleation theory, we elucidate the relation between size-dependent surface tension, chemical potential, and thermal fluctuations that governs the nucleation of the liquid. Because of the similarly between the critical Casimir potential and molecular potentials, we argue that these observations allow insight into the nucleation of molecular liquids as well.

6.1 Introduction

Nucleation is the formation of a thermodynamically stable phase in a metastable phase, produced by a first order transition. The nucleation of a liquid from its saturated vapor phase provides an archetypical example of nucleation, and has been studied for nearly 100 years because of its importance to processes in the earth atmosphere, and many industrial applications. Nucleation reflects the competition between the energy cost ΔG_{surf} to create an interface between the liquid and vapor phases, and the energy gain ΔG_{bulk} from the condensation of particles into the thermodynamically stable phase [1-4]. The total nucleation energy reaches a maximum ΔG^* at a critical nucleus radius r^*, where both contributions balance. Nuclei are only stable and grow if their radius $r > r^*$. The maximum ΔG^* represents the energy barrier for liquid nucleation, and depends sensitively on the amount of supersaturation determining ΔG_{bulk} [5]. An important question concerns the relation between the liquid structure and the surface tension and chemical potential. The normal application of classical nucleation theory assumes the values of macroscopic liquid phases to apply at small scales; however, both ΔG_{surf} and ΔG_{bulk} depend on the liquid structure inside the nucleus that itself can depend on the nucleus size; direct imaging of atomic configurations in molecular liquids, however, is prohibitively, difficult. While macroscopic expansion and diffusion measurements allow determination of the average nucleation rate, the structure of critical nuclei and the interplay of size-dependent surface tension, chemical potential and thermal fluctuations are extremely difficult to observe directly in atomic systems.

In this chapter, we report the direct visualization of liquid nucleation in colloidal system induced by critical Casimir forces. The temperature-dependent critical Casimir force allows us to change directly the interaction energy U between the particles; this enables us to adjust the amount of supersaturation of the colloidal gas. Moreover, the direct imaging of the individual particles allows us investigate the structure of critical nuclei directly in three-dimensional (3D) space. These microscopic observations provide a unique opportunity to elucidate the relation between size-dependent nucleus structure and nucleation energies, and to test the applicability of nucleation theories.

6.2 Free energy barrier in classical nucleation theory

Nucleation of the liquid phase from a supersaturated vapor phase is an activated process that involves the formation of a critical nucleus of the thermodynamically stable liquid phase within the metastable vapor phase. The free energy of formation of the liquid nucleus is determined by the free energy gain due to condensation of the attraction particles and the free energy cost due to the creation of the gas-liquid interface. The classical nucleation theory (CNT) [1-4] uses these two terms to obtain an expression for the free energy difference between a homogenous bulk gas and a system containing a spherical liquid nucleus of radius R as

$$\Delta G = 4\pi R^2 \gamma - \frac{4\pi}{3} R^3 \Delta\mu \rho_l , \qquad (6.1)$$

where γ is the interfacial tension of gas-liquid interface, $\Delta\mu$ is the chemical potential difference between gas and liquid, and ρ_l is the number density of particles in the liquid. In Eq. 6.1, the first term is referred to as surface energy, ΔG_{surf}, and the second term is referred to as the bulk energy, ΔG_{bulk}. For small nuclei, ΔG_{surf} is larger than ΔG_{bulk}, and spontaneously formed nuclei are unstable and disappear. With increasing nucleus size, ΔG_{bulk} grows faster than ΔG_{surf}, until, at the critical nucleus size, the bulk energy dominates over the surface energy and spontaneously formed nuclei are stable and grow.

The critical radius is

$$R^* = \frac{2\gamma}{\rho_l \Delta\mu} , \qquad (6.2)$$

and the free energy cost to create the critical nucleus is

$$\Delta G^* = \frac{16\pi\gamma^3}{\rho_l^2 \Delta\mu} \qquad (6.3)$$

From the critical radius, and the particle density ρ_l, we determine that the number of particles in a critical nucleus is

$$n^* = \frac{32\pi}{3\rho_l^2}\left(\frac{\gamma}{\Delta\mu}\right)^3 \qquad (6.4)$$

In thermal equilibrium, the probability P_n for a particle to be in a cluster containing n particles is

$$P_n = \exp\left(\frac{-\Delta G_n}{k_B T}\right) \tag{6.5}$$

Therefore, in the nucleation stage, the occurrence of clusters of size n allows us to directly determine the free energy cost ΔG_n of formation of the liquid cluster. One of the most important predictions of classical nucleation theory is the prediction of nucleation rates. Such prediction needs accurate estimates of γ and $\Delta\mu$. Both quantities, however, depend on the structure of the liquid phase, which, for small nuclei of the order of a few particle diameters, might no longer be that of the bulk liquid phase. There has been much discussion about the size-dependence of the surface tension for small nuclei [5-7]. Our direct observation of nucleation allows us to image the 3D structure of critical nuclei as they form. Furthermore, from density fluctuations of the gas, we can directly determine the particle pair potential (see chapter 5). This allows us to elucidate the relation between the liquid structure, particle pair potential and coarse-grained quantities like surface tension and chemical potential.

6.3 Surface tension in Kirkwood and Buff theory

According to the thermodynamic definition, surface tension is the isothermal work of formation of unit area of interface. However, Kirkwood and Buff found that the mechanical definition of surface tension in terms of the stress transmitted across a strip of unit width offers the most direct approach to a molecular theory. Let's consider a system of coexisting gas and liquid, where the two phases are separated by a planar surface (Fig. 6.1a-b). The density of the gas and the liquid are ρ_g and ρ_l, respectively. In thermal equilibrium, the pressure in the bulk gas and liquid phases is constant and equal to P^0. In the interfacial region, pressure is a function of z. Let $P^t(z)$ be the normal pressure exerted by one element of volume of the fluid on a neighboring element across a plane parallel to the z-axis. Far away from the surface region,

$$P^t(z) = P^0; \tag{6.6}$$

whereas, within the surface region (Fig. 6.1c)

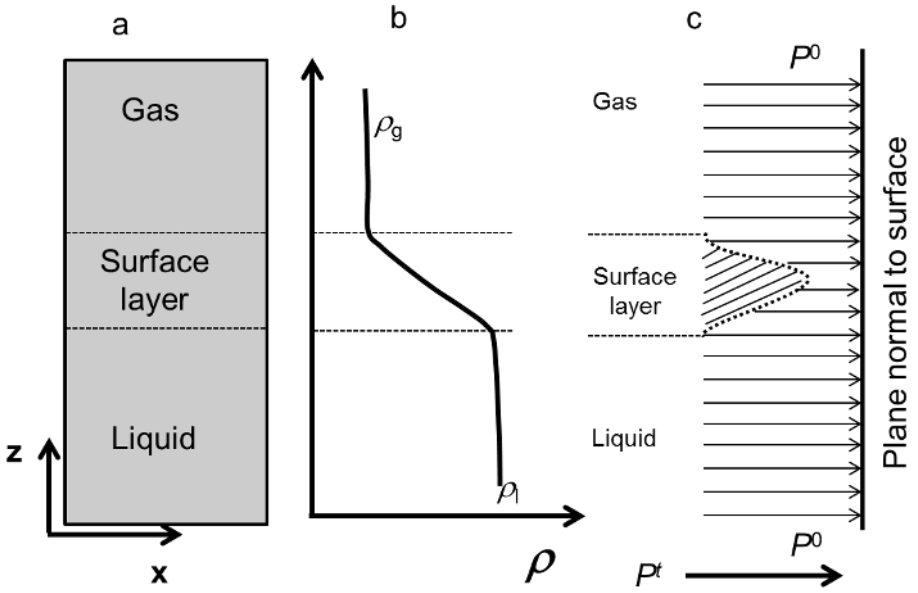

Figure 6.1: Representation of gas-liquid interface and its pressure deficit.

(a) Surface layer model. (b) Variation of density across the surface region; the density of the gas and the liquid are ρ_g and ρ_l, respectively. (c) Variation of the normal pressure, p^t, on the plane parallel to z-axis. The pressure deficit is indicated by the hatched region.

$$P^t(z) < P^0 \qquad (6.7)$$

The pressure deficit $\{P^0 - P^t(z)\}$ in the surface layer manifests itself macroscopically as a tension exerted by the molecules along the surface plane. The magnitude of this tension, per unit length, is the surface tension, and is given by [8]:

$$\gamma = \int_{-\infty}^{\infty}\{P^0 - P^t(z)\}dz \qquad (6.8)$$

This equation is quite general and rigorous. However, its application to real situations is difficult because the pressure $P^t(z)$ is not known. To avoid this difficulty, Kirkwood and Buff relate the pressure $P^t(z)$ to the kinetic and the potential energy as

$$P^t(z) = kT\rho(z) - \frac{1}{2}\int \frac{dU(r)}{dr} g(r) r dr, \qquad (6.9)$$

where k is Boltzmann's constant, $\rho(z)$ is the local density, $g(r)$ is the molecular pair distribution function, and $U(r)$ is the molecular pair potential.

Far away from the surface, $P^t(z)$ becomes equal to P^0, the equilibrium pressure in the system. Hence, we have

$$P^0 = kT\rho_g - \frac{1}{2}\int \frac{dU(r)}{dr} g_g(r) r dr, \qquad (6.10a)$$

$$= kT\rho_l - \frac{1}{2}\int \frac{dU(r)}{dr} g_l(r) r dr, \qquad (6.11b)$$

where $g_g(r)$ and $g_l(r)$ are the molecular pair distribution functions in the gas and in the liquid, respectively.

We can now employ (6.8) to evaluate γ. We have

$$\gamma = \int_0^\infty \{P^0 - P^t(z)\} dz + \int_{-\infty}^0 \{P^0 - P^t(z)\} dz \qquad (6.12)$$

Using equations (6.10a) and (6.10b) and assuming the gas is infinitely dilute and the liquid is homogenous right up to the dividing surface, the surface tension is simply determined as

$$\gamma = \frac{\pi\rho_l^2}{8}\int_0^\infty \frac{dU(r)}{dr} g_l(r) r^4 dr \qquad (6.13)$$

Since published in 1949, the Kirkwood-Buff theory has become the most general statistical mechanical theory which is applicable to all types of intermolecular interactions. In this thesis, we apply this theory to relate the surface tension of liquid clusters to the measured liquid density, particle pair distribution, and particle pair potential.

6.4 Observation of liquid nucleation and growth by dynamic light scattering

We use dynamic light scattering to obtain an overview over the liquid nucleation and growth process. This technique allows us to measure the average size of liquid droplets from fluctuations of the scattered intensity due to their diffusion (see chapter 2 and chapter 5 for more detail). We use a suspension of pNipam particles in a binary solvent of 3mp and water, with 3mp mass fraction of 28%. As discussed in the last chapter, this solvent composition offers a wide temperature range to investigate the colloidal gas-liquid transition. To obtain reproducible results, we follow a fixed temperature protocol; we first equilibrate the sample at a temperature 0.7°C below T_{cx} where critical Casimir forces are negligible, and hold it for 30 minutes to achieve a homogeneous particle suspension. We then increase the temperature towards T_{cx} and fix the temperature at $\Delta T = 0.3$°C, well inside the gas-liquid coexistence regime, to observe the nucleation and growth of the liquid phase.

Dynamic light scattering allows us to follow the growth of aggregates in time. The dynamic light scattering setup and technique is described in chapter 2. We record the scattering intensity at an angle of 90° to the incident beam. In order to follow the aggregate size in time, we evaluate the fluctuations of the scattered intensity after different waiting times, t_w. This allows us to determine the average aggregate radius at different stages of growth.

We show the reduced correlation function of the scattered intensity at different waiting times in Fig. 6.2a. All curves show a double-exponential decay $C_t(\tau) = \exp(-Dq^2\tau_1) + \exp(-Dq^2\tau_2)$; the first exponential decay, at time constant $\tau_1 \sim 0.01$ms, is independent of waiting time while the second decay τ_2 increases with waiting time. We interpret the first decay as the result of the fluctuations of the binary solvent. Using the solvent viscosity $\eta = 1.2$mPas [9, 10], we obtain the size of the solvent fluctuation $R_{fluc.} \sim 30$ nm, which is close to the correlation length obtained by fitting the measured pair potential described in chapter 5. For the second decay, the increase of the time constant τ_2 with waiting time can

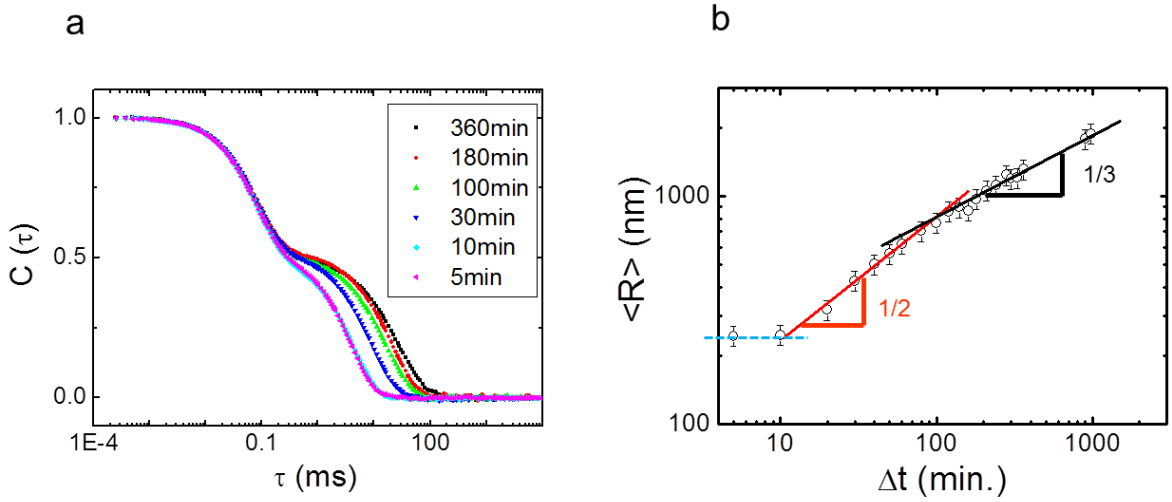

Figure 6.2: Light scattering measurement of the growth of the colloidal liquid phase.

(a) Reduced correlation as a function of delay time τ for different waiting times t_w measured at $\Delta T = 0.3$ °C revealing the fluctuations of the binary solvent (first decay at short times), and the diffusion of the colloidal liquid drops (second decay at longer times). (b) Average radius of colloidal liquid droplets as a function of time, determined from the second decay of the time correlation of the scattered intensity. The solid lines delineate an initial nucleation regime (blue dashed line), and two growth regimes $\langle R \rangle \propto t^{(1/2)}$ (red line), and $\langle R \rangle \propto t^{(1/3)}$ (black line), which are associated with diffusion limited and surface limited growth, respectively [11- 13].

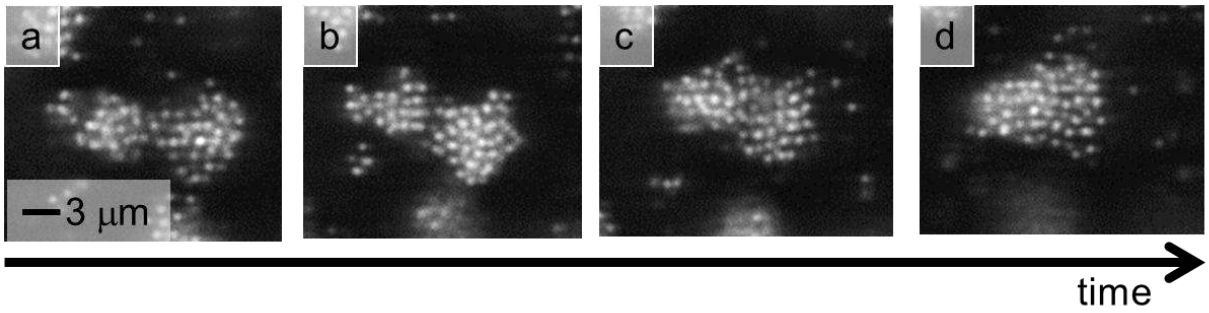

Figure 6.3: Large clusters grow by merging of small clusters. (a) Two small clusters start to merge. (b and c) The clusters are merging. (d) Merging completed.

be interpreted as the growth of particle aggregates. We use τ_2 to determine the mean aggregate radius $\langle R \rangle$ and show the resulting $\langle R \rangle$ as a function of time in Fig. 6.2b. The data indicates three regimes: the first regime, at Δt < 10 minutes, shows $\langle R \rangle \sim r0$, the radius of a single particle. Apparently, the growth of liquid phase is delayed, and we interpret this regime as the initial nucleation stage. The second regime, at 10 < Δt < 60 minutes, shows a growth according to $\langle R \rangle \sim t^{1/2}$. This time dependence agrees with that of surface-limited growth. Finally, the third regime, at Δt > 60 minutes, shows $\langle R \rangle \sim t^{1/3}$, reflecting diffusion-limited growth [11, 12]. These three growth regimes are confirmed by direct observation using confocal microscopy. The nucleation delays for 10 minutes after the desire temperature is reached, after that clusters form by aggregating of single particles, finally, large clusters form mostly by merging of small clusters growth (see Fig. 6.3). These observations of the time-dependence cluster size agree reasonably well with Ostwald's prediction of the cluster growth of molecular liquids and solids [14]. The large droplets grow at the expense of small ones. The agreement between our measurement and those of molecular liquids suggests that the growth of the liquid phase in the two systems follow similar mechanisms.

6.5. Confocal microscopy observation of liquid nucleation

To obtain insight into the nucleation of the colloidal liquid phase, we use confocal microscopy to image individual particles during the nucleation stage. This allows us to

follow the formation of nuclei and image their structure directly in three-dimensional space. We follow the same temperature protocol described in the dynamic light scattering measurement and use confocal microscopy to follow the appearance and disappearance of liquid nuclei. We show confocal microscope images at fixed temperature $\Delta T = 0.3°C$, and different waiting times in Fig. 6.4 a-c. After 10 minutes of waiting, a nucleus is clearly visible as indicated by the arrow in the confocal microscope image shown in Fig.6.4a. Interestingly, this nucleus breaks up again after a few seconds. After ~15min, a stable nucleus finally forms and grows (Fig. 6.4b). Subsequently, more stable nuclei form and grow, until after ~30min, small colloidal droplets coexist with a low density of particles outside (Fig. 6.4c).

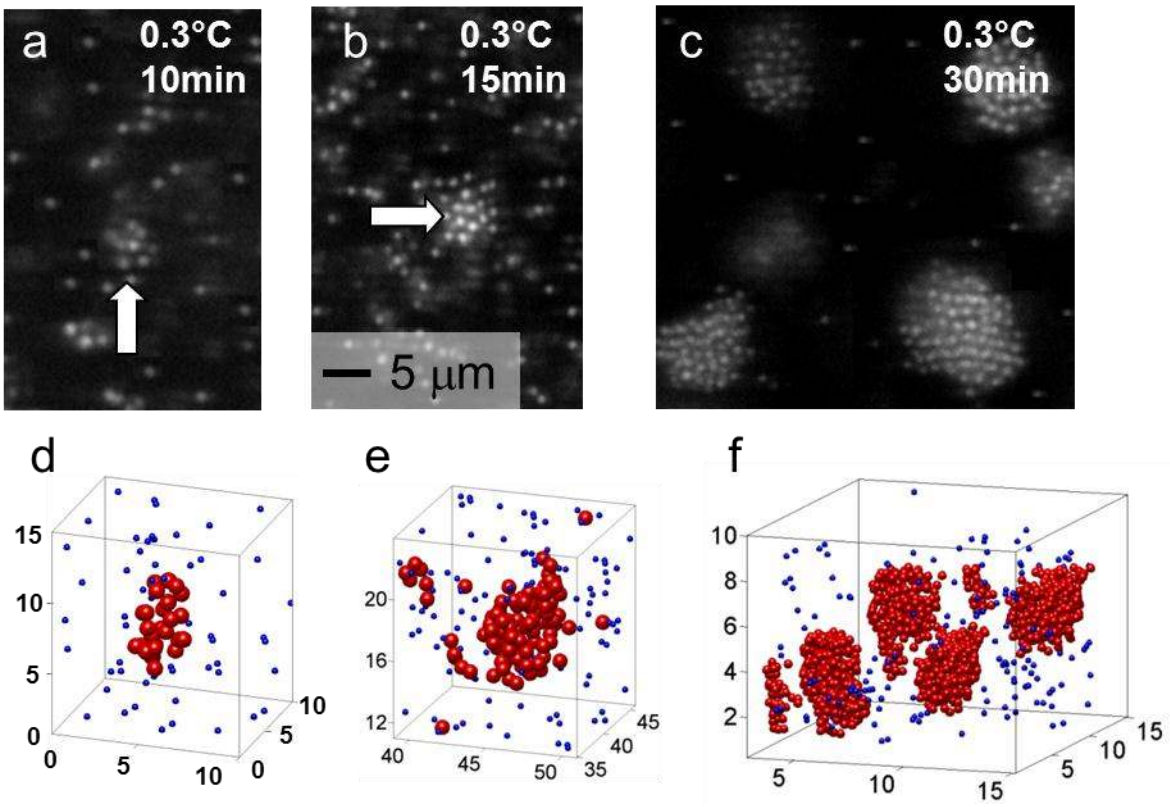

Figure 6.4: Colloidal liquid nucleation and growth.

(a-c) Confocal microscope images of colloidal liquid nucleation and growth: (a) arrow indicates a liquid nucleus that disappears within a few seconds. (b) Arrow indicates a nucleus that is stable and grows. (c) Colloidal liquid-gas equilibrium after 30min of growth. (d-f) Reconstructed images of liquid formation correspond to the confocal images (a-c). Red and blue spheres indicate particles with a large and small number of nearest neighbors, respectively. Red particles demarcate the unstable (d) and stable liquid nucleus (e), and the fully grown liquid drops (f).

We elucidate the nucleation of the liquid phase in more detail by showing three-dimensional reconstructions of the stable and unstable nuclei in Fig. 6.4d and e. We also show a reconstruction of the stable colloidal drops in Fig.6.4f. Large red spheres indicate particles with more than four nearest neighbors, and small blue spheres indicate particles with four or less nearest neighbors. Red particles accumulate in clusters demarcating a local high particle density. We elucidate the structure of the nuclei and fully grown drops by measuring the particle density ρ as a function of distance r from the nucleus center of mass. We show the result for selected nuclei in Fig. 6.5. Inside the fully grown drop, the density is constant to very good approximation, and exhibits a rather sharp decay to the density of the gas. From the plateau, we obtain the density $\rho_{lid} = 3.3\ \mu m^{-3}$ inside the liquid drops. For the two nuclei, there is no longer a plateau of constant density indicating that the density inside the nucleus is not uniform, while still the position of the surface can be determined from the rapid decay of ρ. These microscopic observations provide a unique opportunity for direct measurement of the critical radius r^* of liquid nucleation. The data shows that the radius of the unstable aggregate is approximately $4r_0$, while that of the stable nucleus is $6r_0$. Thus, $r_c \approx 5r_0$, in very good agreement with values found in computer simulations for Lennard-Jones liquids which are between 4 and $8r_0$, depending on the rate of cooling [5, 15, 16].

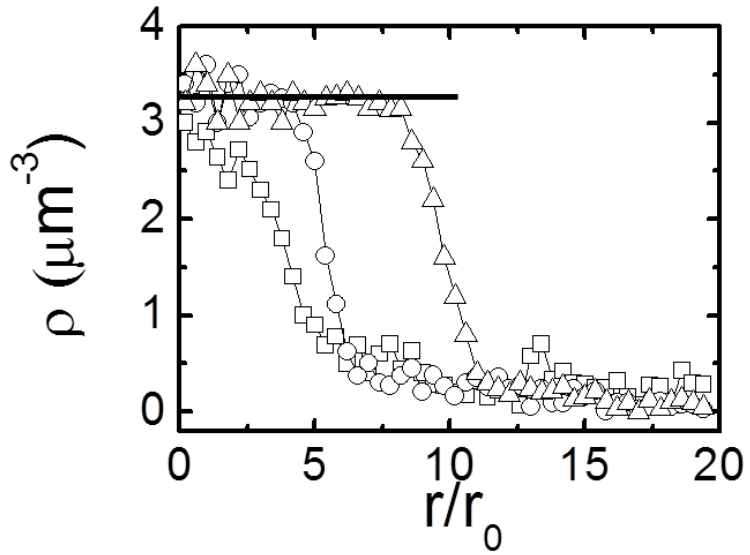

Figure 6.5: Particle density as a function of distance from the center of mass for the unstable liquid nucleus (squares), the stable nucleus (circles), and the fully grown droplet (triangles).

6.6 Free energy barrier as a function of supersaturation

We can also measure the nucleation barrier directly from the distribution of nuclei sizes. In thermal equilibrium, the probability P_n for a particle to be in a nucleus containing n particles is given by eq. (6.5). We can therefore measure the Gibbs free energy of nuclei directly from the observed frequency of particles to be in a cluster of size n. To do so, we image a large field of view, much larger than that used for the reconstruction of individual nuclei. An example of a large 3D reconstruction is shown in Fig. 6.6a. Many different cluster sizes are apparent, indicating a thermally equilibrated cluster size distribution. We count the total number N_n of clusters containing n particles to determine their probability of occurrence P_n according to $P_n = N_n/N$, where N is the total number of particles in the field of view. We show the resultant P_n as a function of cluster size in Fig. 6.6b, inset. The probability decreases exponentially with increasing cluster radius. We use this distribution to determine the Gibbs free energy ΔG as a function of cluster size, according to eq. (6.5). The resulting ΔG as a function of r is shown in Fig. 6.6b (open squares). They show the expected dependence of ΔG on nucleus size: For small nuclei, the Gibbs free energy increases with increasing radius R indicating the dominance of the surface energy

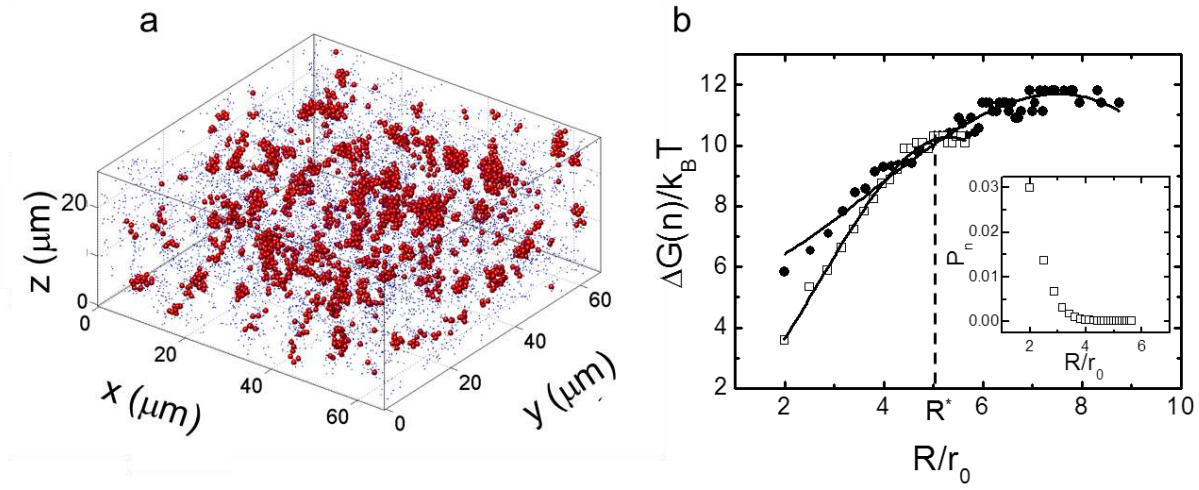

Figure 6.6: Cluster distribution and Gibbs free energy of clusters.

(a) 3D reconstruction gives an over view of cluster size distribution. Many different cluster sizes are apparent, indicating a thermally equilibrated cluster size distribution. (b) Gibb's free energy as a function of cluster size R, where r_0 is the particle size, at ΔT = 0.4 °C (dots) and at ΔT = 0.3 °C (open squares). Solid lines indicate fitting of CNT to the data. Dashed line indicates the critical radius of nuclei at at ΔT = 0.3 °C. Inset, Occurrence probability P_n of cluster containing n particles as a function of cluster size R.

over the bulk energy. The Gibbs free energy reaches a maximum $\Delta G_1^* \approx 10 k_B T$ at the critical cluster radius of $R_1^* = 5 \pm 0.5 r_0$ and a critical particle number of $n_1^* = 30 \pm 5$, after which it starts decreasing as a result of the dominance of the bulk energy. This critical radius is in very good agreement with the direct observation of stable nuclei, see Fig. 6.4. The measured form of ΔG versus r allows us to directly estimate the surface tension γ and chemical potential $\Delta\mu$. We fit the $\Delta G(r)$ curves with the function predicted by CNT (eq. 6.1). Assuming $\rho_{lid} = 3.3$ μm^{-3} determined from Fig. 6.3, the only free parameters are γ and $\Delta\mu$. We obtain $\Delta\mu_1 = 0.40\ k_BT$ and $\gamma_1 = 0.25\ k_BT/d_0^2$, where d_0 is the particle diameter; the corresponding curve fits the measurements very well. The values $\Delta\mu_1$ and γ_1 are in good agreement with simulations of Lenrd-Jones liquids, which find values in the range of $\Delta\mu =$ 0.10-0.7 k_BT and $\gamma =$ 0.1-1.0 k_BT/d_0^2 [5, 15-17]. However, these values should depend on the attraction of the particles. To elucidate this dependence, we perform the same measurement at ΔT = 0.4 °C corresponding to lower attractive potential between the particles. The resulting Gibbs free energy is indicated by solid circles in Fig. 6.6b. As result of the lower attraction, the nucleation barrier increases to $\Delta G_2^* \approx 11.8 k_B T$, while the critical cluster radius becomes $R_2^* = 7.2 \pm 0.5 r_0$ corresponding to $n_2^* = 75 \pm 10$ particles. The best fit from the data with CNT gives us $\gamma_2 = 0.12\ k_BT/d_0^2$ and $\Delta\mu_2 = 0.16\ k_BT$. Both values are smaller than the ones obtained at higher particles attraction. The lower values of $\Delta\mu$ reflect directly the lower degree of supersaturation associated with the lower attractive potential. The lower value of γ associates with weaker particle bonds. Again, this trend of is in good agreement with simulations in Lennard-Jones system and hard sphere colloidal crystallization [18].

6.7 Surface tension and the structure of critical nuclei

In this section, we aim to link the structure of critical nuclei and the particle pair potential directly to the measured surface tension. Following Kirwood and Buff theory eq. (6.13), the surface tension can be related to the pair potential $U(r)$ and the pair correlation function of the liquid structure [8, 19, 20]. To explore this relation, we measure the pair correlation function of liquid particles and show the results in Fig.6.7. Open squares show the pair correlation functions at ΔT = 0.3 °C (strong attraction) and solid circles show the

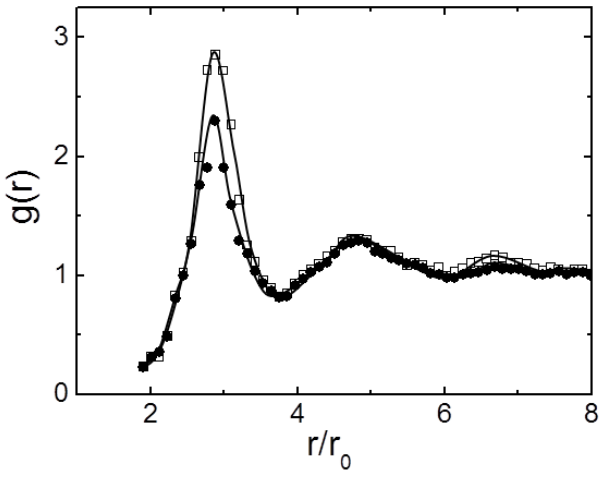

Figure 6.7: Pair distribution function of colloidal liquid at ΔT = 0.4 °C (dots) and at ΔT = 0.3 °C (open squares). Stronger attraction at ΔT = 0.3 °C gives rise to the higher peak of $g(r)$ indicating higher degree of short-range order. Lines indicate polynomial fit to the data.

pair correlation functions at ΔT = 0.4 °C (weaker attraction). Remarkably, a clear change of the pair correlation function is observed: at stronger attraction (higher degree of supersaturation) the first peak of $g(r)$ is higher indicating higher degree of short-range order associated with the stronger bonds. The pair potentials corresponding to these temperatures have been shown shown in Fig. 5.11a. To calculate the integral (6.13) we fit $g(r)$ and $U(r)$ with polynomial functions and insert these functions into the Kirkwood-Buff integral. We then set the lower limit of the integration to the position where the particle pair potential reaches its minimum, since only the attractive part of pair potential contributes to the surface tension [20]. Doing so, we obtain values of surface tension $\gamma_1^{KB} = 0.40 k_B T / d_0^2$ and $\gamma_2^{KB} = 0.20 k_B T / d_0^2$ at ΔT = 0.3 °C and ΔT = 0.4 °C, respectively, which show the same trend as the surface tensions γ_1 = 0.25 k_BT/d_0^2 and γ_2 = 0.12 k_BT/d_0^2 determined from the cluster size distribution but are almost factor of two larger. This difference is reasonable given the crude assumptions of an infinitely dilute gas and an infinitely narrow interfacial width. The second assumption of constant density inside the liquid in particular does not hold as shown in Fig. 6.5. The data shows that the width of the interface and the density distribution changes with the nucleus size, leading to a size-dependent surface tension [21, 22]. In contrast, CNTassumes the surface tension is independent of the cluster size. Nevertheless γ_1 / γ_2 and $\gamma_1^{KB} / \gamma_2^{KB}$ are quite similar

confirming the surface tension is proportional to the well depth of the pair potential and the nucleation and growth process is finely tuned by controlling critical Casimir forces.

6.8 Conclusions

In conclusions, by using critical Casimir forces to control particle interactions, we investigated the nucleation and growth of colloidal liquids. The use of the complementary techniques, light scattering and confocal microscopy allowed us to follow all stages of the nucleation and growth process, and to test classical theories of nucleation and growth. We used dynamic light scattering to have an overview of the nucleation and growth process. The result shows that the growth process is divided into three regimes: initial nucleation, surface limited growth, and diffusion limited growth. The latter two regimes are in very good agreement with Ostwald ripening for molecular liquids and solids. On the other hand, we used confocal microscopy to follow the formation and break up of liquid nuclei directly in real space and we determined the critical radius above which nuclei are stable and grow. We then used the cluster size distribution to reconstruct the Gibb's free energy barrier of nucleation, assuming thermal equilibrium of cluster sizes. This measured free energy curve could be very well fitted by the classical nucleation theory prediction, and we used the fit to determine the important parameters surface tension and chemical potential. Furthermore, we showed that the exquisite temperature control of the particle pair potential via critical Casimir forces allowed us to even change the amount of suspersaturation. We determined that at lower attraction, the energy barrier for nucleation becomes larger, reflecting the lower degree of supersaturation. Finally, using Kirwood and Buff theory, we linked the structure of critical nuclei and the particle pair potential directly to the measured surface tension. While we find qualitative agreement, the value of surface tension computed from the structure and pair potential is a factor of two larger, indicating the need for a more refined model. Our results, from different methods, are consistent and in good agreement with simulation results on Lennard-Jones liquids suggesting that this colloidal system is a good model for molecular liquids.

Bibliography

[1] P. G. Debenedetti, Metastable liquids: Concepts and Principles, New Jersey: Princeton University Press, 1996.

[2] J. Prenkel, Kinetic theory of liquids, New Your: Dover, 1995.

[3] R. Becker and W. Doring, *Mol. Phys.,* vol. 24, p. 719, 1935.

[4] A. C. Zettelemoyer, Nucleation, New Your: Dekker, 1969.

[5] P. R. ten Wolde and D. Frenkel, "Computer simulation study of gas–liquid nucleation in a Lennard-Jones system," *J. Chem. Phys.,* vol. 109, p. 9901, 1998.

[6] Benjamin J. Block, Subir K. Das, Martin Oettel, Peter Virnau, and Kurt Binder, "Curvature dependence of surface free energy of liquid drops and bubbles: A simulation study," *J. Chem. Phys.,* vol. 133, p. 154702, 2010.

[7] David S. Corti,a) Karl J. Kerr, and Korosh Torab, "On the interfacial thermodynamics of nanoscale droplets and bubbles," *J. Chem. Phys.,* vol. 135, p. 024701, 2011.

[8] J. G. Kirwood and F. P. Buff, "The Statistical Mechanical Theory of Surface Tension," *J. Chem. Phys.,* vol. 17, p. 338, 1949.

[9] L.-C. Wang, H.-S. Xu, J.-H. Zhao, C.–Y. Song, F.-A. Wang,, "Density and viscosity of (3-picoline + water) binary mixtures from T=(293.15 to 343.15)," *J. Chem. Thermodynamics,* vol. 37, p. 477, 2005.

[10] A. Oleinikova, L. Bulavin and V. Pipich, "The Viscosity Anomaly Near the Lower Critical Consolute Point,," *Int. J. Thermophys,* vol. 20, p. 889, 1999.

[11] I.M. Lifshitz and V.V. Sloyozov, *J. Phys. Chem. Solids,* vol. 19, p. 35, 1961.

[12] C. Wagner, "Theorie der Alterung von Niederschlägen durch Umlösen (Ostwald-Reifung)," *Zeitschrift fur Elektrochemie,* vol. 65, p. 581, 1961.

[13] J. Carr, O. Penrose, "Asymptotic behavior of solutions to a simplified Lifshitz-Slyozov equation," *Physica D,* vol. 124, p. 166, 1998.

[14] W. Ostwald, *Lehrbuch der Allgemeinen Chemie,* vol. 2, 1896.

[15] Y. Hirata, "Molecular dynamics simulation of the vapour liquid transition of argon and the reaction," *Mol. Phys.,* vol. 108, p. 3383, 2010.

[16] M. Santra, S. Chakrabarty, and B. Bagchi, "Gas-liquid nucleation in a two dimensional system," *J. Chenm. Phys.,* vol. 129, p. 234704, 2008.

[17] Matthias Mecke, Jochen Winkelmann, and Johann Fischer, "Molecular dynamics simulation of the liquid–vapor interface: The Lennard-Jones fluid," *J. Chem. Phys.,* vol. 107, p. 9264, 1997.

[18] U. Gasser, Eric R. Weeks, Andrew SchoÞeld, and P. N. Pusey, "Real-Space Imaging of Nucleation and Growth in Colloidal Crystallization," *Science,* vol. 292, p. 258, 2001.

[19] M. V. Berry, R. F. Durrans, and R. Evans, "The calculation of surface tension for simple liquids," *J.*

Chem. A: Gen. Phys., vol. 5, p. 166, 1972.

[20] R. Defay, I. Prigogine, and A. Bellemans, Surface tension and adsorption, Bristol: Longmans, Green & Co Ltd, 1966.

[21] J. Merikanto, E. Zapadinsky, A. Lauri, and H. Vehkamaki, "Origin of the Failure of Classical Nucleation Theory: Incorrect Description of the Smallest Clusters," *Phys. Rev. Lett.,* vol. 98, p. 145702, 2007.

[22] A. E. van Giessen and E. M. Bolkhuis, "Determination of curvature corrections to the surface tension of a liquid–vapor interface through molecular dynamics simulations," *J. Chem. Phys.,* vol. 116, p. 302, 2002.

[23] J. Wedekind, G. Chkonia, J. Wölk, R. Strey, and D. Reguera, "Crossover from nucleation to spinodal decomposition in a condensing vapor," *J. Chem. Phys.,* vol. 131, p. 114506, 2009.

Chapter 7

Out-of-equilibrium assembly by critical Casimir forces

Active control over the aggregation of particles has important applications for the design of new nanostructured materials. In the two preceding chapters we have investigated phase equilibria due to critical Casimir forces. Here, we explore structures formed out-of-equilibrium by quenching the particles into a strongly attractive state. We demonstrate that via active control of the particle pair potential, we can quench the particles into well-defined aggregate structures with direct control of their morphology. By imaging the morphology in three dimensions, we show that the resulting structures are fractals, with a fractal dimension that is controlled precisely by the temperature quench. We use Monte Carlo simulations of diffusion-limited aggregation to relate the aggregate morphology to the particle pair potential. These results open a new route of control in the assembly of colloidal and nano-scale structures.

7.1 Introduction

Controlling the structure of aggregates is important for applications as diverse as filters, catalyzers, and electronic devices. The functionality of devices requires aggregate structures with specifically designed surface to volume ratio, morphology, and characteristic structural length scales. However, achieving specific aggregate structures by design is a difficult task, and there is no general framework to achieve active control over the aggregation process. In fact, usually such aggregation processes are irreversible with very little control over the resulting structures. Because of its importance, colloidal aggregation has been investigated intensely. The important low-density regimes of diffusion-limited aggregation (DLA) and reaction-limited aggregation (RLA) [1], where the particles stick irreversibly due to strong attractive interactions, have been much investigated in simulations and shown to exhibit universal features with well-defined fractal dimensions. In experiments, it is rather diffusion and reaction limited *cluster* aggregation that is observed [2, 3]. In this case, it is the growing fractal clusters that get attached to each other rather than single particles. This leads to lower fractal dimensions compared to DLA. Much more relevant for applications, however is the regime of lower attractive potential, where because of particle detachment denser structures can form; this regime is much less explored [4, 5]. Consequently much less is known about the structures formed, and their dependence on the attractive potential. The reversible control of particle attraction by critical Casimir forces offers new opportunities to explore this regime, and to control the morphology and fractal dimension of colloidal aggregates by design.

In this chapter, we investigate the morphology of fractal structures that form when particles can detach from the growing aggregate with a finite probability. We combine experimental- and simulation studies of colloidal aggregation: In the experiment, we use critical Casimir forces to quench the particles in a state of well-defined attraction. We follow the diffusion-limited cluster aggregation as a function of the quench depth. We find that we can assemble the particles into aggregates with well-defined morphology and fractal dimension. We elucidate the relation between their fractal dimension, characteristic cluster length scale, and the depth of temperature quench by imaging the resulting structures at the particle scale. In the simulation, we use Monte Carlo simulations of diffusion-limited aggregation (DLA) with finite particle dissociation probability to model the aggregation process. This allows us to link the change of morphology and fractal

dimension directly to the attractive potential strength. We show that even at finite attractive potential, the aggregation exhibits universal properties: the change of fractal dimension with particle pair potential appears to be independent of the nature of the interaction, the type of aggregation, and the dimensionality.

7.2 Experimental control of the aggregate morphology with critical Casimir forces

The temperature dependence of the critical Casimir force allows us to explore out-of-equilibrium behavior by actively quenching the particles into states of different attractive strength. To do so, we use pNipam colloids suspended in a binary solvent consisting of 28 %wt 3mp (see chapter 5), and we employ a special heating setup consisting of two independent water circles to quench the system quickly and reliably to a temperature ΔT below the phase separation temperature T_{cx}. We first equilibrate the suspension at ΔT = 0.7°C, where critical Casimir forces are still negligible. Then, by switching the water cycle, we jump to the desired final temperature to achieve a well-defined attractive critical

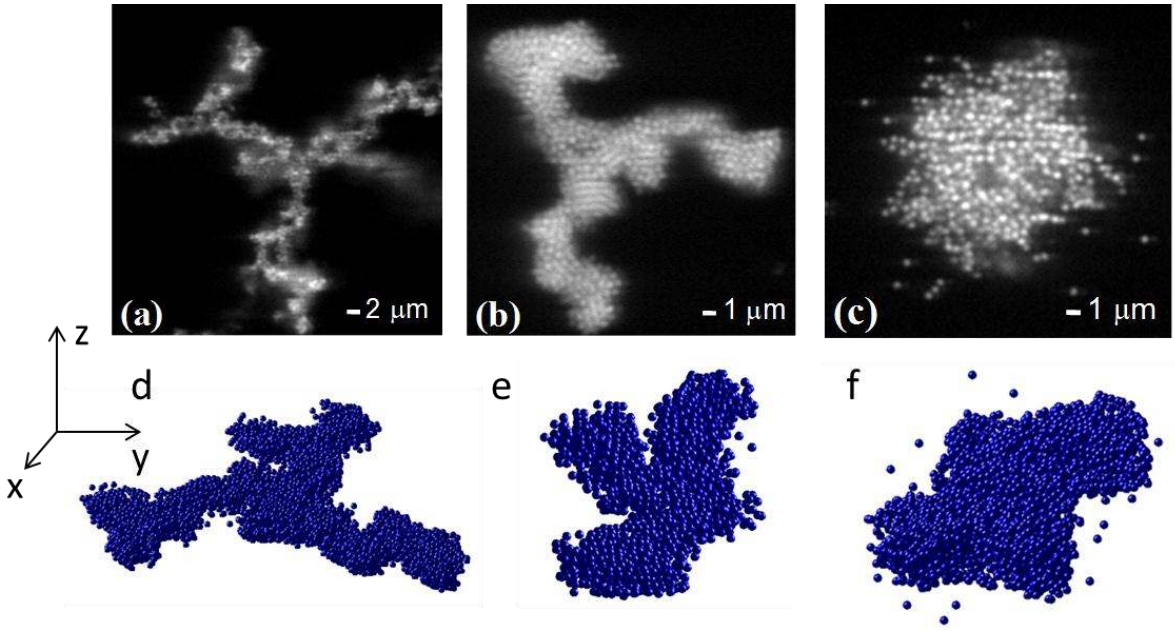

Figure 7.1: Tuning the morphology of colloidal aggregates by critical Casimir forces. Confocal microscope images and three-dimensional reconstruction of aggregates resulting from temperature quenches to ΔT = 0.12 °C (a, d), 0.14 °C (b, e), and 0.2 °C (c, f) below the phase separation temperature of the binary solvent.

Casimir potential. After an hour, we image the resulting structures with confocal microscopy and obtain 3D reconstructions of the aggregate structures. The controlled temperature quench allows us to form aggregates with well-defined morphologies. This is demonstrated in Fig. 7.1, where we show confocal microscope images and three-dimensional reconstructions of typical aggregates obtained at various ΔT. With increasing ΔT, the structure of the aggregate changes from open, ramified (Fig. 7.1a, d) to dense and compact (Fig. 7.1c, f). These morphologies remain essentially unchanged over several hours as long as we hold the temperature fixed. We characterize the compactness of the structures by determining the number N of particles within a distance r to the cluster center. The data in Fig. 7.2a shows that, in good approximation, $N \sim r^{d_f}$, indicating that the structures are fractals on intermediate length scales. We conclude that even when the morphology becomes more compact, the fractal structure persists. We find, however, that the fractal dimension increases with ΔT as shown by the increasing slopes in Fig. 7.2a. This is confirmed when we analyze many more clusters, and plot the fractal dimension as a function of ΔT in Fig. 7.2. The fractal dimension increases continuously from $d_f \sim 2.1$, at small ΔT to $d_f \sim 3$ at larger ΔT, confirming that the structures become more dense as the attractive strength decreases. These results demonstrate that by controlling the temperature quench, we can assemble structures with well-defined morphology and fractal dimension. By varying the temperature quench, we can continuously tune the morphology and structural properties of the aggregates.

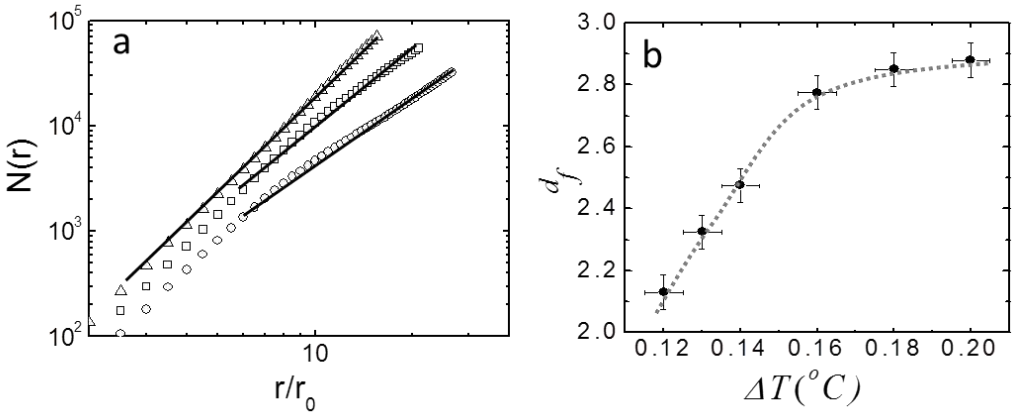

Figure. 7.2: (a) Scaling of the number of particles $N(r)$ with distance r/r_0 from the cluster center for selected temperatures: ΔT = 0.12 °C (circles), 0.14 °C (diamonds), and 0.2 °C (hexagons). (b) Fractal dimension as a function of temperature ΔT, determined from the slopes in (a). A continuous increase of the fractal dimension towards the spatial dimension $D = 3$ is observed.

7.3 Monte Carlo simulation study of the fractal morphology

To elucidate how the change in morphology is related to the particle attractions, we perform Monte Carlo simulations of diffusion-limited particle aggregation. We carry out simulations in two and three dimensions, and model finite bond energies by a finite dissociation probability α with which particles can detach from the growing cluster. The particles move on two and three-dimensional square lattices following a random walk, until they get attached to the cluster. Singly bonded particles can dissociate from the cluster with probability α, and the detached particle then diffuses until it sticks to the cluster again. This procedure is repeated until there is a collection of 10^4 particles in the cluster. We first generate clusters, using 2D simulations, for a wide range of dissociation probabilities; different dissociation probabilities lead indeed to very different morphologies, as shown by the renderings of the final clusters in Fig. 7.3. Clear changes in the cluster morphology from a highly ramified fractal structure at $\alpha = 0$ to increasingly compact structures at higher α are observed. We measure the fractal dimension as before from the scaling of the number of particles as a function of distance from the cluster center. Two examples are shown in Fig. 7.4a. Indeed, $N(R) \sim R^{d_f}$ over almost the entire range of R, in agreement with our experimental observations. The resultant fractal dimension is shown as a function of α in Fig. 7.4b; it increases continuously from the DLA limit d_f^{DLA}=1.66 [6] to the dimension of space D = 2, see Fig. 7.4b, main panel. We plot $D - d_f$ as a function of α in Fig. 7.4b (inset). Interestingly, for sufficiently large α the

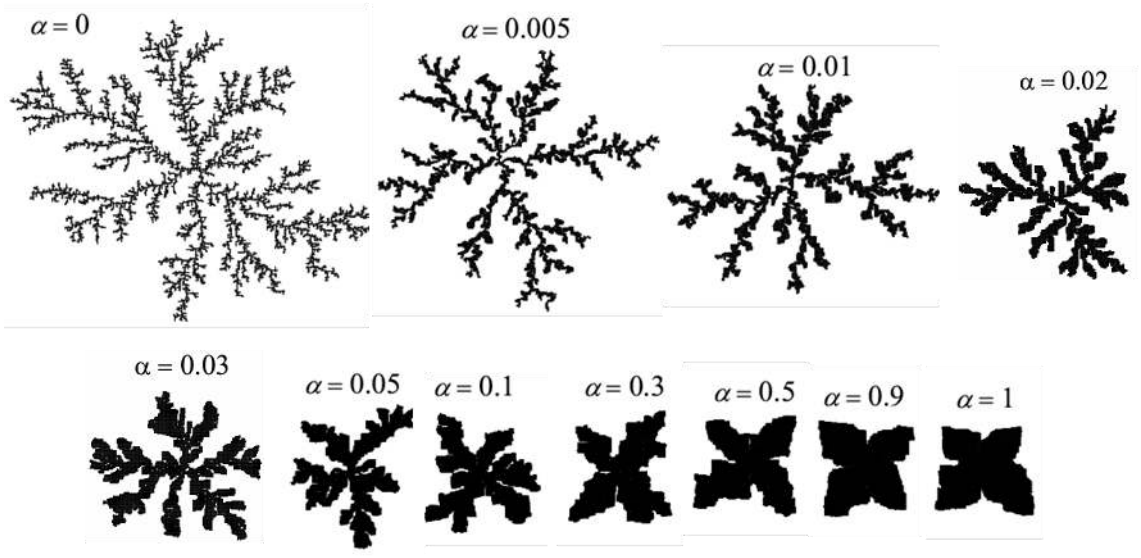

Figure 7.3: Diffusion limited aggregate cluster generated for various values of rate of dissociation *a*.

fractal dimension is well described by $D - d_f \propto \alpha^{-\mu}$, where the exponent $\mu = 0.65 \pm 0.01$ (solid line in Fig. 4b). At lower α, this power-law relation no longer holds, possibly because at small α, the structure does no longer adjust on the simulation timescale.

The changing morphology leads to a dramatic change in the number N_p of particles at the perimeter of the cluster, see Fig. 7.5. In the highly ramified structures ($\alpha \sim 0$), most of the particles sit at the perimeter of the structure, while with increasing α, the number of perimeter particles drops rapidly, in agreement with the decreasing surface to volume ratio observed in the experiments. This change in the number of perimeter particles provides a

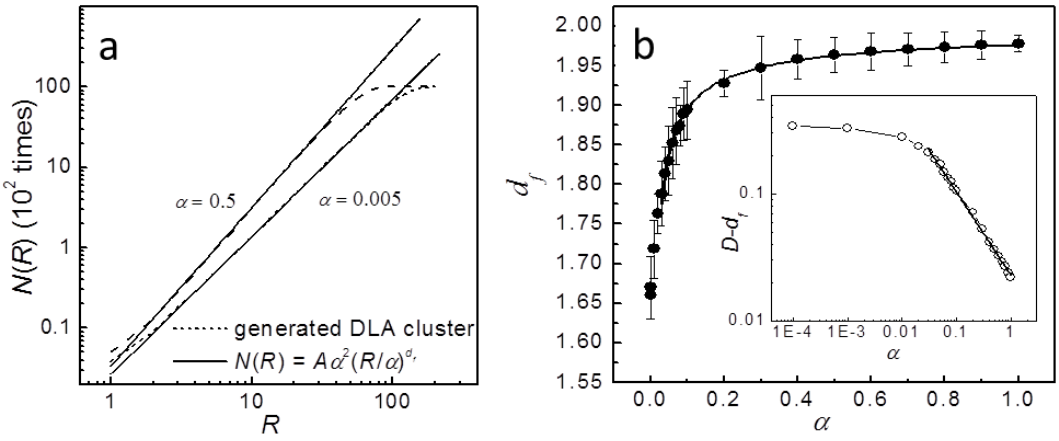

Figure. 7.4: 2D Monte Carlo simulations of cluster. (a) Representative graphs of $N(R)$versus R on log-log scale for the DLA cluster for =0.005 and 0.5. (b) Plot of variation of fractal dimensions d_f versus rate of dissociation a. Inset graph shows variation of (D-d_f) VS a on log-log scale, with linear fit in the region from a = 0.03 to 1.

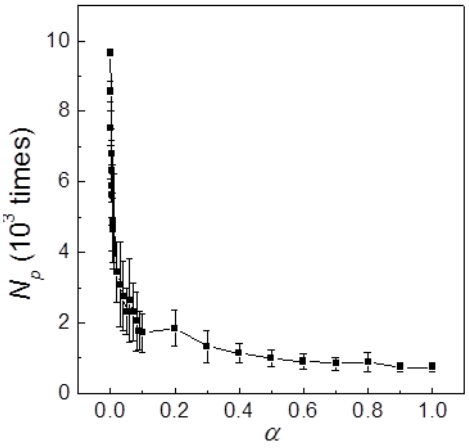

Figure 7.5: 2D Monte Carlo simulations results of the number of particles at the perimeter of the structure as a function of dissociation probability a demonstrates dramatic change of the cluster morphology. The low dissociation probability is directly reflected in the large number of particles at the perimeter.

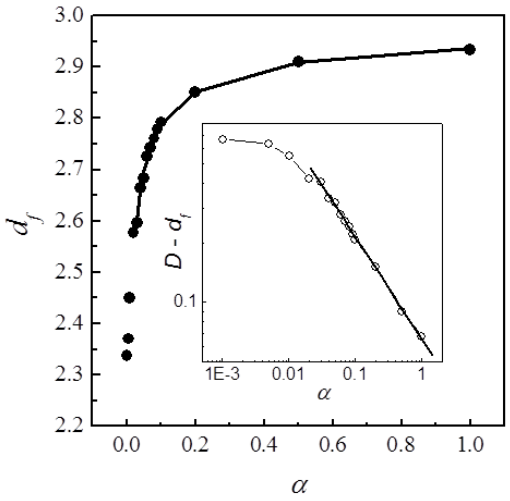

Figure 7.6: 3D Monte Carlo simulations of clusters: Variation of the fractal dimensions d_f with rate of dissociation α. Inset shows the variation of (D-d_f) versus α on a log-log scale, with linear fit in the region from $\alpha = 0.03$ to 1.

crucial link between α and the changing fractal structure. At small dissociation probability, many more particles sit at the perimeter where they are relatively stable and dissociate only slowly. At higher dissociation probability, fewer particles sit at the perimeter, as a result of the higher dissociation rate that allows for structural rearrangement. The final aggregate structure results from the balance of morphology-dependent dissociation and restructuring due to re-attachment of particles. We perform similar simulations on a three-dimensional lattice. We find that, similarly, a relation of the form $D - d_f \propto \alpha^{-\mu}$ holds, where $D = 3$ (see figure 7.6). However, the value of exponent in this case is found to be $\mu = 0.53 \pm 0.01$.

7.4 Discussion

To compare quantitatively the cluster morphology change observed in the experiments and simulations, we relate the dissociation probability to the particle pair potential. Assuming thermally activated dissociation of particles, we can link the dissociation probability α in the simulations directly to an effective pair potential $V(r)$, using $\alpha \propto e^{-V_0/kT}$, where, the energy barrier V_0 is associated with depth of the potential $V(r)$. This effective pair potential can be extrapolated from direct measurement: as shown in chapter 5, at low attraction, the

potential can be measured from the pair distribution function in dilute systems. Here, we use these measurements to extrapolate the potential depth to somewhat stronger attraction. We show the potential depth $-V_0$ as a function of ΔT in Fig. 7.7. Filled symbols indicate the experimental measurements. To extrapolate to stronger attraction, we follow the observation of Bechinger *et al* [7] that the potential depth increases exponentially with ΔT. We fit the experimental data points with an exponential function, and extrapolate to lower ΔT, see the solid line in Fig. 7.7. The exponential function does indeed fit the measurements well. The resulting extrapolated potential depths, which correspond to the temperature quenches used in this chapter, are shown as open symbols in Fig. 7.7.

We can now compare the experimental and simulated aggregate structures; we do this by plotting the variation of the fractal dimensions (D-d_f) as a function of α for both experiments and 2D and 3D simulations in Fig. 7.8. Two crucial points can be noticed: first, by choosing b, we can collapse the two- and three-dimensional simulations and the experiments, indicating a common underlying mechanism. Second, for large α, a linear relation between (D-d_f) and α is observed, indicating that the aggregate structure changes continuously, and in a surprisingly linear way with the attractive potential. These observations highlight a general feature of the aggregation: although the different mechanism of aggregation, DLA in the simulations and DLCA in the experiment, results in different values of the fractal dimension, the relative changes of the fractal dimension are similar. Moreover, simulations by Shih *et al* [8] on a reversible growth model for

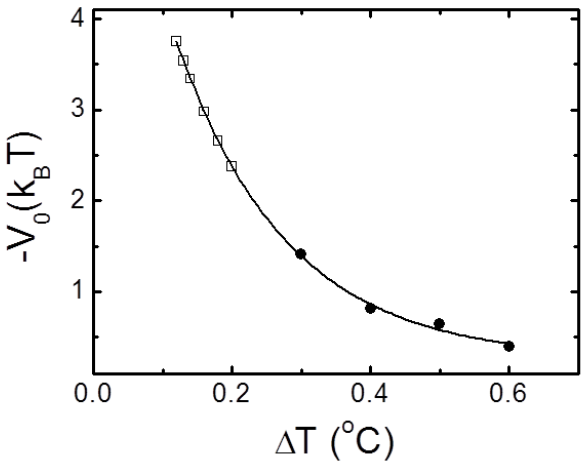

Figure 7.7: Experimental potential depth $-V_0$ as a function of DT: solid circles are measured values, open squares are extrapolated values, line is an exponential fit.

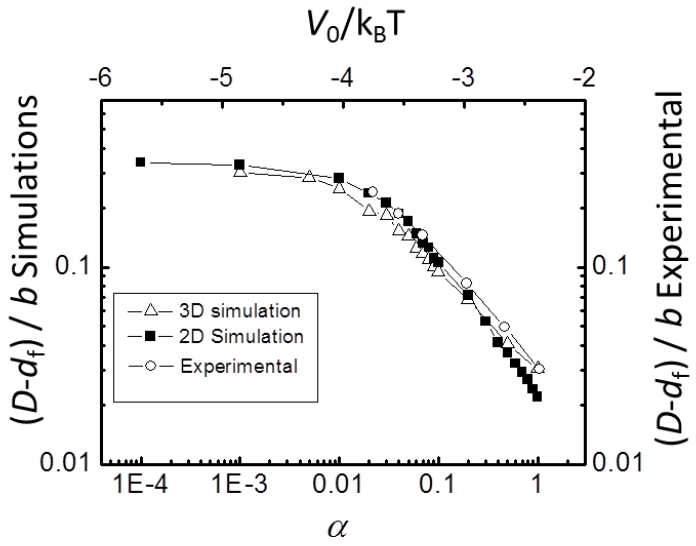

Figure 7.8: Variation of the fractal dimensions $(\mathrm{D} - d_f)/b$ versus α for experiments and simulations in 2D and 3D. Here, b is a scaling factor.

cluster-cluster aggregation and experiments by Pusey *et al* [9] for a system of colloid-polymer mixtures, have reported that the fractal dimension is almost constant at large attraction energy E, but it increases drastically with decreasing E when $E \leq 3k_BT$. In both cases, they observed fractal dimensions from d_f =1.9 to d_f =3 which is in good agreement with our experiments as well as simulations. Our direct comparison of experiments, and 2 and 3D simulations demonstrates that the morphology change exhibits universal properties, being independent of dimensionality, nature of the underlying lattice and the specific aggregation process.

7.5 Conclusions

In conclusion, we have shown that we can tune the morphology of colloidal aggregates continuously with exquisite control over their fractal dimension by combining critical Casimir forces with controlled temperature quenches. The controlled temperature quench forces the system in a state of well-defined attraction, allowing us to elucidate the formation of out-of-equilibrium structures. Comparison with simulations of diffusion-limited aggregation in two and three dimensions demonstrates that the underlying relation

between fractal dimension and attractive particle potential exhibits universal properties. Direct potential control such as that afforded by the critical Casimir effect can thus be used to precisely tune the average architecture of such out-of-equilibrium structures to yield specific branch thickness, surface-to-volume ratio, and fractal dimension. Such direct morphology control offers new opportunities for applications as for example to design specific structures required to reach specific functionality in devices.

Bibliography

[1] D. A. Weitz, J. S. Huang, M. Y. Lin, and J. Sung, "Limits of the Fractal Dimension for Irreversible Kinetic Aggregation of Gold Colloids," *Phys.Rev. Lett.,* vol. 54, p. 1416, 1985.

[2] R. C. Ball, D. A. Weitz, T. A. Witten, and F. Leyvraz, "Universal kinetics in reaction-limited aggregation," *Phys. Rev. Lett.,* vol. 58, p. 274, 1987.

[3] M. Y. Lin, H. M. Lindsay, D. A. Weitz, R. C. Ball, R. Klein, and P. Meakin, "Universality in colloid aggregation," *Nature,* vol. 339, p. 360, 1989.

[4] P. J. Lu, E. Zaccarelli, F. Ciulla, A. B. Schofield, F. Sciortino & D. A. Weitz, "Gelation of particles with short-range attraction," *Nature,* vol. 453, p. 499, 2008.

[5] W. C. K. Poon, A. D. Pirie and P. N. Pusey, "Gelation in colloid-polymer mixtures," *Faraday Discuss,* vol. 101, p. 65, 1995.

[6] T. A. Witten and L. M. Sander, "Diffusion-Limited Aggregation, a Kinetic Critical Phenomenon," *Phys. Rev. Lett.,* vol. 47, p. 1400, 1981.

[7] C. Hertlein, L. Helden, A. Gambassi, S. Dietrich, C. Bechinger, "Direct measurement of critical Casimir forces," *Nature,* vol. 451, p. 172, 2008.

[8] Wan Y. Shih, Ilhan A. Aksay, and Ryoichi Kikuchi, "Reversible-growth model: Cluster-cluster aggregation with finite binding energies," *Phys. ReV. A,* vol. 36, p. 5015, 1987.

[9] W. C. K. Poon, and P. N. Pusey, in Observation, Prediction and Simulation of Phase Transitions in Complex Fluids, Boston: Kluwer Academic, 1995.

Summary

Colloids are widely used because of their exceptional properties. Beside their own applications in food, petrol, cosmetics and drug industries, photonic, optical filters and chemical sensor, they are also known as powerful model systems to study molecular phase behavior. In this thesis, we have examined both aspects of colloids using temperature-sensitive colloidal systems to fully investigate colloidal phase behavior and colloidal assembly. The thesis contains two major subjects; in the first part, we have investigated the crystal-fluid transition and the free energy at colloidal crystal-fluid interfaces. In the second part, we have studied colloidal phase transition and assembly induced by critical Casimir forces.

The direct observation of the crystal-fluid interface is difficult because it is buried between two dense phases of closely similar densities, but different structural order. We overcome this difficulty using a refractive-index matched system, containing pNipam colloids and water, and recent confocal microscopy techniques. Since the size of the pNipam particles, and therefore, the volume fraction of the suspension change with temperature, large crystal-fluid interfaces are achieved by using a temperature-gradient technique. We use confocal microscopy to follow directly the heterogeneous crystal nucleation, the advancing interface and the stationary interface at the particle scale. For the advancing interface, we measure the growth velocity of the crystal and diffusion coefficient of fluid particles and use them to determine the chemical potential difference between crystal and fluid phases. We investigate the effect of impurities on the advancing interface and

determine the critical force needed to overcome impurity particles from the local interface curvature.

For the stationary interface, we follow the changes from the short-range order of the fluid to the long-range order of the crystal. Our result is in very good agreement with simple atomic systems; the maximum short-range density of the fluid is achieved with icosahedral configurations. These icosahedral units exhibit five-fold rotational symmetry that is incompatible with a periodic filling of space. This incompatibility leads to a first-order transition that separates crystal and fluid phases. At the interface to the crystal, the number of possible packing configurations of the fluid is reduced with respect to the bulk fluid, resulting in a loss of configurational entropy that provides the dominant contribution to the interfacial energy.

We establish a direct link between structure and free energy by measuring the free energy change across the interface from the 3D particle configurations. The 3D imaging allows us to directly measure the free volume and the free surface area available for insertion of additional particles; thus the interfacial free energy and the interfacial tension of crystal-fluid interfaces are determined. Because of its structural origin, the interfacial tension depends on the direction of the interfacial plane with respect to the crystal lattice and is anisotropic. This anisotropy plays an important role in crystal nucleation and the morphological stability of crystal growth; however, its direct experimental measurement is prohibitively difficult, and this anisotropy has mostly been inferred from macroscopic measurements. We used thermally excited interface fluctuations to measure the interfacial tension and its small anisotropy. The measured interfacial tensions, from both methods, agree well with simulation values of hard spheres and slightly soft spheres, while the anisotropy is surprisingly larger than that found in simulations.

In the second part of the thesis, we demonstrated the active assembly control of equilibrium and out-of-equilibrium phases using attractive critical Casimir forces. These forces arise due to concentration fluctuations of the critical binary solvent, and therefore, the magnitude and range of this attraction is set by the solvent correlation length, and can be adjusted with temperature. Using a low quench rate, we guide the colloidal particles into analogues of molecular liquid and solid phases via exquisite control over the particle interactions. We measure the pair distribution and pair potential of the particles directly by following density fluctuations in the colloidal gas. This allows us to elucidate the

applicability of continuum models to the colloidal assembly process. We apply the van der Waals model of molecular liquefaction to show that the colloidal gas-liquid condensation is accurately described by the Van der Waals theory, even on the scale of a few particles.

The microscopic insight of the experiment provides direct input for simulations to investigate the full phase behavior of colloids induced by the critical Casimir forces. We, therefore, use experimentally measured particle pair potentials and Monte Carlo simulations to fully investigate the phase behavior of colloids in binary liquid solvents. This combination allows us for the first time to simulate phase equilibria due to critical Casimir forces. We locate colloidal gas, liquid and solid phases as a function of temperature and colloid volume fraction. The resulting colloidal phase diagram agrees well with experiment and has the characteristic topology associated with molecular potentials like the Lennard-Jones, but occurs over a very narrow temperature range due to the strong temperature dependence of the critical Casimir interactions.

The homogeneous nucleation of a liquid from its vapor is of fundamental interest to our understanding of the formation of phases in first order transitions. Despite its importance, direct observation of the nucleation of the liquid phase is prohibitively difficult at the molecular scale. Here, we show that the application of critical Casimir forces on a colloidal gas provides direct images of liquid nucleation in real time and on the single particle level, allowing us to visualize the effects of thermal fluctuations in the nucleation fluctuations. We implement a new way to measure the free energy of the liquid cluster, surface tension and chemical potential difference between gas and liquid phases directly from the cluster size distribution. We also determine the surface tension directly from the particle pair potential and structure of liquid cluster at different degrees of supersaturation. These results provide a unique opportunity to test the applicability of nucleation theories.

Finally, we study in detail the morphology change of fractal structures by complementing experimental control via critical Casimir forces with Monte Carlo simulations of diffusion-limited aggregation. On the one hand, with high quench rate we quench the particles into a state of high attraction and assemble them into aggregates with well-defined morphology. We elucidate the relation between the fractal dimension and the potential depth by imaging the resulting structures. On the other hand, we use Monte Carlo simulations of diffusion-limited aggregation with finite particle dissociation probability to model the aggregation process, and relate the resulting structures to the particle dissociation

probability and, therefore, to the attractive potential strength. A good agreement between simulations and experiments allows us to conclude that the diffusion limited aggregation exhibits universal properties, being independent of the nature of the interaction and the dimensionality.

Our results confirm that the temperature-sensitive colloidal system, on the one hand, is a powerful model system to study molecular phase behavior, and on the other hand, opens up new possibilities in the active assembly of micro and nanostructures.

Samenvatting

Colloïden worden op vele gebieden gebruikt voor hun exceptionele eigenschappen. Naast hun toepasbaarheid in de voedsel, petrochemische, cosmetische en farmaceutische industrie en in de fotonica, optische filters en chemische sensoren, staan ze ook bekend als een zeer sterk model systeem voor moleculair fasegedrag. In dit proefschrift hebben we deze beide aspecten van colloïden onderzocht door gebruik te maken van temperatuur gevoelige colloïdale systemen om het colloïdale fasegedrag en de colloïde organisatie vast te leggen. Dit proefschrift bestaat uit twee hoofdonderwerpen: in het eerste deel hebben we de kristal-vloeistof overgang en de vrije energie op het colloïdale kristal-vloeistof grensvlak onderzocht. In het tweede deel, bestudeerden we colloïdale faseovergangen en organisatie geïnduceerd door kritische Casimir krachten.

Het direct observeren van het kristal-vloeistof grensvlak is moeilijk omdat het begraven ligt tussen twee fasen met een zeer hoge en gelijkwaardige dichtheid, maar met verschillende structurele ordening. We lossen dit probleem op door zowel gebruik te maken van een systeem van pNipam colloïden in water waarbij de brekingsindex van de deeltjes gelijk is aan het oplosmiddel, als van recente confocale technieken. Omdat de grootte van de pNipam deeltjes afhangt van de temperatuur, en daarmee dus ook de volume fractie van de dispersie, kunnen grote kristal-vloeistof grensvlakken verkregen worden door gebruik te maken van een temperatuurgradiënt. We gebruiken confocale microscopie om het heterogene nucleatieproces, het zich voortbewegende grensvlak en het stationaire grensvlak direct te volgen op de schaal van een enkel deeltje. Voor het zich voortbewegende grensvlak hebben wij de groeisnelheid van het kristal en de

diffusiecoëfficiënt van de vloeistofdeeltjes gemeten en gebruikt om het verschil in chemische potentiaal tussen kristal en vloeistof fase te bepalen. We hebben ook het effect van onzuiverheden op het voortbewegende grensvlak onderzocht en de kracht die nodig is om langs deze onzuiverheden te komen bepaald vanuit de locale kromming van het grensvlak.

Voor het stationaire grensvlak hebben we de verandering van de orde over korte afstand van de vloeistof naar de orde over langere afstanden van het kristal gevolgd. Het resultaat is goed in overeenstemming met wat gevonden word voor simpele atomaire systemen: om een maximale dichtheid over een korte afstand te krijgen nemen de deeltjes in de vloeistof een icosahedrische configuratie aan. Deze icosahedrische eenheden vertonen een vijfvoudige rotatiesymmetrie die een periodieke vulling van de ruimte onmogelijk maken. Dit leidt tot een eerste orde faseovergang die de kristal en vloeistof fases van elkaar scheidt. Aan het grensvlak worden de mogelijke manieren om te ordenen van de vloeistof beperkt in verhouding tot de bulk vloeistof. Dit resulteert in een verlaging van de configuratie entropie die daadoor het meest bijdraagt aan de grensvlak energie.

Verder vormen we een directe link tussen de structuur van de vloeistof en kristal fase van de colloïden en de vrije energie van het grensvlak. Dit doen we door de verandering in vrije energie over het grensvlak te meten vanuit de driedimensionale configuratie van de deeltjes. Het in drie dimensies vastleggen van de posities van de deeltjes zorgt er voor dat we direct het vrije volume en het vrije oppervlakte kunnen meten dat beschikbaar is om extra deeltjes toe te voegen. Op deze manier wordt de energie en de spanning van het grensvlak tussen het kristal en de vloeistof bepaald. Door zijn structuur hangt de grensvlakspanning af van zijn richting ten opzichte van de vlakken van het kristal en is daardoor anisotroop. Deze anisotropie speelt een grote rol in de vorming en stabiliteit van de groei van kristallen. Het direct meten van deze anisotropie is echter zeer moeilijk. In veel gevallen wordt deze afgeleid van metingen gedaan voor het gehele macroscopische systeem. Wij maken gebruik van thermische fluctuaties aan het grensvlak om de grensvlakspanning en de anisotropie daarin te meten. De gemeten gemiddelde grensvlakspanningen, verkregen door beide methoden, komen goed overeen met waarden verkregen uit simulaties van harde bollen en ietwat zachte bollen. De gemeten anisotropie daarin daarentegen, is veel groter dan wat in de simulaties werd gevonden.

In het tweede deel van dit proefschrift laten we zien dat we een actieve controle hebben over het organiseren van colloïden in zowel evenwichtsstructuren als in structuren die ver van het evenwicht gevormd worden. Dit doen we door gebruik te maken van attractieve kritische Casimir krachten. Deze krachten ontstaan door fluctuaties in de concentratie van een binair mengsel van oplosmiddelen. De sterkte en de afstand waarover deze krachten werken, hangt af van de correlatie lengte van het mengsel en wordt daardoor bepaald door temperatuur. Door de temperatuur zeer langzaam te veranderen en daarmee uitermate nauwkeurig de interacties tussen de deeltjes te beheersen, kunnen we de deeltjes colloïdale versies van moleculaire vloeistoffen of vaste fasen laten vormen. De paar-interacties tussen de deeltjes en de paar-distributie kunnen direct gemeten worden door de dichtheidsfluctuaties van de deeltjes in de gasfase te volgen. Hierdoor kunnen we onderzoeken of de huidige continuüm modellen wel van toepassing zijn op het colloïdale organisatie proces. We passen het model voor het condenseren van gassen van Van der Waals toe om aan te tonen dat deze theorie het condenseren van een colloïdaal gas precies beschrijft, zelf op de schaal van maar een paar deeltjes.

De inzichten verkregen uit de experimenten kunnen direct gebruikt worden in simulaties om het volledige fasegedrag van colloïden met attractieve kritische Casimir krachten te kunnen onderzoeken. De experimenteel bepaalde paar-potentialen tussen de deeltjes werden daarom gebruikt in Monte Carlo simulaties om het volledige fasegedrag van colloïden in binaire mengsels te onderzoeken. Deze combinatie stelde ons voor het eerst instaat om evenwichten tussen fasen te simuleren ontstaan door het kritische Casimir effect. In de simulaties vonden we een colloïdaal gas, vloeistof en een vaste stof als functie van de temperatuur en de volume fractie van de deeltjes. Het gevonden complete fase diagram komt goed overeen met wat er in experimenten gevonden is. Het heeft de karakteristieke vorm van diagrammen voor moleculaire potentialen, zoals bijvoorbeeld Lennard-Jones, maar voor maar een zeer klein temperatuur bereik. Dit komt door de sterkte temperatuursafhankelijkheid van de kritische Casimir interacties.

De homogene nucleatie van een vloeistof vanuit zijn damp is van fundamentele interesse in het begrijpen van de formatie van fasen in eerste orde fase overgangen. Ondanks zijn belangrijke betekenis, is het direct observeren van de nucleatie van de vloeistoffase op moleculaire schaal zeer moeilijk. Wij laten zien dat door de toepassing van het kritische Casimir effect op colloïdale schaal een direct beeld gekregen kan worden van de vloeistof

nucleatie, zelfs op de schaal van een enkel deeltje. Dit stelt ons in staat om de effecten van thermische fluctuaties van de deeltjes aan het oppervlak te zien op de fluctuaties in de grote van de nucleus. We passen een nieuwe manier toe waarin we de vrije energie van de vloeistof clusters, de oppervlaktespanning en het chemische potentiaal verschil tussen het gas en de vloeistof direct bepalen vanuit de gemeten grootteverdeling van de clusters. Ook bepalen we de oppervlaktespanning direct vanuit het paar-potentiaal van de deeltjes en de structuur van de vloeistof clusters bij verschillende mate van oververzadiging. Deze resultaten geven een unieke kans om de toepasbaarheid van nucleatietheorieën te testen.

Als laatste bestuderen we in detail de verandering van de structuur van fractale aggregaten door experimentele controle over de interacties te complementeren met Monte Carlo simulaties voor diffusie gelimiteerde aggregatie. Aan de ene kant springen we experimenteel in een temperatuur gebied waarin de deeltjes een zeer hoge attractieve kracht ondervinden waardoor ze direct aggregaten vormen met een goedgedefinieerde structuur. We leggen de relatie vast tussen de fractale dimensie van deze aggregaten en de diepte van de interactie potentiaal door beelden te nemen van de ontstane aggregaten. Aan de andere kant, gebruiken we Monte Carlo simulaties van diffusie gelimiteerde aggregatie met een eindige kans op dissociatie om het aggregatie proces te modeleren en de ontstane structuren te koppelen aan een kans op dissociatie van een deeltje en dus aan de aantrekkingskracht tussen de deeltjes. Uit de goede overeenstemming tussen experimenten en simulatie concluderen we dat voor een diffusie gelimiteerd aggregatie proces het gedrag universeel is: dezelfde aantrekkingskracht leidt tot dezelfde structuur, ongeacht het type deeltje en de dimensie van het systeem.

Onze resultaten bevestigen dat het temperatuurgevoelige colloïdale systeem aan de ene kant een sterk model systeem is om moleculair fasegedrag de bestuderen. Aan de andere kant bied het nieuwe mogelijkheden voor het actief en gecontroleerd samenstellen van micro- en nanostructuren.

Publications

1. **V.D. Nguyen**, M.T. Dang, B. Weber, Z. Hu and P. Schall, *Visualizing the structural solid-liquid transition at colloidal crystal/fluid interfaces*. Adv. Mater. 23, 2716-2720 (2011). (**Cover page**).
2. **V.D. Nguyen**, Z. Hu and P. Schall, *Single crystal growth and anisotropic crystal-fluid interfacial free energy in soft colloidal systems.* Phys. Rev. E. 84, 011607 (2011).
3. M.T. Dang, **V.D. Nguyen**, A.V. Verde, P. Bolhuis, P. Schall, *Monte Carlo simulations of a temperature sensitive colloidal phase behavior induced by critical Casimir forces*. Under review of Soft Matter.
4. **V.D. Nguyen**, S. Faber, Z. Hu, G. H. wegdam, P. Shcall, *Controlling colloidal phase transitions with critical Casimir forces*, Under review of Nature communications.
5. P. Schelke, **V.D. Nguyen**, *Universality of morphology changes in colloidal aggregation*, in manuscript.
6. **V.D. Nguyen**, Z. Hu, P. Schall, *Visualization of colloidal liquid nucleation induced by critical Casimir forces*, in manuscript.

Oral presentations

1. '*Colloidal crystal-fluid interface: Anisotropy and free energy*', American Physical Society (APS) conference 2010
2. '*Critical Casimir effect provides direct control of colloidal interactions*', APS 2010
3. '*Colloidal Gas-liquid condensation induced by the critical Casimir effect*', APS 2011
4. '*Critical Casimir force: novel control of colloidal assembly*', Netherland Organization for Scientific Research conference 2011
5. '*Colloidal Gas-liquid transition: Tuning nucleation and growth by critical Casimir effect*', APS 2012
6. '*Visualization of colloidal liquid nucleation induced by critical Casimir forces*', Dutch soft matter conference 2012 (**invited**)

Acknowledgments

I would like to take this opportunity to thank all of the people who have supported me in finishing this thesis and the people who have made positive changes in my life.

First of all, it is with immense gratitude that I acknowledge the support and help of my supervisor Dr. Peter Schall who has given me a great opportunity to work in a pleasant research environment, with such interesting subjects. Dear Peter, thank you very much for introducing me into the fascinating world of soft condensed matter physics and many thanks for your elegantly clear guidance.

I am grateful to my promoter Prof. Dr. Daniel Bonn for many valuable suggestions. Dear Daniel, discussions with you always saved me a lot of time on searching and reading the extensive subject literature.

I would like to express my special thanks to Prof. Gerard H. Wegdam, Dr. Rudolf Sprik, Prof. Dr. Peter Bolhuis and Prof. Dr. Marjolein Dijkstra for fruitful discussions on light scattering, the critical Casimir effect and free energy measurement.

I would like to thank all of the committee members for their positive and much appreciated comments enabling me to improve my thesis.

Many thanks are given to Triet, Bart, Pradip and Suzanne for their collaborations. Triet, thank you very much for helping me with Matlab codes to determine the free energy based on the free volume and free surface area. My experimental results of the colloidal phase behavior induced by the critical Casimir effect have been confirmed by your simulations. Bart, thank you very much for your help in determining particle configurations produced

during your bachelor project. Pradip, I am very happy that your simulation results of the fractal dimensions are in good agreement with my experiments. Suzanne, I enjoyed not only the time supervising you but also our little chat during relax time.

Many thanks to Prof. Zhibing Hu, at the University of North Taxes, for your collaboration, providing me pNiPam particles and helpful comments regarding the manuscripts of our article published on Advanced Materials.

Sandra, I thank you very much for the Dutch translation of the Summary.

Kiên, I thank you very much for the designing of the cover. My dear friend, I wish you all the best.

I would like to thank all of the people from the Glass, Mechanical and Electronic Workshops who helped me to design the many setups and the sample cells for my experiments.

I am grateful to Arend van Leeuwen, Peter de Goeje, Niels Molenaar who were always available as needed. Arend, Peter and Niels I really appreciate your kindness. You helped us to solve a lot of problems with our Visa, housing, and Dutch language letters, etc. It would take pages to list all your help.

I would like to thank Luuk Lusink, Rita Vinig, Ineke Baas, Truc Ngo, Erith Boniel, Elvire Smeets and Thès Smeets for their kind help in administrative matters.

Ton Gortenmulder and Henny Gortenmulder, Ton Riemersma and Lia Riemersma, thanks a lot for donating the very useful things for our babies when they were born. Ton and Henny, I remember that you were the first people who came to welcome our daughter Cam Ha to her life.

I would like to thank Ekkes Brück and the people in his group for allowing me to use their computers and offices before I had my own working place in the Soft Matter group. Dear Ekkes, I know that you did your best to help my wife not only in her research but also in her personal life.

I have greatly appreciated the Soft Matter group members for so many active discussions during our group meetings, in the office, during the coffee break and lunch times. I wish all of you the best of luck in the future.

It was my pleasure to work in the WZI of the University of Amsterdam. I would like to thank all my colleagues for making such a friendly working environment. I really enjoyed sharing the time with you during the international cooking party, the lab outings, the table

tennis and the football tournaments and so many other funny little chats during our leisure time.

Anh Lộc, thank you very much for the nice time at Eliss. It did not feel like you were my boss, rather it felt that you were a big brother who was providing me a lot of advices in my life. Eliss members, I will always miss you. I enjoyed every moment that we were together, especially during the funny dance tournament, volleyball, table tennis, football, Tá Lả, Bánh Chưng, etc.

I thank all of my Vietnamese friends in the Netherlands for the many pleasant times at parties, playing football, tennis, table tennis and poker.

I would like to take this chance to thank my teachers and my dear friends at the University of Science (Hanoi, Vietnam) and at the schools in Dong Trieu.

I would like to express my gratefulness to my parents, my brothers and my parents-in-law for their constant support and enduring love. Mom and Dad, you always manage to inspire me to study.

Words are never enough to express my deep gratitude and my love to my wife, Cẩm Thanh, my daughter Cẩm Hà and my tiny son "Tortoise" Đức Việt.

I would like to close this thesis with my heartfelt gratitude to my mother. Mom, you are always in my heart. I love you.